Design of nanostructures and hybrids of transition metal derivatives for energy storage applications

Guanjie He

A thesis presented for the degree of

Doctor of Philosophy

Supervised by

Professor Ivan P. Parkin

Professor Jawwad A. Darr

Department of Chemistry

Mathematical and Physical Sciences Faculty

University College London

May, 2018

I, Guanjie He, confirm the work presented in this thesis as my own. Where information has been derived from other sources, I confirm that this has been indicated in this thesis.

Abstract

The research for high-performance energy storage devices, such as supercapacitors, Li-ion batteries, is continuing apace. These devices can store energy *via* electrochemical processes. However, further increases of capacity and stability of these devices to meet practical requirements remain a challenge. By using nanostructured electrode materials, several strategies were proposed in this thesis based on transition metals and their derivatives.

The binder-free strategy was used across the entire project, which could increase the utilization and avoid “dead volume” of active materials. To improve the commonly reported electrochemical performance in aqueous of transition metal hybrids, such as nickel, cobalt or tungsten materials, bimetal nanostructured electrodes were proposed. Ni foam supported $NiWO_4$ and $CoWO_4$ electrodes were synthesized and increased the capacity and rate performance because of an increased electrical conductivity. Other methods for enhancing energy storage performance by means of increased electrical conductivities were found to be the sulfide or nitride counterparts of the corresponding oxide.

To further improve the specific capacity and clarify the blurred energy storage mechanism of nickel or cobalt-based electrode materials, nickel cobalt sulfide nanostructures within sulfur and nitrogen-doped graphene frameworks were produced. Importantly, the redox reactions between materials and OH^- groups were demonstrated as diffusion-controlled processes. In addition, the solid-state devices and properties of oxygen reduction were explored.

Pseudocapacitor electrodes are attractive by bridging the power density and energy density between the electro-double layer capacitor and batteries. W_2N@C

core-shell structures on carbon cloth was synthesized by chemical vapour deposition *via* an ammoniation process and evaluated for supercapacitor performance. Combining with electrochemical analysis, *in-situ* electrical measurements and simulation, the merits of W_2N materials were determined.

The interesting nanostructured electrodes could be utilized in Li-ion batteries. Illuminated by above stratigies and considering the stable structures, capacity contribution and Li intercalation, a highly stable V_2O_5-based cathodes were developed.

Impact statement

With the coming of the mobile internet era, portable devices, electrical vehicles and large-scale energy storage stations are ubiquitous. These applications demand better performance from energy storage devices.

Supercapacitors, hybrid devices and Li-ion batteries occupy a large area in the Ragone plot. The PhD project was to solve the problems and boost the performances associated with commonly used electrodes in supercapacitors and batteries *via* chemical synthesis of different nanostructures as novel electrodes.

Highlights:

(1) The utilization of flexible electrodes configuration provides the foundation for next-generation of bendable devices.

(2) The definition of rechargeable alkaline battery electrodes from a kinetic view was presented. The misleading concepts provided on Ni and Co based nanomaterials as supercapacitor electrodes because of the surface-controlled energy storage behaviour and the obscure explanations of these materials for use as battery-type supercapacitor or hybrid supercapacitor electrodes was resolved. In addition, the formulas to evaluate these hybrid battery devices (formerly called asymmetric supercapacitor devices) from most of previous work were not unified and accurate, for instance, the energy density and power density calculations. In this thesis, the detailed calculation formulas to illustrate the actual performances of the devices were proposed to enable standardization for performance comparisons for future work in this area.

(3) Tungsten nitrides were compared to oxides and shown that they boost potential of nitrides in energy storage and conversion applications.

(4) The unique core-shell structure considering stable structure, diffusivity of metal-ions and separate function design provides design concepts for future metal-ion batteries.

(5) All the designed and synthesized transition metal materials of different dimensions are promising for other applications, which require exposed active sites, high surface area, robust structures or fast electron pathways.

Beyond the academic research, parts of the PhD project have also attracted great interest during public events and lectures, especially the fabricated cells and bendable devices that powered LED light demonstrations.

Acknowledgements

First and foremost, I would like to express the deep appreciation for my supervisor, Prof. Ivan P. Parkin. I could not achieve any progress in the research without his wise guidance and massive support. Prof. Parkin's attitudes towards science, engineering, management and life inspired me a lot, especially for building up my academic career.

I would like to thank all the collaborative supervisors. Prof. Zheng Xiao Guo, Prof. Jawwad A. Darr, Dr. Katherine B. Holt, Prof. Claire J. Carmalt, Prof. Gopinathan Sankar in UCL Chemistry Department; Prof. Dan J.L. Brett and Dr. Ryan Wang in UCL Chemical Engineering; Prof. Hailiang Wang in Yale Univeristy; Prof. Magdalena Titirici in Queen Mary University of London, Prof. Qiang Zhang in Tsinghua University and Prof. Xia Zhang in Henan University. Special thank to Prof. Rujia Zou in Donghua University, Prof. Wenyao Li in Shanghai University of Engineering Science and Prof. Bo Li in Chinese Academy of Sciences for their long-term collaboration and supports for my research.

I am deeply grateful to all my collaborators. Dr. Xiaoyu Han for simulation, Dr. Yao Lu and Prof. Xia Zhang for self-cleaning surfaces, Dr. Min Ling and Mr. Yaomin Li for CVD synthesis, Miss Tingting Zhao, Dr. Srinivas Gadipelli, Mr. Runjia Lin and Mr. Zhuangnan Li for electrochemistry in UCL Chemistry Department. Thanks to Miss Dina Ibrahim Abouelamaiem, Dr. Shan Ji, Dr. Noramalina Mansor, Mr. Ruoyu Xu in UCL Chemical Engineering, Miss Mo Qiao in Queen Mary University of London, Dr. Zhe Weng in Yale University, Dr. Andreas Kafizas in Imperial College London, Dr. Yuanlong Shao in University of Cambridge, Mr. Jianmin Li in Drexel university and Mr. Feili Lai in Fudan University for their support in characterization and discussion. Thanks to all the group members in Prof. Parkin's group, especially Dr. SocMan Ho-Kimura, Dr. Nuruzzaman Noor,

Dr. Sanjay Sathasivam, Dr. Kristopher Page, Dr. Raul Quesada Cabrera, Dr. Tom Macdonald, Dr. William Peveler, Dr. Caroline E. Knapp and Dr. Michael Powell. I had a wonderful and meaningful time here.

In addition, I would like to thank technicians and management teams Department, Dr. Zhimei Du, Mrs. Ninik Smith, Mrs. Judith James, Mr. Tony Field, Dr. Steve Firth, Mr. Martin Vickers, Mr. Joe Nolan and Mr. Kavanagh Brian in Chemistry and Dr. Toby Neville and Dr. Jason Millichamp for the help with management and equipment training.

Finally, I would like to thank my parents and all relatives for their infinite love and all my friends in London. Thanks for UCL-CSC scholarship, STFC early career award and UCL-Yale exchange program for financial support.

Contents

List of Figures

Chapter 1 Background and Introduction

Chapter 2 Ni foam supported $NiWO_4$ and $CoWO_4$ nanostructures for supercapacitor electrodes

Chapter 3 Boosting Energy Storage and Coversion Performance by S, N-co-doped Graphene-Nickel Cobalt Sulfide Aerogels

Chapter 4 Tungsten Nitrides Used as Self-standing Electrodes for High-performance Supercapacitors

Chapter 5 Structural Design for Realizing Highly Effective and Stable Cathodes in Rechargeable Li-Ion Batteries

List of Tables

Abbreviation

1D	One-dimensional
2D	Two-dimensional
3D	Three-dimensional
AACVD	Aerosol-assisted chemical vapour deposition
ADs	Asymmetric devices
AFM	Atomic force microscopy
CA	Chronoamperometric
CBM	Conduction band minimum
CD	Charge-discharge curves
C_{device}	Capacity of the device
Ci-NEB	Climbing Image Nudged Elastic Band
CSA(s)	Core-shell array(s)
CV	Cyclic voltammetry
CVD	Chemical vapour deposition
DFT	Density Functional Theory
DOS	Density of states
E_{area}	Areal energy density
EDLC(s)	Electrical double layer capacitor(s)
EDS	Energy dispersive X-ray spectrometer
EIS	Electrochemical impedance spectroscopy
E_{mass}	Gravimetric energy density
EMI, BF4	Ethyl-methyl-immidazolium tetra-fluoro-borate
E_{volume}	Volumetric energy density
F_a	Adhesive force
FASD	Flexible asymmetric supercapacitor device
F_c	Contracted force
FFT	Fast fourier transformation
GAs	Graphene aerogel(s)
GCD	Galvanostatic charge-discharge
GO	Graphene oxide
HRTEM	High-resolution transmission electron microscopy
i_{disk}	Current densities on the disk
i_{ring}	Current densities on the ring
LDH	Double layer hydroxides
LIBs	Lithium-ion batteries
MFC	Mass flow controller
NC	Nitrogen-doped carbon
Ni-Co-S/SNGA	S, N doped graphene-based nickel cobalt sulfide aerogel
OER	Oxygen evolution reaction
ORR	Oxygen reduction reaction

PAW	Projector-augment wave
PCs	Pseudocapacitors
P_{mass}	Gravimetric power density
Pt	Platinum electrode
PVA	Polyvinyl alcohol
P_{volume}	Volumetric power density
R_{ct}	Charge transfer resistance
RDE	Rotating disk electrode
RRDE	Rotating ring-disk electrode
R_s	Equivalent series resistance
SDs	Symmetric device(s)
ASDs	Asymmetric device(s)
SEM	Scanning electron microscope
SNGA	S, N co-doped graphene aerogel
TEM	Transmission electron microscopy
TEM-STM	Transmission electron microscope-scanning tunneling microscope
TMO(s)	Transition metal oxide(s)
VASP	Vienna Ab *initio* Simulation Package
VBM	Valence band maximum
XAS	X-ray absorption spectroscopy
XPS	X-ray photoelectron spectroscopy
XRD	X-ray diffractometer
Z_w	Warburg resistance

Chapter 1

Background and Introduction

1.1 Energy Storage Devices

With increasing demands for clean energy technologies to eliminate environmental pollution, new types of energy production, such as wind, solar and tidal, are being intensively investigated.[1] These energy resources are sustainable and environmentally friendly, but they are intermittent and dependent on geographic conditions.[2] Under this situation, the evolution of the next generation of energy storage and conversion devices are necessities for widening utilization.[3, 4] Energy storage and conversion apparatus, for instance supercapacitors,[5-7] rechargeable metal-ion batteries,[8, 9] solar cells[10] and fuel cells[11] play considerable roles for portable electronics and electric vehicles. In this chapter, commonly used energy storage devices will be introduced.[12] The electrode materials for two promising devices, *i.e.* supercapacitor and Li-ion batteries (LIBs), mainly based around transition metal materials and their derivatives will be discussed. Furthermore, the synthesis and design strategies of representative transition metal nanostructures are presented. The purpose of the PhD project is the chemical synthesis of electrode materials based on nanostructured design for energy storage devices with high performance, such as superb specific capacity, rate capability and long-term cycling stability.

Ragone plots are commonly used for comparison the performance of different kinds of energy storage devices. [13] In this chart, the values of the specific power density (volumetric or gravimetric density) are plotted versus corresponding energy density, to compare the values of the energy stored in the devices and the speed of that energy's release. Figure 1.1 presents the Ragone plot of commonly used energy storage devices, *i.e.* capacitors, supercapacitors, batteries and fuel cells. These four energy storage devices are introduced below.

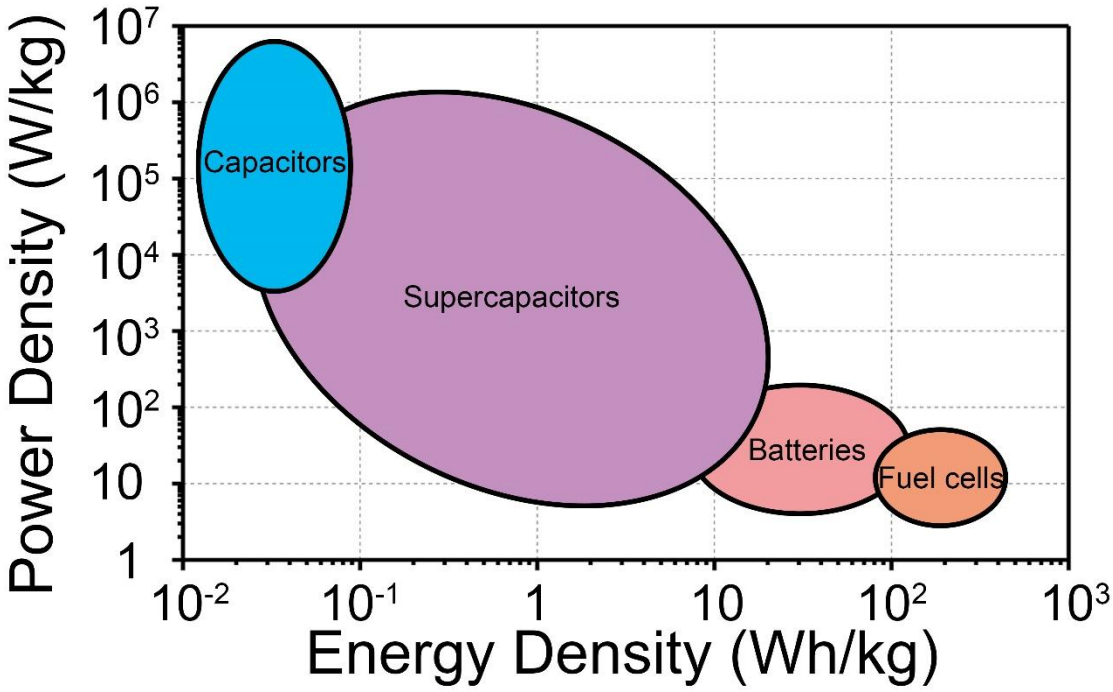

Figure 1. 1 Ragone plot of typical energy storage devices.

1.1.1 Capacitors

Capacitors store charge by physical charge separation between two electrodes. [5] They store energy on the surfaces of electrodes (metal, metallized plastic film or a layer of oxide materials covered metal), which is more likely due to a physical process. The capacitance could be calculated by the following equation:

$$C = \frac{\varepsilon S}{4\pi k d} \qquad (1.1)$$

Where C is capacitance, ε is the dielectric constant, S is the overlapping surface area of electrodes, d is the distance between two electrodes and k is the electrostatic constant.

A capacitor normally exhibits much lower specific energy density compared to supercapacitors and batteries but shows ultrahigh power density. This suggests that capacitors can deliver high current density within an extremely short period as the specific capacitance (energy density) is quite low.

1.1.2 Fuel cells

Fuel cells provide energy through converting chemical energy from an electrochemical reaction between hydrogen and oxygen or other oxidants. [3] Like other electrochemical cells, fuel cells are composed of anodes, cathodes and electrolytes. Anodes are where the oxidation reactions occur, as opposite to the cathodes for reduction reactions. In most fuel cells, hydrogen enters through field flow plates to the anode part, where catalysts help them to go through the oxidation reactions, forming protons (H^+) and electrons. The electrolytes allow only the H^+ to travel through to the cathodes, however the electrons need to go along the external circuit to the cathodes. In the cathodes, the oxygen from air participate in reduction reactions and combine protons and electrons to form water. Compared to other energy storage systems, fuel cells exhibited much higher energy density but relatively poor power densities. The generation and storage of hydrogen and its related safety issues limit the application of fuel cells in portable devices.

1.1.3 Supercapacitors

The Ragone plot in Figure 1.1 shows that supercapacitors bridge the large gap between capacitors and batteries. [14, 15] They could store more than two orders of magnitudes of energy per unit mass or volume compared to normal capacitors and deliver much faster charging than that of batteries. Supercapacitors can be classified into two types according to the different charge storage mechanisms in Figure 1.2.[5]

(1) Electric double layer capacitors (EDLCs)

EDLCs store charges *via* reversible electrochemical double layer formation, these are fast non-Faradaic reactions at the electrode/electrolyte interfaces. [16] During charge/discharge processes, electric charges store on the surface of two

electrodes, meanwhile ions with opposite charges are arranged in the electrolyte. Commercial EDLCs electrodes are highly porous carbon, for example active carbon, graphene and carbon nanotubes. [5]

Helmholtz firstly described the mechanism of EDLCs in 1853. This was further improved by Gouy and Chapman, as well as Stern and Geary. [17] A diffuse layer in the electrolyte was introduced because of the accumulation of electrolyte ions around the surfaces of electrodes. [18] Their conclusions are as follows: there are two interactions between electrode/electrolyte interfaces. One is the electrostatic interaction of the ions from the electrolyte; the other is the short-range interaction between the electrodes and different kinds of ions, such as the forces from Van der Waals and electrovalent bond. These interactions provide the trend for ions with opposite charges attaching on the surface of the electrodes, forming dense layers. Due to thermal motion, the ions in the electrolyte could not uniformly cover the whole surface of the electrodes, thus forming a diffuse layer. Under this situation, the conflicting interactions between electron static force and the thermal dynamics result in both dense and diffuse layers contributing to electrochemical double layers. If we suppose the dielectric constant is invariable in a dense layer, the potential within this layer is a linear function with distance, however the potential in the diffuse layer is changed nonlinearly. If the potential of solution far from the electrode is regarded as zero, the equation for calculation of EDLCs capacitance can be expressed as follows: [18]

$$\frac{1}{C} = \frac{d\varphi_a}{dq} = \frac{d(\varphi_a - \psi_1)}{dq} + \frac{d\psi_1}{dq} = \frac{1}{C_{dense}} + \frac{1}{C_{diffuse}} \qquad (1.2)$$

Where C is the total capacitance, φ_a is the total potential difference for the whole electric double layers, ψ_1 is the average potential difference for the distance which is d away from the electrodes. In this case, the potential difference for diffuse layer is ψ_1, and the potential difference for dense layer is $\varphi_a - \psi_1$.

Usually, the double-layer capacitance can realize 5 ~ 20 μF cm^{-2} in different electrolytes.[19] The specific capacitance of EDLCs is generally higher in aqueous alkaline or base electrolyte (most commonly used 1 M H_2SO_4 or 2 M KOH) than that of the ionic liquid in organic electrolyte, such as 1 M 1-ethyl-3-methylimidazolium tetrafluoroborate (EMI BF_4) in acetonitrile (AN).[5, 19] But the specific energy density is higher in an organic electrolyte than in an aqueous electrolyte according to the equation:

$$E = \frac{1}{2}CV^2 \qquad (1.3)$$

Where E is the specific energy density, C is the specific capacitance and V is the voltage range of the supercapacitors. In an organic electrolyte system, the symmetric EDLCs (same materials and loading for both electrodes) can sustain a wider operation voltage window (~ 3 V) compared to aqueous electrolyte. The three time increase in voltage range leads to approximately an order of magnitude enlarged energy density stored under the same capacitance.

Compared to pseudocapacitors, there is no redox reaction occurring at the surface of the EDLC electrodes, which provides a major contribution to the long-term stability. For carbon materials, there is no obvious decay of performance even after tens of thousands of cycles. The surface charge storage favours super-fast energy input and output, inducing higher power performance. The non-Faradic process limits high specific capacitance and energy density of the electrodes.

(2) Pseudocapacitors

Different from EDLCs, pseudocapacitors utilize both fast and reversible redox reactions and adsorption of electrolyte ions at the surface or near-surface of the electrode materials. A series of transition metal-based materials, such as WO_3, [20,21] MnO_x [22] and RuO_2, [23] possessing various valence states are favorable for

surface multi-electron redox reactions. In addition, several electronically conducting polymers, such as polypyrrole [24] and polyaniline, [25] have been intensively studied. Those electrodes outperform carbon materials for their specific capacitance. By utilizing different working potential electrode materials, asymmetrical supercapacitors could be fabricated, thus wider potential windows and higher energy/power density can be realized. However, because of the redox reactions happening on the surface, pseudocapacitors suffer from poorer stability compared to EDLCs.

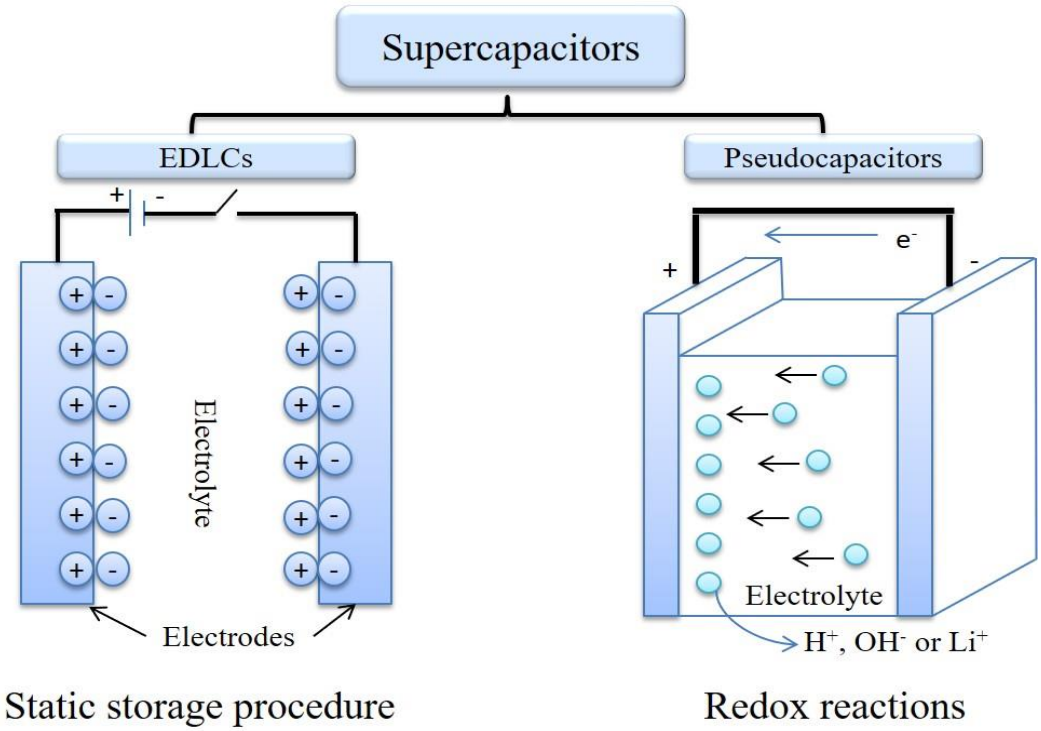

Figure 1. 2 Two categories of supercapacitors according to different charge storage mechanisms.

1.1.4 LIBs

The major difference between batteries and supercapacitors is from the electrochemical kinetic view point. The charge storage mechanism of batteries is a diffusion-controlled process; however, supercapacitors are surface-dominated.

[14] Among diverse secondary metal-ion batteries, LIBs have distinct merits, such as high energy density, relatively low self-discharge and remarkable long-term stability. [3, 8, 26] As similar to common electrochemical cells, LIBs consist of two electrodes, electrolyte and separator to avoid short circuits in Figure 1.3. The LIBs were first commercialized by Sony in 1991. Commercial LIBs often use lithium cobalt oxide ($LiCoO_2$) as the positive electrode and graphite (C) as the negative one. The organic electrolyte containing Li salts provide the wide working potential window for LIBs. The reversible redox reaction in this kind of commercial LIBs is $\mathrm{LiCoO_2} + C_6 \leftrightarrow \mathrm{Li_{1-x}CoO_2} + \mathrm{Li_xC_6}\ (0 < \mathrm{x} \leq 1)$. During the charge process, the Li ions are transferred to C, forming $Li_{1-x}CoO_2$ and Li_xC_6. The current goes from the anodes to the cathodes during the charge process, whereas during discharge, the reverse reaction occurs, and current goes in the opposite direction.

However, the reaction mechanism of the electrodes during lithiation and de-lithiation process are different and can be divided into three kinds. [26]

(1) Intercalation-deintercalation mechanism. Graphite materials and some transition metal oxide materials with layered structures or three-dimensional network structure that can intercalate Li into the lattice without destroying the crystal structures. Layered V_2O_5 materials are good examples and can be expressed by the chemical equation:

$$V_2O_5 + x\ Li^+ + x\ e^- \leftrightarrow Li_xV_2O_5\ \ (0 \leq x \leq 3) \quad (1.4)$$

Additionally, these electrode materials should contain the ability for forming lower valence states ions (usually of the transition metals) to stand the intercalation of the Li ions together with the electrons.

(2) Alloying/de-alloying mechanism. Some metals or elements can form alloys with Li metal, thus forming intermetallic compounds. Those compounds exhibit different physical properties and lattice parameters to the initial Li and

metals or alloys. Metals like Zn, Bi or Sn and elements such as Sb and Si are commonly used electrode materials. Take Si as an example:

$$Si + 4.4\,Li^+ + x\,e^- \leftrightarrow Li_{4.4}Si \qquad (1.5)$$

During lithiation process, Si electrodes exhibited large volume change of more than 300 times. [27-29] This may cause problems, such as safety issues for causing short circuits, and thereby reducing performance by loosening the electrical contact between active materials and current collectors.

(3) Redox reaction mechanism. This reaction is also named as a conversion reaction with Li metals. Li_2O is normally regarded as the electrochemically inactive components and cannot be decomposed to Li and O_2. However, in the presence of some nanostructure transition metal-based materials, such as CoO or NiO, Li_2O can be decomposed. For example, the surface of mesoporous NiO causes a reversible reaction to occur at a suitable potential range:

$$NiO + 2Li^+ + 2e^- \leftrightarrow Ni + Li_2O \qquad (1.6)$$

Moreover, the redox reaction mechanism is in general a Li-storage phenomenon and can be applicable to binary, ternary and even complex oxides systems. Both theoretical design and chemical synthesis have been employed to prepare those materials by means of improving the electron conductivity, increasing the mobility of Li^+ and enhancing the structural stability to boost the electrochemical performance of the electrodes.

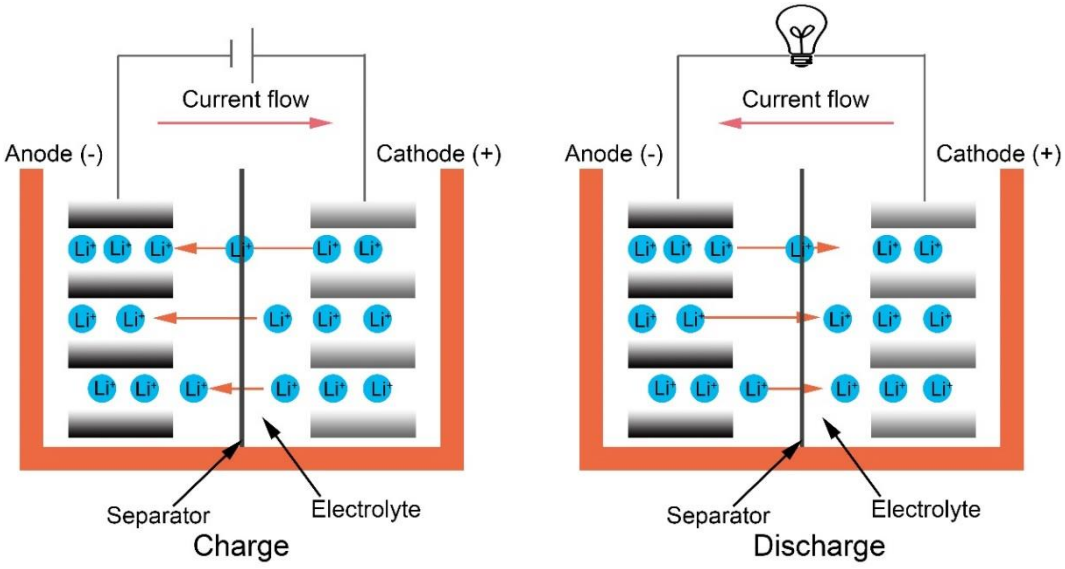

Figure 1. 3 Charge storage mechanism of LIBs.

A literature search of energy storage devices shows that transition metal-based materials play an important role as electrode especially for pseudocapacitors and LIBs. [30-39] By using different materials and structures, the energy of electrochemical storage properties can be optimized and realized by design. The following parts will focus on the introduction of the basic properties for transition metals materials and their synthesis. The rational design of the electrodes will also be discussed.

1.2 Transition metal materials

In general, transition metals, such as manganese or iron can typically form stable ions with incompletely filled d orbitals. These materials and their derivatives have a broad range of applications, such as energy storage and conversion, [38, 39] catalysts, [40] conductive metals, semiconductors [32] and bioimaging, [41, 42] *etc*. From the definition of the International Union of Pure and Applied Chemistry (IUPAC), “a transition metal is an element whose atom has a partially filled d sub-shell, or which can give rise to cations with an incomplete d sub-shell”. This classification draws up certain areas of the periodic table ranging from Group III

to X for transition metals, as shown in Figure 1.4. In detail, the pink area shows transition metals and the orange part of post transition metals.

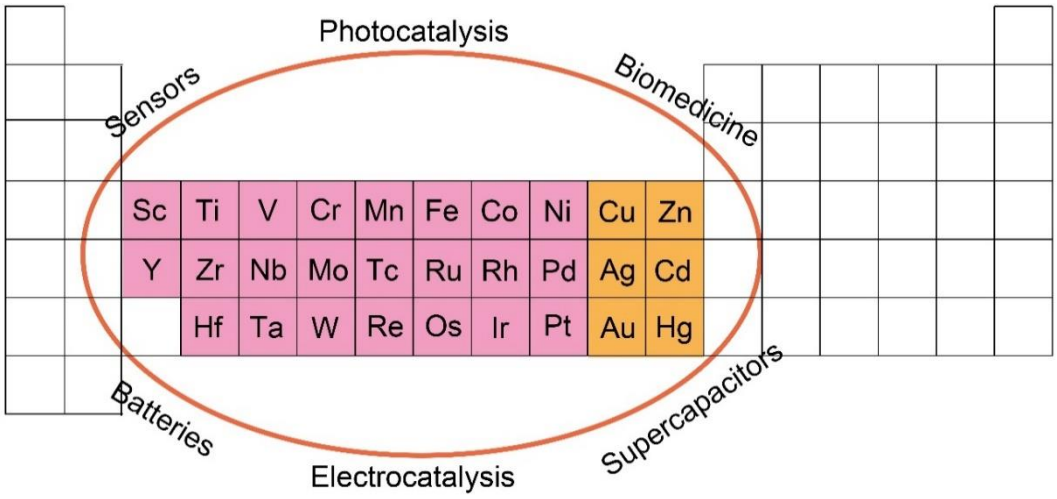

Figure 1. 4 Schematic illustration of application for transition metal materials.

1.2.1 Basic physical properties [43, 44]

As exemplified by the name, the common physical properties of almost all transition metals are that they possess excellent thermal and electron conductivity as well as high melting and boiling points. [43] For example, iron, a well-known heat and electron conductor, has a melting and boiling point of 1538 and 2862 °C, respectively. (Data from Wikipedia: Iron) These properties are the results of metallic bonding by delocalized d electrons, contributing to the enhanced cohesion in line with the increased number of shared electrons. The distribution of the d electrons also influences the magnetic properties of the transition metals. The unpaired d-electrons contributed to the paramagnetic properties of these materials. In some cases, such as low spin octahedral d^6 and square-planar d^8 complexes, those compounds demonstrate diamagnetic properties. Moreover, due to the absorption of light by d-d electronic transition, the presented colour of the transition metal ions is varied, such as the red of $Co(NO_3)_2 \cdot 6H_2O$ and blue of $CuSO_4 \cdot 5H_2O$.[44]

1.2.2 Typical Chemical properties

Another representative characteristic for transition metals is they often have multiple oxidation states. Table 1.1 lists the normal oxidation states for first row transition metals.

Table 1. 1 Representative properties for first-row transition metals

First Row Transition Metals	Ground state electronic configuration from M (0)	Oxidation States
Sc	[Ar] $3d^1 4s^2$	+3
Ti	[Ar] $3d^2 4s^2$	+2, +3, +4
V	[Ar] $3d^3 4s^2$	+2, +3, +4, +5
Cr	[Ar] $3d^5 4s^1$	+2, +3, +6
Mn	[Ar] $3d^5 4s^2$	+2, +3, +7
Fe	[Ar] $3d^6 4s^2$	+1, +2, +3
Co	[Ar] $3d^7 4s^2$	+1, +2, +3
Ni	[Ar] $3d^8 4s^2$	+1, +2, +3
Cu	[Ar] $3d^{10} 4s^1$	+1, +2
Zn	[Ar] $3d^{10} 4s^2$	+2

The feasibility of different oxidation states thus provides tunable chemical properties of the transition metals. [44] Take manganese as an example, the commonly noted oxidation states vary from +2 to +7. Manganese (+7) ions are strong oxidizers and can be used to oxidize and exfoliate carbon materials, *i.e.* Hummers' method. [45] Transition metals and their derivatives are intensively used in the catalytic area due to their various oxidation states thus forming complexes. Nickel oxyhydroxides are a kind of normally used materials in electrocatalytic oxygen evolution reactions (OER). [46, 47] The 3d/4s electrons were utilized for forming bonds between atoms of catalysts and reactant molecules (OH^- group).

Recent work reported adjusting the number of 3d electrons of nickel ions could optimize the catalytic performance of OER. [48] The following content will introduce some electrochemical properties of Ni or Co and W-based materials.

1.2.3 Ni or Co-based materials

Ni and Co are the constituent elements in Group VIII transition metals. These elements have different 3d electrons ($3d^8$, $3d^7$ for Ni^{2+} and Co^{2+}, respectively). They can form solid solution compounds easily and have similarities around their physical and chemical (electrochemical) properties. Both NiO and CoO are anode materials for LIBs. Ni or Co-based materials contain a series of metals, oxides, hydroxides, sulfides and different kinds of hybrid materials. The easy-preparation and scalable methods make them applicable for active/catalytic materials in the fields of energy storage and conversion. $LiCoO_2$ is a commercialized cathode material for LIBs; however, due to its high toxicity, other candidates are being synthesized for replacing $LiCoO_2$. [49] $LiNiO_2$ is an attractive replacement for $LiCoO_2$ but it also suffers from some disadvantages, such as poor stability and it is hard to achieve stoichiometry during preparation. [50] Recent research efforts have used $LiNi_xCo_{1-x}O_2$ as an alternative. These materials contain layered structures with an anion (almost) close-packed lattice. Dimesso *et al.* summarized the use of lithium transition metal phosphates for cathode materials in LIBs. [51] $LiCoPO_4$ and $LiNiPO_4$ exhibited olivine-type structures with relatively more open lattice structures. [52, 53]

1.2.4 W-based materials

The most commonly used tungsten-based materials in energy applications is its oxides. Stoichiometric WO_3 crystals are made up of WO_6 octahedra sharing corners and edges and possess different phases due to the different rotation direction. [54] These phases realize transformations during annealing process. The widely known electrochemical reactions between WO_3 and protons or metal

ions can be utilized for energy storage and electrochromism due to its colour change. [21] The chemical equation can be presented as：

$$WO_3 + xH^+(Li^+ \ or \ Na^+) + xe^- \leftrightarrow M_xWO_3 \quad (0 < x < 1) \quad (1.7)$$

Stoichiometric WO_3 crystals can easily lose oxygen atoms forming oxygen vacancy-rich WO_{3-x}. WO_{3-x} materials demonstrate a narrow bandgap and improved electron conductivity compared to stoichiometric WO_3, confirmed by observation of transition from insulator to metal properties for nonstoichiometric WO_{3-x} from Chakrapani's group.[55] By utilizing this property, Yu's group designed large-area co-assembled Ag and $W_{18}O_{49}$ nanowires for flexible smart window application.[56] Other modifications of WO_3 materials have been conducted, including WO_3 hydrates,[21] nitrides and carbides.[39, 57] These contents will be introduced in detail in the following chapters.

In traditional forms, *i.e.* bulk or aggregated materials, they could not provide benefits such as fast charge transfer for electrochemical performances. Recent progress around well-designed transition metal-based nanostructures *via* wet chemistry synthesis includes hollow structures, one-dimensional (1D) nanorods or nanowire and nanowires, [58] two-dimensional (2D) nanosheets [33, 59] and complex three-dimensional (3D) hierarchical build-up. [60-62] These high surface area architectures tend to have superior electrochemical performances.

1.3 Chemical synthesis

1.3.1 Hollow Structures

Hollow structures of transition metal materials have attracted great interest in electrochemical energy-related applications due to their high porosity, large surface-to-volume ratio and internal void space. [36, 63, 64] The high specific surface

area and open channels provide large ratios of active sites for redox reaction and charge storage. Additionally, thin shell layers expose large surface allowing fast diffusion and intercalation thus improving the kinetic process of the electrodes. Conventionally, building hollow structures relies on the hard or soft templates, such as silicate templates (porous silicate or silicate nanoballs with controlled size) or easily-synthesized metal oxides nanostructures. Then, the objective materials can form the shell on the template. Finally, the templates are selectively removed, leaving the shell materials to generate hollow structures.

For instance, Lou *et al.* recently synthesized uniform Fe_2O_3 nanocubes as the template, then coated with a layer of polydopamine (PDA). [65] As shown in Figure 1.5, the Fe_2O_3@PDA core-shell structures were annealed under N_2 atmosphere, transferring PDA to nitrogen-doped carbon (NC). Then, the oxide core is dissolved by acid etching, leaving the NC nanotube hollow boxes. Finally, flower-like nanosheets were synthesized directly on the NC hollow nanotube forming a uniform coating *via* hydrothermal process. The as-designed materials were used as photocatalysts for CO_2 reduction. The hollow structure enhanced the adsorption of CO_2 molecules, the carbon support facilitated separation and migration of charge carriers; and the enlarged specific surface area offered more active sites for photochemical reactions. The as-synthesized materials showed high stability and selectivity.

Another emerging method to produce hollow structures is the self-template process, the objective materials or their precursors can be used as the template directly, the following heat treatments or controlled etching processes result in the formation of hollow structures.

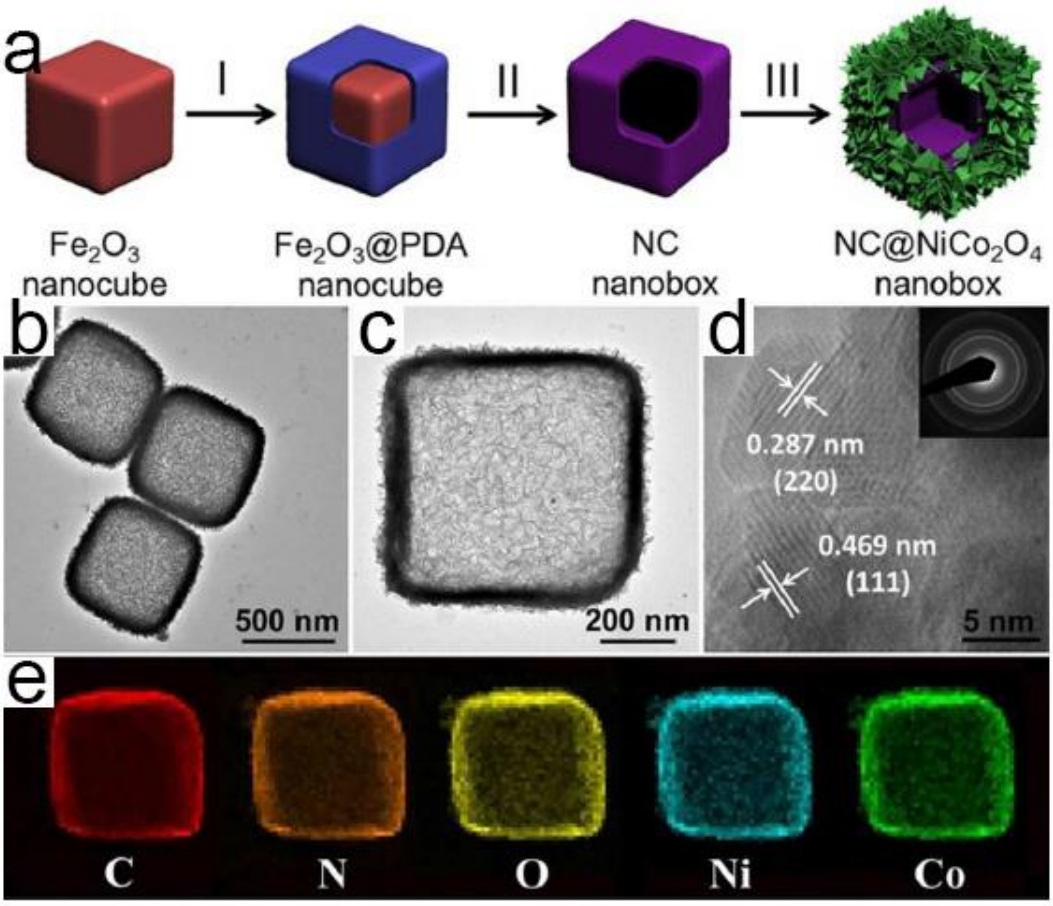

Figure 1. 5 (a) Synthetic procedure of nitrogen-doped carbon (NC)@$NiCo_2O_4$ nanoboxes. (I) Fe_2O_3 nanobox coated by polydopamine, (II) annealing and acid etching to form NC nanobox, (III) growth of $NiCo_2O_4$ nanosheets; (b-c) TEM images of NC@$NiCo_2O_4$ nanoboxes, (d) HRTEM image of the $NiCo_2O_4$ nanosheets and SAED pattern (inset) of selected area in NC@$NiCo_2O_4$ nanoboxes, and (e) EDS mappings of a representative NC@$NiCo_2O_4$ nanobox. (Copyright © 2018, Royal Society of Chemistry. Reproduced with permission)

For example, core-in-double shell $NiCo_2O_4$ hollow spheres were prepared *via* two facile steps in Figure 1.6. [66] At first, Ni-Co glycerate spheres were prepared by a solvothermal process. Then, the hollow structures were obtained from the nonequivalent thermal treatment. At the initial calcination stage, the large discrepancy of the temperature along radial lines directs the quick formation of the $NiCo_2O_4$ on the surface. Afterwards, there are two forces in opposite directions affecting the formation of core-shell structures. The contracted force (F_c) induced by oxidative degradation of organic species in the structures,

generates the inward core. The other force, an adhesive force from the shell structures (F_a), hinders the further inward shrinkage of the precursor core. When Fc is dominant, the core structures will further contract inside and detach from the pristine shell. This phenomenon is called a heterogeneous contraction process. With the extension of the heating period, there is another core formed within the pristine one. By the same mechanism, the core-in-double shell $NiCo_2O_4$ structures were developed. These materials with mixed transition metal oxides were used as supercapacitor and LIBs electrodes, as the hollow and integrated structures provide excellent energy storage properties.

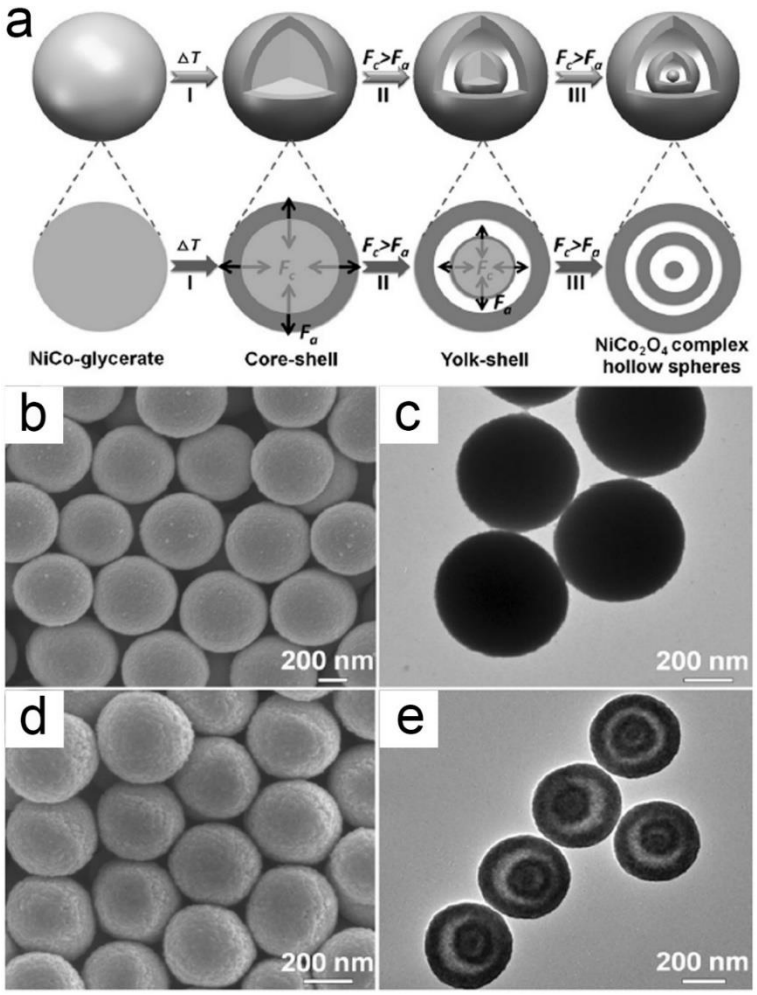

Figure 1. 6 Synthetic process of $NiCo_2O_4$ double core-shell hollow spheres. (b) SEM and (c) TEM images showing the pristine Ni-Co glycerate precusors; (c) SEM and (d) TEM images of the final products. [54] (Copyright Wiley-VCH Verlag GmbH & Co. KGaA. Reproduced with permission)

1.3.2 One-dimensional (1D) structures

1D nanostructures include nanowires, [67, 68] nanorods [69] and nanotubes. [70, 71] These materials with high length-diameter ratio have several merits when used in the fields of energy storage and conversion. Firstly, 1D nanostructures can be the building blocks for hierarchical structures, thus providing a nucleating site for other materials integrating multiple targets in one structure. Additionally, the large length-diameter ratio of specific materials could avoid the undesirable self-assembly issue as detected from most of the other structures. The uncontrollable self-aggregation phenomenon will decrease the effective electrochemical surface area of the nanostructured active materials to some extent. Moreover, 1D nanostructures enrich the candidates of electrode materials for next-generation flexible energy storage devices. The synthesis of 1D structures usually involves the surfactant-induced solvent-based wet chemistry. Transition metal ions often have different coordination environments with ligands and allow for many orientations for attachment. For instance, $NiCo_2O_4$ nanowires can be formed by hexa-coordination between Ni^{2+}/Co^{2+} and urea, while the nanosheets formed between these metal ions and methenamine. [72] Some other methods, such as chemical vapour deposition (CVD), can form 1D structures according to the seed mediated growth mechanism. One common example is the CVD-synthesized WO_3 nanorods, these materials were grown along the [001] direction. [73]

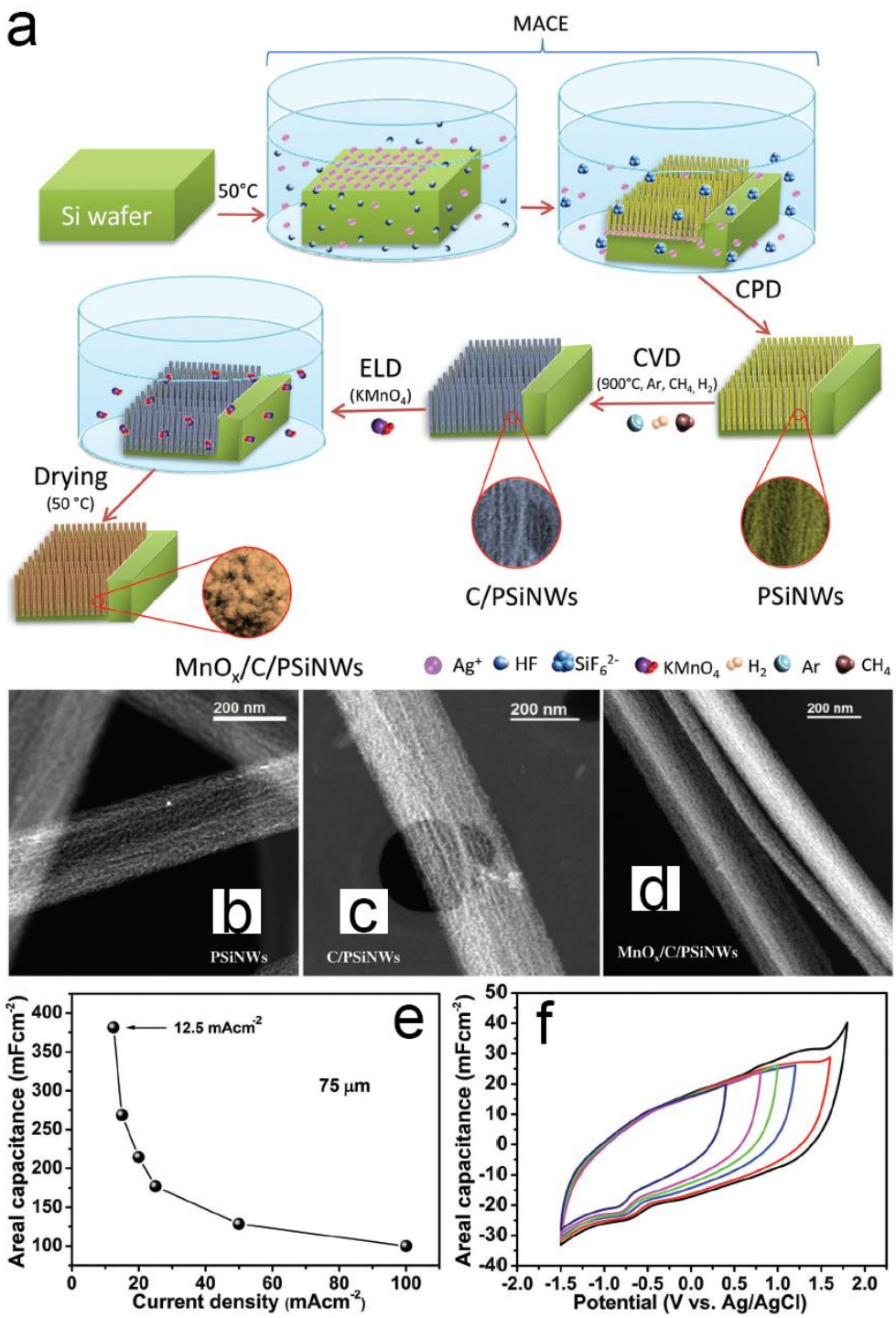

Figure 1. 7 (a) Synthetic procedure of fabrication nanowire-based electrodes; STEM-HADDF images of (b) porous Si nanowires (PSiNWs); (c) C/PSiNWs and (d) MnO_2/C/PSiNWs. (Abbreviation in the figures: CPD: commercial CO_2 supercritical point drying process; CVD: chemical vapour deposition; ELD: electroless deposition) (Copyright © 2017, Royal Society of Chemistry. Reproduced with permission)

Maboudian *et al.* developed the metal-assisted chemical etching route for the

synthesis porous silicon nanowires directly on current collectors (Figure 1.7) to limit the contact resistance compared to other nanostructured silicon. [22] Compared to the non-porous analogue, the specific surface areas increase more than 10 times (~ 24 m^2/g for non-porous one and ~ 342 m^2/g for porous silicon). Carbon coating was introduced by a CVD process to maintain the formation of the protection layer for silicon nanowires and maintain their high surface area and improve the electron conductivity. The MnO_x pseudocapacitance material was deposited by electrochemical deposition, which further improved the electrochemical energy storage properties. Asymmetric supercapacitors in ionic liquid electrolyte were assembled by using MnO_x/C/PSiNWs as the positive electrode and C/PSiNWs as the negative electrode, the devices delivered a high areal capacitance of ~ 375 mF cm^{-2} at a current density of 12.5 mA cm^{-2} within the potential range of 3 V.

1.3.3 Two-dimensional (2D) materials

2D materials, especially layered transition metal compounds and their derivatives, have attracted great research interest as emerging materials with graphite-like properties. [74] In these materials, the in-plane atoms are connected through chemical bonds while the inter-plane atoms are interacted by relatively weaker van der Waals force. A few transition metal oxides/hydroxides are layered structures in nature. For example, α-V_2O_5 consists of corner-sharing square pyramids and the open layered structure, it allows the flexibility for diffusion and transport of different ions, thus improving electrochemical energy storage properties, especially the rate performance when used as an electrode material.[75] Another example is the transition metal (Ni, Fe) double layer hydroxides (LDH),[76, 77] these materials deliver excellent electrocatalytic properties for oxygen evolution reaction (OER) due to their high surface area and easy exfoliation properties, which contributed to the enhanced electron-transfer,

electrolyte-accessibility and a large amount of exposed MO_6 catalytic sites for three-phase processes.

Ultrathin layered materials exhibit unique one to a few atomic layers, tunable compositions and superb physical, chemical and optical properties, thus leading to remarkable performances in various applications including energy storage and conversion. Transition metal chalcogenides are one of the important categories for 2D materials. [32, 33, 59, 74] These materials include ternary metal chalcogenides, alloyed chalcogenides, heteroatom-doped chalcogenides and heterostructured chalcogenides. Two schemes have been proposed for synthesizing 2D ultrathin transition metal chalcogenides, *i.e.* the top-down and bottom-up strategies.

The top-down method obtains ultrathin nanosheets from bulk materials. In general, different kinds of exfoliation approaches have been involved, including mechanical or sonication-assisted exfoliation and electrochemical/chemical Li intercalation-assisted exfoliation.

For example, Xie's group obtained Cu_2WS_4 ultrathin nanosheets by using n-butyl-lithium, as shown in Figure 1.8. [78] The intermediates of $Li_xCu_2WS_4$ were produced by the intercalation of Li ions into bulk Cu_2WS_4. Li ions were removed by a hydrolysis reaction in distilled water, hydrogen is generated within the layered structure and a further ultrasonication procedure produces further exfoliation in the ultrathin nanosheets structures. The thickness of the as-synthesized ultrathin nanosheets are ~ 1.0 nm, which exhibit high electron conductivity, reflected from an electrical resistivity test, thus making them a suitable candidate for flexible solid-state supercapacitor electrode materials.

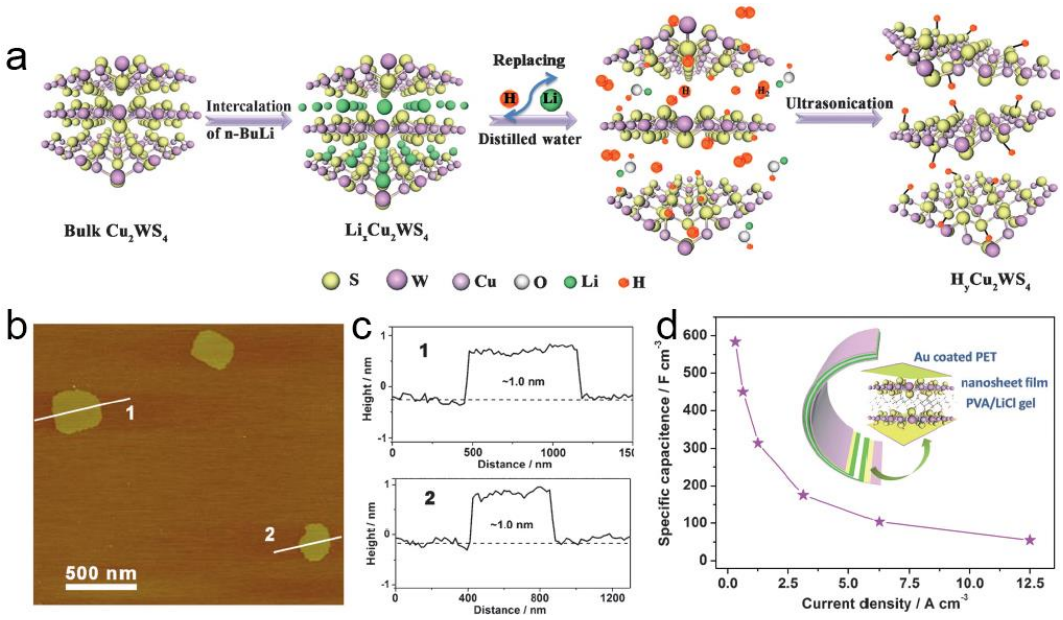

Figure 1. 8 (a) Schematic illustration of the synthetic procedure for hydrogenated Cu_2WS_4 ultrathin nanosheets; (b) Atomic force microscopy (AFM) image of the selected area for obtained samples and its corresponding height diagram in (c); (d) Capacitive performances for symmetrical supercapacitors based on hydrogenated Cu_2WS_4 as the active materials. [66] (Copyright Wiley-VCH Verlag GmbH & Co. KGaA. Reproduced with permission)

The bottom-up strategy of ultrathin nanosheets can be realized by chemical vapour deposition or chemical synthesis from small precursor molecules. In Figure 1.9, Zhou *el al.* reported a smart approach by using aerogels containing NaCl, $C_6H_8O_7$, NH_2CSNH_2 and $(NH_4)_6Mo_7O_{24}{\cdot}4H_2O$ as the precursors. [79] Due to the cubic structure of NaCl particles, the formed ultrathin Mo-C-N films uniformly cover the templates. The aerogels were then heated to decomposed to ultrathin MoS_2 nanosheets on carbon confined by stacked NaCl cubes. The as-prepared materials were washed several times to remove NaCl templates. MoS_2 nanosheets with 2-layer thicknesses on carbon have been purified and the materials used as the anode materials for LIBs, which outperformed commercial MoS_2 powders and MoS_2/C composites.

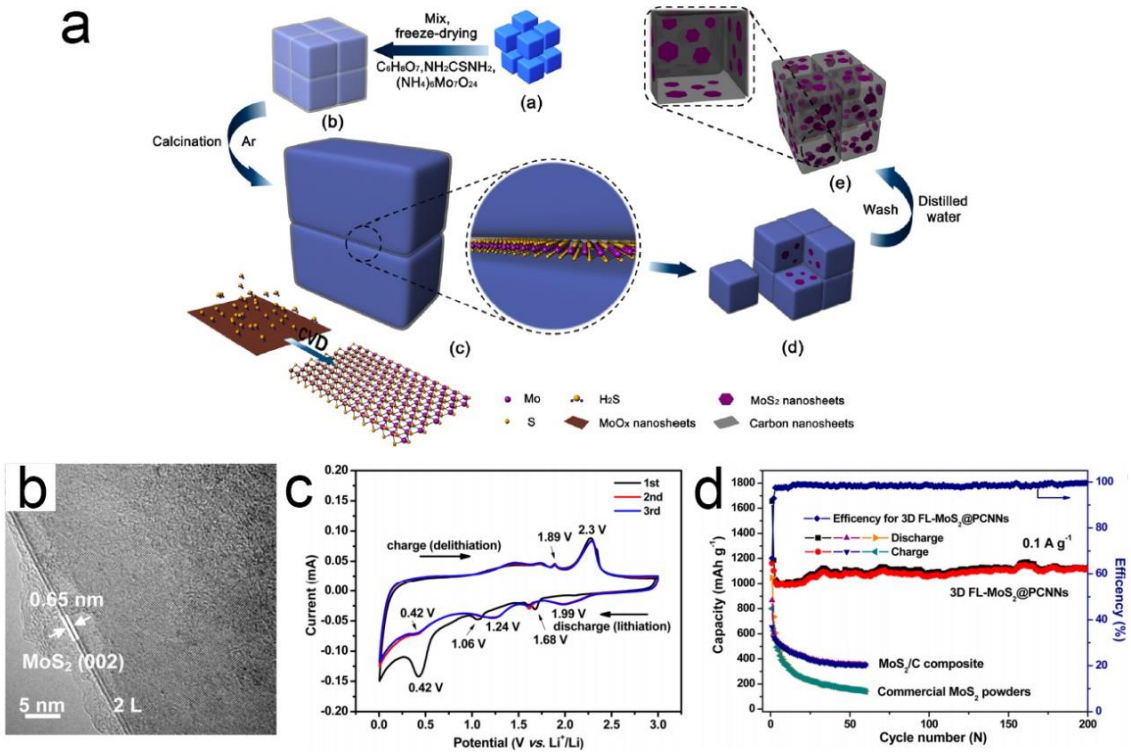

Figure 1. 9 Schematic illustration of synthetic procedure for MoS_2/C ultrathin nanosheets; (b) High-resolution transmittance electron microscopy (HRTEM) of as-synthesized materials; (c) cyclic voltammetry (CV) curves for MoS_2/C ultrathin nanosheets; (d) Comparison of the stability tests of as-synthesized materials and two counterparts. [67] (Copyright © 2015, American Chemical Society. Reproduced with permission)

1.3.4 Three-dimensional (3D) structures

3D hierarchical structures are the most widely used electrodes in energy storage and conversion application. [38, 39, 61, 62, 80, 81] These structures usually involve *in situ* synthesis of multiple active materials on the current collectors. It can avoid the use of conductive carbons and binders for bonding active materials and current collectors. This strategy can increase the utilized ratio of active materials to the largest extent, however, the rational design of the structure is of great importance. The stable structures enhance the cycling stability of the electrodes for batteries or supercapacitors. For instance, multi-component 3D structures usually involve several hierarchical structures (*i.e.* multiple core-shells), the structure stability of the inner parts is more important as they provide the

structural support for the whole electrodes. Moreover, due to the lack of extra electron conductive agents, fast ions and electron transfer should be considered into the design of components. Finally, enlarged specific surface area (or electrochemical active surface area) and electrophilic structures could be considered into the design, through which, large areas of interface between electrolytes (electrolyte/gas for energy conversion systems) and active materials can be realized, however the controllable synthesis of high surface area and highly active-materials-loading electrodes, to meet the requirement such as at an industrial level, is a challenge.

The emblematic hybrid 3D structure for integration of materials presenting synergetic effects is $ZnCo_2O_4$@$Ni_xCo_{2x}(OH)_{6x}$ core-shell structures on Ni foam by Fu *et al*. as shown in Figure 1.10. [82] The $ZnCo_2O_4$ nanowires were prepared by solvothermal reactions followed by an annealing process and was used as the support structures for the electrodeposition of $Ni_xCo_{2x}(OH)_{6x}$ nanosheets. Both core and shell structures are active components for electrochemical energy storage; moreover, the hierarchical structures utilized the interspace of the porous current collectors more efficiently. These advantages result in enlarged areal capacitance, reflected from larger closed area in the CV curves, and excellent rate performance (Figure 1.10f and g).

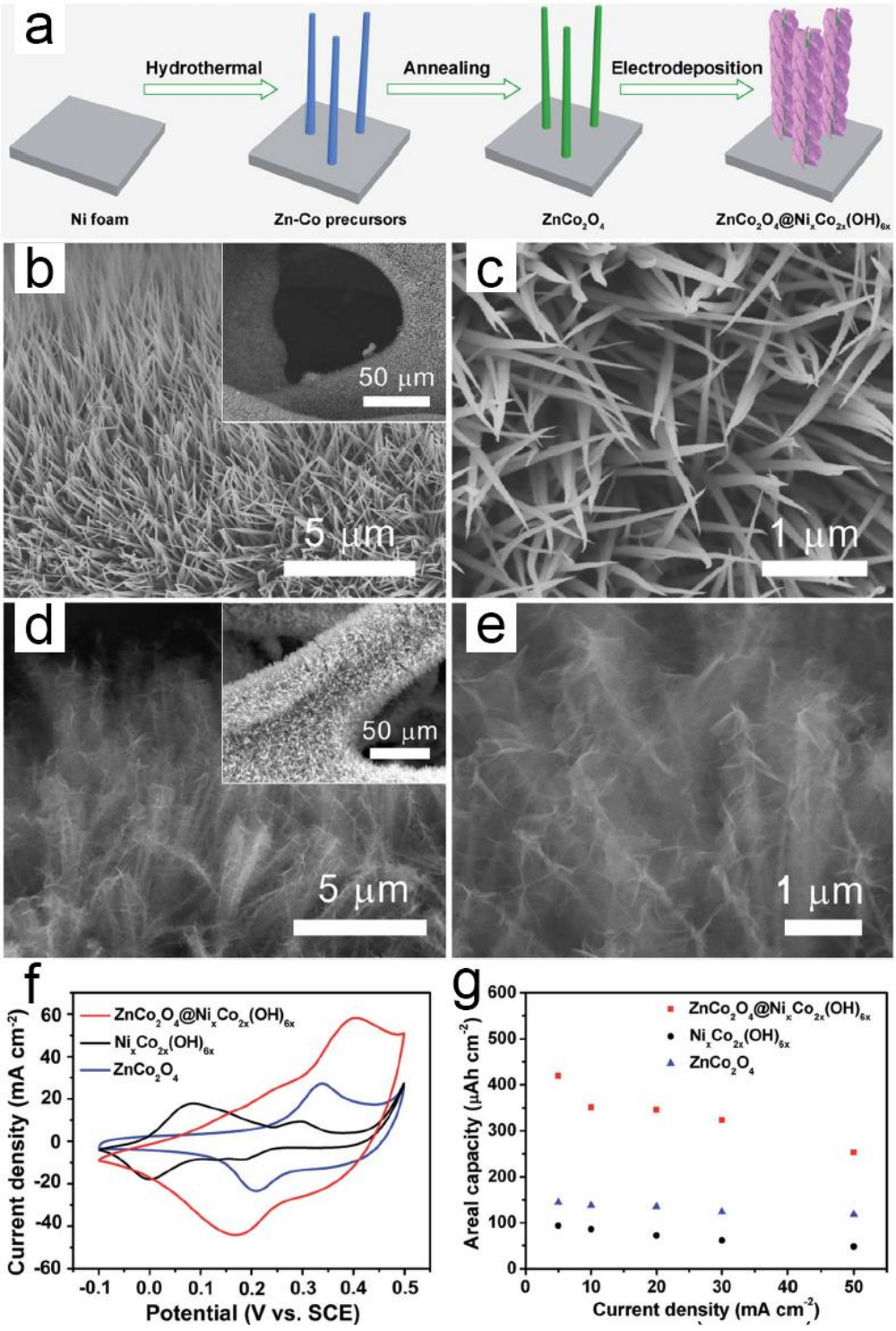

Figure 1. 10 (a) Schematic illustration of the synthetic procedure for $ZnCo_2O_4@Ni_xCo_{2x}(OH)_{6x}$ on Ni foam; SEM images of $Ni_xCo_{2x}(OH)_{6x}$ in (b) low-magnification and (c) high-magnification; SEM images of $ZnCo_2O_4@Ni_xCo_{2x}(OH)_{6x}$ core-shell structures in (d) low and (e) high magnification; (f) cyclic voltammetry (CV) curves of three comparable samples; (e) the areal capacity as a function of current density for these three electrodes. (Copyright © 2015, Royal Society of Chemistry. Reproduced with permission)

1.4 Summary

In this chapter, the classification of commonly used energy storage devices was introduced according to their different contributions as shown in a Ragone plot. Especially, supercapacitors and LIBs occupied a large area in the Ragone plot, as they can realize either high-energy or high-power densities. The energy storage mechanism and electrode materials of supercapacitors and LIBs were described in detail. Transition metals and their derivatives are playing important roles as electrode materials in both supercapacitors and LIBs. Chemical synthetic methods for different active materials for electrodes were then suggested. Despite the progress that has been made for different nanostructures from hollow to 3D electrodes, further improvements are needed to overcome the shortcomings of reported materials, such as the structural stability of hollow and hierarchical active materials. These improvements will promote the development of long-term high-capacity energy-storage devices.

In the following chapters, binder-free electrodes for electrochemical energy storage were designed. In Chapter 2, nickel oxides or cobalt oxides were extensively reported as pseudocapacitors, however their poor electron conductivity and rapid decline of specific capacitance hindered the application of these materials. Ternary transition metal oxides with multi-valance states improved the electron conductivity by several orders of magnitudes relative to that of binary metal oxides. $NiWO_4$ and $CoWO_4$ were directly synthesized on Ni foam as electrodes the first time, which outperformed the traditional slurry process of making electrodes. They showed superior specific capacitance and rate performances. The electrochemical performances of the as-assembled electrodes are among the top-tier of electrochemical performance compared to similar materials or nanostructures at the time of writing. However, several issues remained, tungsten contents contributed to enhance the electron conductivity, but no redox reactions happened within tungsten and the ions from the electrolyte.

Further modification and design of the electrode materials and fabrication and evaluation of the supercapacitor devices by the synthesized electrodes are required. In addition, the energy storage mechanism of nickel and cobalt-based materials in alkaline electrolytes are not clear. Therefore, ternary transition metal sulfides materials were synthesized in Chapter 3.

In Chapter 3, the electrochemical energy storage performances of nickel and cobalt-based materials in alkaline aqueous electrolyte were further improved by metal sulfides. It reports that metal sulfides materials delivered high electron conductivity compared to oxides counterparts, however, they can be oxidized easily and thus lose their advantages. In this work, the structural design around Ni-Co-S/SNGA materials were optimized to realize the best energy storage performance by means of controlling the ratios of Ni-Co-S and graphene aerogel and the ratios of nickel to cobalt contents. Especially, the optimized structure realized the high capacity and excellent cycling stability in alkaline aqueous electrolytes for electrochemical energy storage application compared to its counterparts, the validity of the structure was demonstrated in energy conversion (oxygen reduction reaction). The definition of the charge storage application was defined. However, the aerogel structures limit the areal/volumetric capacity/capacitance of the electrodes; as battery materials, nickel and cobalt-based materials are not promising candidates for pseudocapacitors. Ni foam as the current collectors are not suitable for bendable energy storage devices. Further seeking promising pseudocapacitor materials to realize high areal capacitance and flexible devices applications was conducted in Chapter 4.

Several tungsten-based materials were reported to deliver excellent pseudocapacitance. Metal nitrides were formed that exhibited metallic electron conductivity. However, no comprehensive work was done related to using tungsten nitride materials for pseudocapacitor electrodes and uncovering the merits of these materials compared to their oxide counterpart. In Chapter 4,

W_2N@C nanoarray core-shell structures were synthesized on carbon fiber clothes by combining aerosol-assisted chemical vapour deposition (AACVD) and annealing approaches in ammonia gas. The carbon fibre cloth was introduced as the bendable and flexible current collectors with relatively larger surface area compared to metal foils. W_2N@C electrodes possess a high areal capacitance and can be used for flexible devices application. The advantages of W_2N materials compared to WO_{3-x} were revealed by analysis of electrochemical results, computational simulation and *in-situ* transmission electron microscope. Finally, the as-assembled electrodes were fabricated for flexible supercapacitors with solid state electrolytes and manufactured into coin cells with ionic liquid electrolyte for high working voltage applications. The successful application of carbon cloths in flexible electrodes technique stimulate the work by using it for flexible LIBs application, thus much higher specific capacity can be realized. In Chapter 5, 3D nanostructures were designed on carbon cloth to realize high-performance cathodes for LIBs.

As known, the specific capacity based on the mass of cathode materials are much lower than that of anodes due to their intrinsic Li-ion intercalation. The research of cathode materials has attracted great interest. V_2O_5 materials with multi-Li intercalation properties are one of the promising cathodes materials due to their high theoretical specific capacitance. The $NiCo_2O_4$@V_2O_5 sandwich structures were designed in Chapter 5, which took account of the structural stability, Li-ion diffusivity and the ratio of electron conductive contribution and capacitance contribution components of the electrode materials.

In the end, the summary of the whole PhD project and the perspective of the structural design based on transition metal materials and their derivatives are presented, and further research work proposed.

1.5 References

[1] S. Chu, A. Majumdar, *Nature* **2012**, *488*, 294.

[2] L. Georgeson, M. Maslin, M. Poessinouw, *Nature* **2016**, *538*, 27.

[3] J. B. Goodenough, *Energy Storage Mater.* **2015**, *1*, 158.

[4] B. Dunn, H. Kamath, J. M. Tarascon, *Science* **2011**, *334*, 928.

[5] P. Simon, Y. Gogotsi, *Nat. Mater.* **2008**, *7*, 845.

[6] P. Huang, C. Lethien, S. Pinaud, K. Brousse, R. Laloo, V. Turq, M. Respaud, A. Demortière, B. Daffos, P. L. Taberna, B. Chaudret, Y. Gogotsi, P. Simon, *Science* **2016**, *351*, 691.

[7] H. S. Kim, J. B. Cook, H. Lin, J. S. Ko, S. H. Tolbert, V. Ozolins, B. Dunn, *Nat. Mater.* **2017**, *16*, 454.

[8] J. B. Goodenough, *Acc. Chem. Res.* **2013**, *46*, 1053.

[9] T. Koketsu, J. Ma, B. J. Morgan, M. Body, C. Legein, W. Dachraoui, M. Giannini, A. Demortiere, M. Salanne, F. Dardoize, H. Groult, O. J. Borkiewicz, K. W. Chapman, P. Strasser, D. Dambournet, *Nat. Mater.* **2017**, *16*, 1142.

[10] J. H. Montoya, L. C. Seitz, P. Chakthranont, A. Vojvodic, T. F. Jaramillo, J. K. Norskov, *Nat. Mater.* **2016**, *16*, 70.

[11] J. P. Lemmon, *Nature* **2015**, *525*, 447.

[12] S. Chu, Y. Cui, N. Liu, *Nat. Mater.* **2016**, *16*, 16.

[13] T. Christen, M. W. Carlen, *J. Power Sources* **2000**, *91*, 210.

[14] P. Simon, Y. Gogotsi, B. Dunn, *Science* **2014**, *343*, 1210.

[15] M. Salanne, B. Rotenberg, K. Naoi, K. Kaneko, P. L. Taberna, C. P. Grey, B. Dunn, P. Simon, *Nat. Energy* **2016**, *1*, 16070.

[16] Z. Lin, E. Goikolea, A. Balducci, K. Naoi, P. L. Taberna, M. Salanne, G. Yushin, P. Simon, *Mater. Today* **2018**, *21*, 419.

[17] M. V. Fedorov and A. A. Kornyshev, *Chem. Rev.* **2014**, *114*, 2978.

[18] B. E. Conway, Electrochemical Supercapacitors, *Springer* **1999**.

[19] A. G. Pandolfo, A. F. Hollenkamp, *J. Power Sources* **2006**, *157*, 11.

[20] G. Cai, P. Darmawan, M. Cui, J. Wang, J. Chen, S. Magdassi, P. S. Lee, *Adv.*

Energy Mater. **2016**, *6*, 1501882.

[21] Z. F. Huang, J. Song, L. Pan, X. Zhang, L. Wang, J. J. Zou, *Adv. Mater.* **2015**, *27*, 5309.

[22] S. Ortaboy, J. P. Alper, F. Rossi, G. Bertoni, G. Salviati, C. Carraro, R. Maboudian, *Energy Environ. Sci.* **2017**, *10*, 1505.

[23] V. Augustyn, P. Simon, B. Dunn, *Energy Environ. Sci.* **2014**, *7*, 1597.

[24] L. Wang, H. Yang, X. Liu, R. Zeng, M. Li, Y. Huang, X. Hu, *Angew. Chem. Int. Ed. Engl.* **2017**, *56*, 1105.

[25] C. O. Baker, X. Huang, W. Nelson, R. B. Kaner, *Chem. Soc. Rev.* **2017**, *46*, 1510.

[26] M. V. Reddy, G. V. Subba Rao, B. V. Chowdari, *Chem. Rev.* **2013**, *113*, 5364.

[27] C. K. Chan, H. Peng, G. Liu, K. McIlwrath, X. F. Zhang, R. A. Huggins, Y. Cui, *Nat. Nanotechnol.* **2008**, *3*, 31.

[28] H. Wu, G. Zheng, N. Liu, T. J. Carney, Y. Yang, Y. Cui, *Nano Lett*. **2012**, *12*, 904.

[29] N. Kim, S. Chae, J. Ma, M. Ko, J. Cho, *Nat. Commun*. **2017**, *8*, 812.

[30] M. Acerce, D. Voiry, M. Chhowalla, *Nat. Nanotechnol.* **2015**, *10*, 313.

[31] B. Anasori, M. R. Lukatskaya, Y. Gogotsi, *Nat. Rev. Mater.* **2017**, *2*, 16098.

[32] R. Lv, J. A. Robinson, R. E. Schaak, D. Sun, Y. Sun, T. E. Mallouk, M. Terrones, *Acc. Chem. Res.* **2015**, *48*, 56.

[33] S. Manzeli, D. Ovchinnikov, D. Pasquier, O. V. Yazyev, A. Kis, *Nat. Rev. Mater.* **2017**, *2*, 17033.

[34] G. A. Muller, J. B. Cook, H. S. Kim, S. H. Tolbert, B. Dunn, *Nano Lett.* **2015**, *15*, 1911.

[35] A. A. Tedstone, D. J. Lewis, P. O'Brien, *Chem. Mater.* **2016**, *28*, 1965.

[36] L. Yu, H. B. Wu, X. W. Lou, *Acc. Chem. Res.* **2017**, *50*, 293.

[37] C. Yuan, H. B. Wu, Y. Xie, X. W. Lou, *Angew. Chem. Int. Ed. Engl.* **2014**, *53*, 1488.

[38] S. Zheng, X. Li, B. Yan, Q. Hu, Y. Xu, X. Xiao, H. Xue, H. Pang, *Adv. Energy Mater.* **2017**, *7*, 1602733.

[39] Y. Zhong, X. Xia, F. Shi, J. Zhan, J. Tu, H. J. Fan, *Adv. Sci.* **2016**, *3*, 1500286.

[40] L. Ping, D. S. Chung, J. Bouffard, S. G. Lee, *Chem. Soc. Rev.* **2017**, *46*, 4299.

[41] G. Tian, X. Zhang, X. Zheng, W. Yin, L. Ruan, X. Liu, L. Zhou, L. Yan, S. Li, Z. Gu, Y. Zhao, *Small* **2014**, *10*, 4160.

[42] K. Manthiram, A. P. Alivisatos, *J. Am. Chem. Soc.* **2012**, *134*, 3995.

[43] D. I. Khomskii, Transition Metal Compounds, *Cambridge University Pres* **2014**.

[44] C. E. Housecroft, A. G. Sharpe, Inorganic Chemistry, *Pearson Education Limited* **2008**.

[45] J. Chen, B. Yao, C. Li, G. Shi, *Carbon* **2013**, *64*, 225.

[46] L. Chen, X. Dong, Y. Wang, Y. Xia, *Nat. Commun*. **2016**, *7*, 11741.

[47] Z. Yan, H. Sun, X. Chen, H. Liu, Y. Zhao, H. Li, W. Xie, F. Cheng, J. Chen, *Nat. Commun.* **2018**, *9*, 2373.

[48] X. Zheng, B. Zhang, P. De Luna, Y. Liang, R. Comin, O. Voznyy, L. Han, F. P. Garcia de Arquer, M. Liu, C. T. Dinh, T. Regier, J. J. Dynes, S. He, H. L. Xin, H. Peng, D. Prendergast, X. Du, E. H. Sargent, *Nat. Chem.* **2018**, *10*, 149.

[49] C. Liu, Z. G. Neale, G. Cao, *Mater. Today* **2016**, *19*, 109.

[50] A. Manthiram, J. C. Knight, S.-T. Myung, S.-M. Oh, Y.-K. Sun, *Adv. Energy Mater.* **2016**, *6*, 1501010.

[51] L. Dimesso, C. Forster, W. Jaegermann, J. P. Khanderi, H. Tempel, A. Popp, J. Engstler, J. J. Schneider, A. Sarapulova, D. Mikhailova, L. A. Schmitt, S. Oswald, H. Ehrenberg, *Chem. Soc. Rev.* **2012**, *41*, 5068.

[52] Q. D. Truong, M. K. Devaraju, T. Tomai, I. Honma, *ACS Appl. Mater. Interfaces* **2013**, *5*, 9926.

[53] Y. Feng, H. Zhang, L. Fang, Y. Ouyang, Y. Wang, *J. Mater. Chem. A* **2015**, *3*, 15969.

[54] H. Zheng, J. Z. Ou, M. S. Strano, R. B. Kaner, A. Mitchell, K. Kalantar-zadeh, *Adv. Funct. Mater.* **2011**, *21*, 2175.

[55] Q. Wang, A. Puntambekar, V. Chakrapani, *Nano Lett.* **2016**, *16*, 7067.

[56] J. L. Wang, Y. R. Lu, H. H. Li, J. W. Liu, S. H. Yu, *J. Am. Chem. Soc.* **2017**, *139*, 9921.

[57] A. Djire, O. T. Ajenifujah, A. E. S. Sleightholme, P. Rasmussen, L. T. Thompson, *J. Power Sources* **2015**, *275*, 159.

[58] L. Mai, X. Tian, X. Xu, L. Chang, L. Xu, *Chem. Rev.* **2014**, *114*, 11828.

[59] X. Zhang, L. Hou, A. Ciesielski, P. Samorì, *Adv. Energy Mater.* **2016**, *6*, 1600671.

[60] H. Sun, L. Mei, J. Liang, Z. Zhao, C. Lee, H. Fei, M. Ding, J. Lau, M. Li, C. Wang, X. Xu, G. Hao, B. Papandrea, I. Shakir, B. Dunn, Y. Huang, X. Duan, *Science* **2017**, *356*, 599.

[61] Y. Q. Li, J. C. Li, X. Y. Lang, Z. Wen, W. T. Zheng, Q. Jiang, *Adv. Funct. Mater.* **2017**, *27*, 1700447.

[62] S. Zhu, J. Li, X. Deng, C. He, E. Liu, F. He, C. Shi, N. Zhao, *Adv. Funct. Mater.* **2017**, *27*, 1605017.

[63] L. Zhou, Z. Zhuang, H. Zhao, M. Lin, D. Zhao, L. Mai, *Adv. Mater.* **2017**, *29*, 1602914.

[64] X. Wang, J. Feng, Y. Bai, Q. Zhang, Y. Yin, *Chem. Rev.* **2016**, *116*, 10983.

[65] S. Wang, B. Y. Guan, X. W. Lou, *Energy Environ. Sci.* **2018**, *11*, 306.

[66] L. Shen, L. Yu, X. Y. Yu, X. Zhang, X. W. Lou, *Angew. Chem. Int. Ed. Engl.* **2015**, *54*, 1868.

[67] W. Ma, S. Chen, S. Yang, W. Chen, Y. Cheng, Y. Guo, S. Peng, S. Ramakrishna, M. Zhu, *J. Power Sources* **2016**, *306*, 481.

[68] M. Yu, Z. Wang, C. Hou, Z. Wang, C. Liang, C. Zhao, Y. Tong, X. Lu. S. Yang, *Adv. Mater.* **2017**, *29*, 1602868.

[69] R. Li, Y. Wang, C. Zhou, C. Wang, X. Ba, Y. Li, X. Huang, J. Liu, *Adv. Funct. Mater.* **2015**, *25*, 5384.

[70] S. Mehraeen, A. Tasdemir, S. A. Gursel, A. Yurum, *Nanotechnology* **2018**, *29*, 255402.

[71] N. Wang, Z. Bai, Y. Qian, J. Yang, *Adv. Mater.* **2016**, *28*, 4126.

[72] W. Li, B. Zhang, R. Lin, S. Ho-Kimura, G. He, X. Zhou, J. Hu, I. P. Parkin,

Adv. Funct. Mater. **2018**, *28*, 1705937.

[73] C. Sotelo-Vazquez, R. Quesada-Cabrera, M. Ling, D. O. Scanlon, A. Kafizas, P. K. Thakur, T.-L. Lee, A. Taylor, G. W. Watson, R. G. Palgrave, J. R. Durrant, C. S. Blackman, I. P. Parkin, *Adv. Funct. Mater.* **2017**, *27*, 1605413.

[74] E. Pomerantseva, Y. Gogotsi, *Nat. Energy* **2017**, *2*, 17089.

[75] P. Liu, K. Zhu, Y. Gao, H. Luo, L. Lu, *Adv. Energy Mater.* **2017**, *7*, 1700547.

[76] Y. Hou, M. R. Lohe, J. Zhang, S. Liu, X. Zhuang, X. Feng, *Energy Environ. Sci.* **2016**, *9*, 478.

[77] Y. Jia, L. Zhang, G. Gao, H. Chen, B. Wang, J. Zhou, M. T. Soo, M. Hong, X. Yan, G. Qian, J. Zou, A. Du, X. Yao, *Adv. Mater.* **2017**, *29*, 1700017.

[78] X. Hu, W. Shao, X. Hang, X. Zhang, W. Zhu, Y. Xie, *Angew. Chem. Int. Ed. Engl.* **2016**, *55*, 573.

[79] J. Zhou, J. Qin, X. Zhang, C. Shi, E. Liu, J. Li, N. Zhao, C. He, *ACS Nano* **2015**, *9*, 3837.

[80] X. Xia, C. Zhu, J. Luo, Z. Zeng, C. Guan, C. F. Ng, H. Zhang, H. J. Fan, *Small* **2014**, *10*, 766.

[81] Q. Zhang, J. Wang, J. Dong, F. Ding, X. Li, B. Zhang, S. Yang, K. Zhang, *Nano Energy* **2015**, *13*, 77.

[82] W. Fu, Y. Wang, W. Han, Z. Zhang, H. Zha, E. Xie, *J. Mater. Chem. A* **2016**, *4*, 173.

Chapter 2

Ni foam supported $NiWO_4$ and $CoWO_4$ nanostructures for supercapacitor electrodes

2.1 Introduction

As discussed in Chapter 1, supercapacitors consist of two categories: electrical double layer capacitors (EDLCs) and pseudocapacitors (PCs). [1] The electrode materials for EDLCs, such as multi-porous nanostructured carbon, employ reversible ion-absorption/desorption from the electrolyte on the surface of electrodes. In comparison with EDLCs, PCs deliver larger gravimetric capacitance due to fast and reversible surface redox reactions among ions from electrolyte and multiple valence states of the electrode materials, mostly transition metal oxides (TMOs). Previous effort has been focused on discovery and design of binary TMOs for electrodes in PCs, such as NiO, [2,3] CoO, [4] RuO_2, [5] MnO_2, [6] and WO_3[7].

Nevertheless, the limitation of electrical conductivity of most binary TMOs has caused poor electrochemical performance, especially low specific capacitance and rate performance of the electrodes. Ternary TMOs with two species of metal cations are prospective candidates for electrochemical energy storage. The integration of two kinds of TM cations could improve the electrical conductivity to a large extent and provide multiple valance states compared to the individual binary oxides thus potentially inducing improvements in electrochemical energy storage properties. Therefore, different compositions of ternary TMOs with controlled nanostructures have been designed and synthesized and presented better electrochemical performance, such as $NiCo_2O_4$, [8,9] $CoMoO_4$,[10] $NiFe_2O_4$,[11] and $MnCo_2O_4$.[12] The design and synthesis of innovative nanostructures of ternary TMOs with excellent electrochemical properties is still an interesting research field. Transition metal tungstates present high electrical conductivity, better than individual binary counterparts and some reported ternary TMOs. For instance, $NiWO_4$ presents an electrical conductivity at the range of 10^{-7}-10^{-2} S cm^{-1}, several magnitudes higher than that of NiO (10^{-13} S cm^{-1}) [13,14] and $NiMoO_4$ (10^{-11}-$10^{-4.5}$ S cm^{-1}) [15,16]. Furthermore, W exhibits various valence

states, [17] which have potential use for redox reactions as electrodes for PCs.

$NiWO_4$ and $CoWO_4$ have been considered as encouraging candidates for catalytic applications, including photocatalysts and electrocatalysts. [18,19] However, literature relating to use of these materials in supercapacitor electrodes are less reported compared to NiO and CoO/Co_3O_4. One previous work prepared amorphous $NiWO_4$ nanostructures *via* a co-precipitation process as electrodes for supercapacitors.[13] The relationship between synthetic temperatures and specific capacitance was studied. The reported highest gravimetric capacitance for nanostructured $NiWO_4$ electrodes was 586.2 F g^{-1} at the current density of 0.5 A g^{-1}. It is noted that amorphous $NiWO_4$ nanoparticles showed an improvement of electrical conductivity due to the combination of tungsten and nickel atoms compared to NiO. $CoWO_4$/graphene hybrids for supercapacitor electrodes were prepared through solvothermal reactions by Ye *et al.* [20] The materials realized a gravimetric capacitance of 159.9 F g^{-1} from CV test at a scan rate of 5 mV s^{-1} and the performance retention of ~ 94.7% after 1000 cycles. In spite of these attempts, the synthesis of $NiWO_4$ and $CoWO_4$ materials for electrodes by a facile procedure and further improvement of their electrochemical energy storage performance are remaining challenges. Recently, an effective approach was proposed to integrate active materials with current collectors, they have been termed binder-free electrodes. This tactic avoids the complicated slurry electrodes procedure for coating of powder materials. Furthermore, it can significantly increase the electrical conductivity by reducing the contact resistance among active materials and current collectors, thus massively improving the electrochemical performance of active materials. [21-23]

In this chapter, an easily-controlled one-step hydrothermal approach of synthesizing Ni foam supported nanostructured $NiWO_4$ and $CoWO_4$ as binder-free electrodes was developed. Their electrochemical properties as electrodes for PCs were fully investigated and compared with the powdery counterparts. It

was verified that the binder-free electrodes display high specific capacitance (797.8 F g^{-1} and 764.4 F g^{-1} for Ni foam supported $NiWO_4$ and $CoWO_4$ from galvanostatic charge-discharge (GCD) test at the current density of 1 A g^{-1}, respectively), remarkable rate capability (55.6% and 50.6% retention for Ni foam supported $NiWO_4$ and $CoWO_4$ with the current density increases of 20 times, respectively) and exceptional long-term performance (capacitance more than 200% compared to the initial specific capacitance after 6000 cycles). In comparison to the previous reported $NiWO_4$ and $CoWO_4$ electrodes for PCs, $NiWO_4$/Ni foam and $CoWO_4$/Ni foam nanostructures in this chapter show favorable electrochemical energy storage properties.

2.2 Experimental section

2.2.1 Electrode Synthesis

The chemicals are of analytical grade, obtained from Sigma (U.K.) and Sinopharm Chemical Reagent Co. (Shanghai, China) and used without further purification. At first, several pieces of Ni foam (~ 4 × 1 cm) were washed by 6 M hydrochloric acid under ultrasonic vibration to remove surface oxide layers and then with deionized water followed by vacuum drying at 100 ^oC. Then, 0.291 g of $Ni(NO_3)_2•6H_2O$ or $Co(NO_3)_2•6H_2O$ as the nickel and cobalt sources were dissolved in 40 mL of deionized water to form light green and pink precursor solutions, respectively. Afterwards, 0.33 g of Na_2WO_4 was dissolved into the above solutions and magnetically stirred for ~ 30 min. The Ni^{2+}/Co^{2+}, WO_4^{2-} solutions were transferred into a 60 mL Teflon-lined stainless-steel autoclaves with a piece of Ni foam standing against the inner-side, respectively. The autoclaves were closed and kept in an oven at 180 ^oC for 8 h. Finally, Ni foam supported nanostructures were washed with distilled water and absolute ethanol consecutively to move loosely attached powders and vacuum dried at 60 ^oC for

6 h.

2.2.2 Characterization

The morphology, phases and chemical states of as-synthesized electrodes were studied using a scanning electron microscope (SEM; Hitachi S-4800) using an accelerating voltage of 5 kV, a transmission electron microscope (TEM; JEM-2100F; accelerating voltage of 200 kV) equipped with an energy dispersive X-ray spectrometer (EDS), a D/max-2550 PC X-ray diffractometer (XRD; Rigaku, Cu-K_a radiation), and Raman Spectroscopy (Renishaw Raman microscope spectrometer with laser wavelength of 488 nm). The mass of the electrode materials was weighed accurately by an XS analytical balance (Mettler Toledo; δ = 0.01 mg).

2.2.3 Electrochemical Tests

Electrochemical measurements of as-prepared binder-free electrodes were characterized on an Autolab potentiostat (PGSTAT302N) in a three-electrode configuration. A platinum (Pt) plate, a Ag/AgCl electrode and 2 M KOH were used as the counter, reference electrodes and electrolyte, respectively. The Ni foam supported $NiWO_4$ or $CoWO_4$ nanostructures were tested as the working electrode directly. The mass loading of the active materials is ~ 0.75 mg cm^{-2} and ~ 2 cm^2 of the nickel foams in the electrolyte were performed the test.

2.2.4 Preparation of the working electrodes for powder samples

At first, $NiWO_4$ or $CoWO_4$ (80 wt%) powder samples were mixed with conductive agents (acetylene black; 15 wt%) and binder solutions (poly(tetrafluoroethylene); 5 wt%, calculated based on a solution of PTFE in water). Then, the mixture was moved to a small bottle with a few drops of ethanol and magnetically stirred over 8 hours to form a uniform slurry. After which, the slurry was pasted and pressed onto cleaned Ni foams (current collector) by a spatula with an area of ~ 2 cm^2 and

dried at 100 °C under vacuum overnight to remove the solvent. The electrodes were pressed under 10 MPa to enhance physical contact with the current collector. The test of the electrochemical performance is the same as the binder-free electrodes testing by using them as working electrodes.

2.2.5 Weighing active materials

The active materials were weighed by the following method: At first, the mass of a cleaned Ni foam was recorded by a XS analytical balance (Mettler Toledo; accuracy: +/- 0.01 mg) and noted as m_a. Then, the Ni foam was put into the autoclaves for reaction; after that, the Ni foam with active materials were washed and dried overnight under vacuum at 60 °C. The mass was weighed by analytical balance and noted as m_b. Finally, the weight of active materials on the electrodes were calculated according to $m_{material} = m_b - m_a$. As the electrode for testing is 2 cm^2 and the total area of Ni foam is 4 cm^2. The mass for testing is $m_{test} = 0.5 \times m_{material}$.

The weight of the powder samples on Ni foam was calculated as follows: Firstly, a piece of cleaned Ni foam was weighed as m_c. Then, after the slurry was pasted, dried and pressed on the Ni foam, the mass was weighed as m_d. Finally, the mass of the powdery electrode materials was calculated according to the equation: $m_{powder} = 0.8 \times (m_d - m_c)$.

2.3 Results and discussion

The Ni foam supported nanostructured $NiWO_4$ and $CoWO_4$ were synthesized by one-step hydrothermal process. The facile preparation method can be regarded as a highly manageable and environmentally benign technique for mass and cut-price production of electrode materials. Self-assembled nanostructures consisting of small individual nanoparticles were coated on the Ni foam uniformly,

as shown in Figure 1 and confirmed by the following analysis.

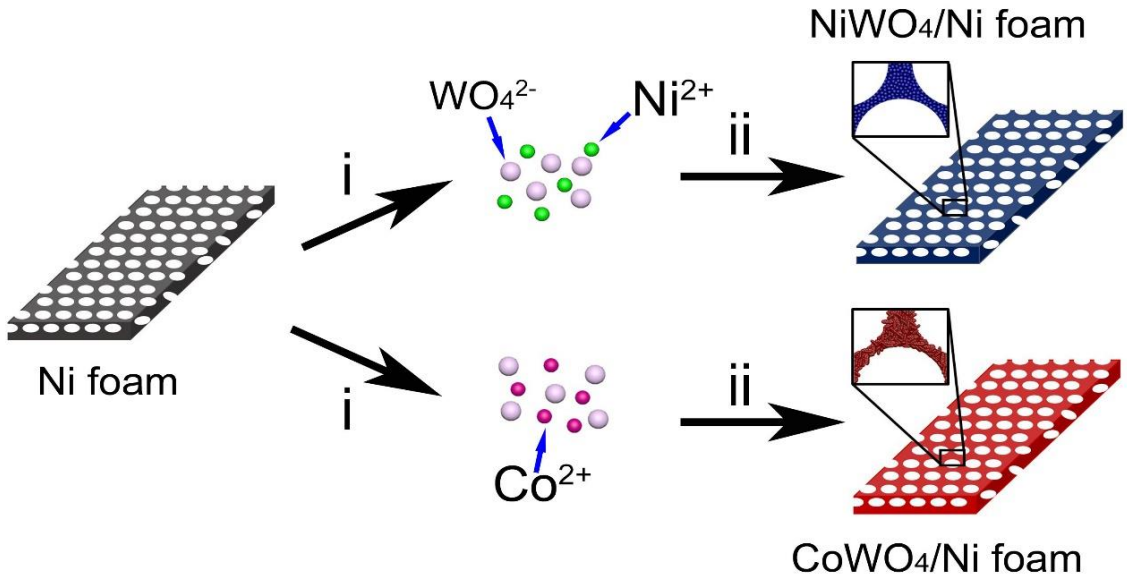

Figure 2. 1 Schematic illustration of the one-step hydrothermal synthesis of self-assembled Ni foam supported $NiWO_4$ and $CoWO_4$ electrodes.

The morphologies of the as-obtained electrodes were examined by scanning electron microscopy (SEM). Commercial nickel foam still preserved its 3D porous structures after washing with hydrochloric acid to remove the surface oxide layer and the hydrothermal reactions with the precursor solution (Figure 2.1 a, b). Ni foam was employed as the current collector due to its interlaced microporous structures affording a large supporting surface area, competent pathways of ion and electron transfer for active materials and superb metallic electrical conductivity. After the hydrothermal reactions, the nanostructures covered the substrates evenly with no bare Ni foam being observed, as illustrated by lower magnification SEM (Figure 2.2c, d). Figure 2.3 a and c are SEM images in nanometer scale of nickel foam supported $NiWO_4$ and $CoWO_4$ structures, respectively. From the high magnification SEM image in Figure 2.3b, the morphology of $NiWO_4$ nanostructures presented hill-like hemispheres consisting of a lot of small assembled nanoparticles with the size of 100-200 nm. The high magnification SEM image of $CoWO_4$ nanostructures is presented in Figure 2.3d.

$CoWO_4$ nanoparticles presented shuttle-like structures with coarse surfaces made of individual structures with the length of ~ 100 nm and width of ~ 50 nm. As for the electrode materials for supercapacitors, their crude morphologies provide appropriate active species for redox reactions and an improved contacting area with the ions from electrolyte during the process of electrochemical energy storage.

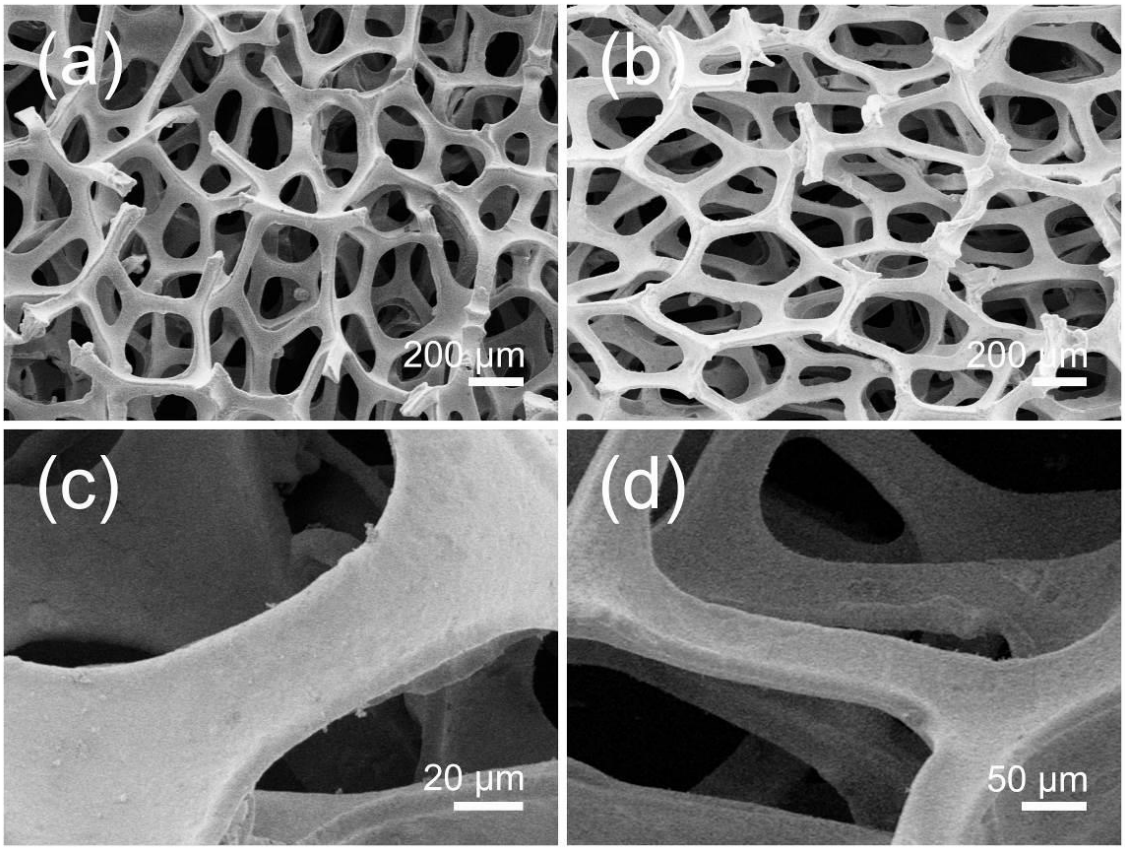

Figure 2. 2 (a), (b) SEM images of Ni foam supported $NiWO_4$ and $CoWO_4$ in micro-scale magnification, respectively; (c), (d) SEM image of $NiWO_4$ and $CoWO_4$/Ni foam, in higher magnification, respectively.

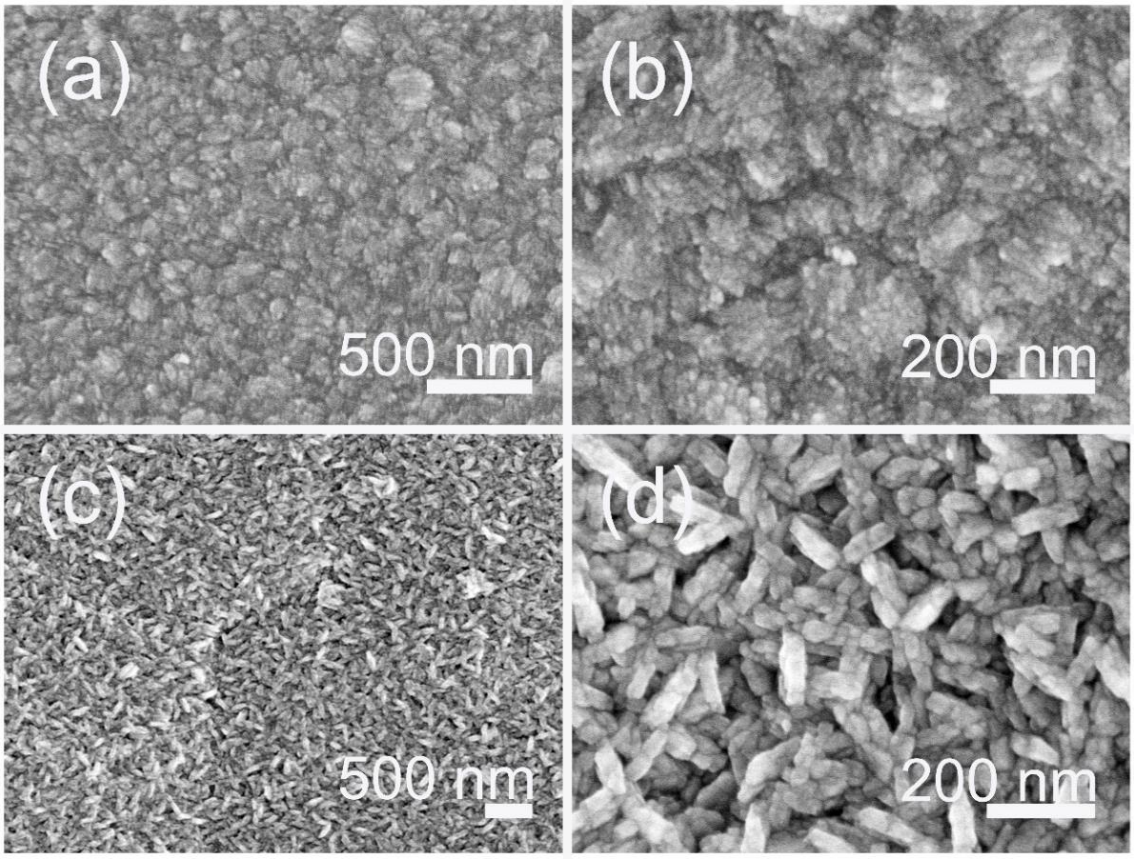

Figure 2. 3 SEM images of $NiWO_4$ nanoparticles/Ni foam in (a) low and (b) high magnifications and $CoWO_4$ nano-shuttles/Ni foam in (c) low and (d) high magnifications, respectively.

The nanostructures and morphologies of active materials were further exemplified by transmission electron microscopy (TEM) combined with an energy dispersive X-ray spectrometer (EDS). The preparation of TEM samples were conducted through detaching $NiWO_4$ and $CoWO_4$ nanoparticles from Ni foam by strong ultrasonic vibration in ethanol solution for half an hour. Obviously, the larger $NiWO_4$ hill-like nanostructures detected from the SEM are made up of multiple small nanoparticles and the nanostructured $CoWO_4$ are composed of plenty of tiny nanoshuttles. TEM images of $NiWO_4$ and $CoWO_4$ nanoparticles are shown in Figure 2.4a and c, respectively. The sizes of specific nanoparticles are ~15 nm for $NiWO_4$ samples and a length of ~50 nm and a width of ~25 nm for $CoWO_4$ nanoshuttles, in accordance with self-assembled uneven morphologies shown in SEM images, thus resulting in entire structures full of multi-scale

porosity. HRTEM of $NiWO_4$ nanoparticles in Figure 2.4b presented apparent lattice fringe with interplanar spacing (d-spacing) of 0.37 and 0.36 nm, corresponding to {011}, {110} planes of the $NiWO_4$ crystals, respectively. The inset showing fast Fourier transformation (FFT) pattern from this HRTEM image attribute to the $[1\bar{1}1]$ zone axis of the $NiWO_4$ monoclinic crystal. The HRTEM of nanostructured $CoWO_4$ are shown in Figure 3d, the d-spacing of 0.29 and 0.36 nm can be indexed as the distance of $\{\bar{1}11\}$, {011} planes of $CoWO_4$ crystals, the inset FFT pattern from the HRTEM image can correspond to the $[01\bar{1}]$ zone axis of the $CoWO_4$ monoclinic crystal. The EDS analyses (Figure 2.4e, f) demonstrate information on the Cu and C from the sample grid and the appearance of Ni/Co, W, O elements from the nanostructures.

The phases of $NiWO_4$ and $CoWO_4$ electrode materials were further discovered by X-ray Diffraction (XRD). The samples were prepared by scratching nanostructures from the Ni foams to avoid the strong background of the substrate on the signals of the diffraction. The diffraction pattern of $NiWO_4$ samples can be indexed to standard monoclinic $NiWO_4$ pattern (JCPDS card No. 15-0755).[24] Due to the small size and low crystallinity of as-prepared $NiWO_4$ nanostructures, it results in broad and relatively low intensity of diffraction peaks. To acquire simply phase identifiable products, $NiWO_4$ materials obtained by hydrothermal process were annealed at 600 ^oC for 1 h in air, XRD patterns were recorded afterwards and corresponded accurately to its standard pattern. Furthermore, Raman spectra for $NiWO_4$ samples after annealing (Figure 2.6 c) showed an exact match for $NiWO_4$ in the previous report. The $CoWO_4$ sample formed after hydrothermal reaction matched the standard $CoWO_4$ structure (JCPDS card No. 15-0867) and its Raman spectrum (Figure 2.5 d) was also showed the same peaks as the one in the literature. [13,20] These results proved the formation of larger crystals of $CoWO_4$ compared to $NiWO_4$ materials after the hydrothermal process.

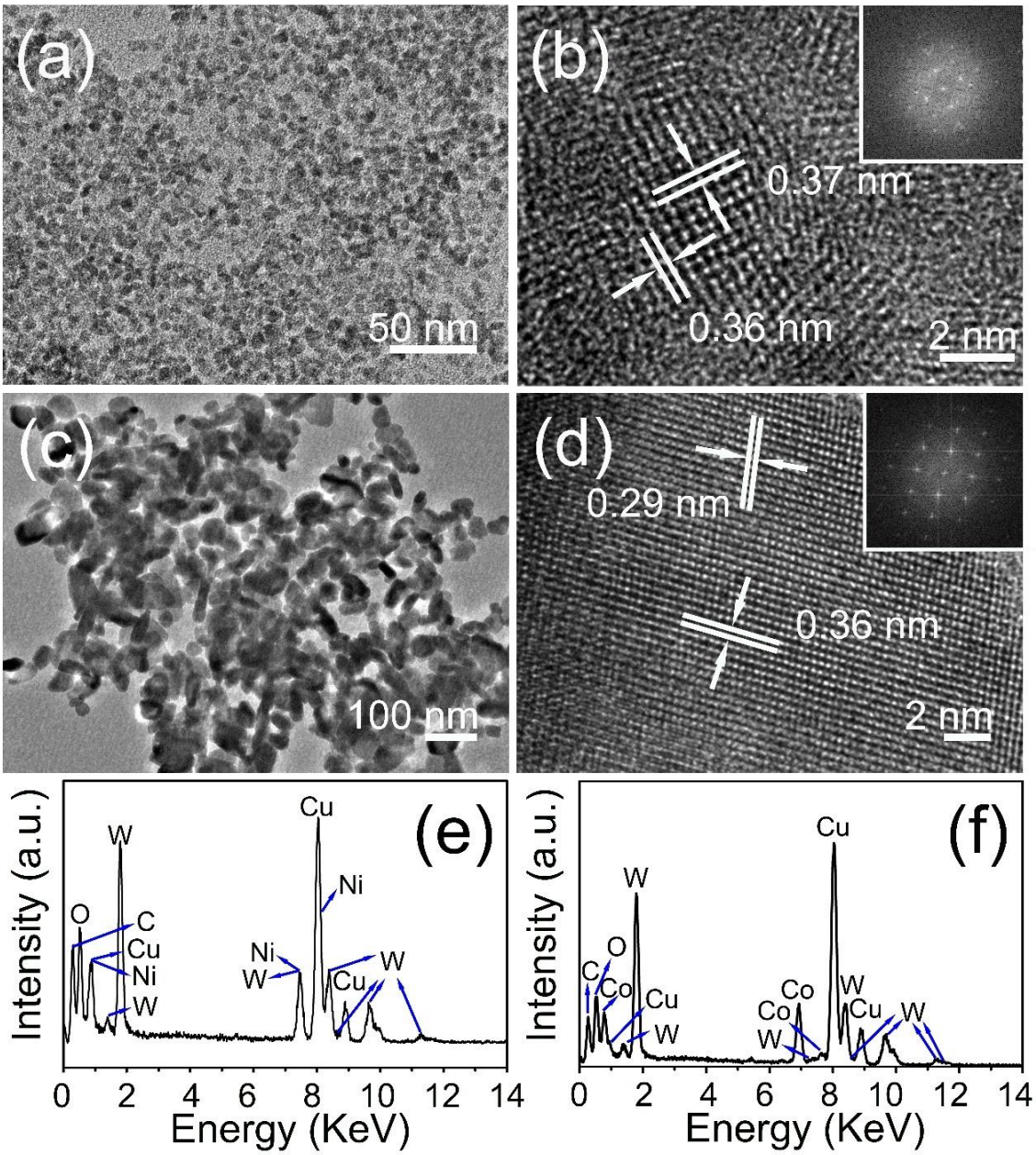

Figure 2. 4 (a, c) TEM nanostructured $NiWO_4$ and $CoWO_4$, respectively, (b, d) HRTEM images of $NiWO_4$ and $CoWO_4$ nanostructures, respectively, inset showing the matching FFT diffraction pattern; (e, f) EDS spectra of $NiWO_4$ and $CoWO_4$ recorded from relevant areas in TEM images, respectively.

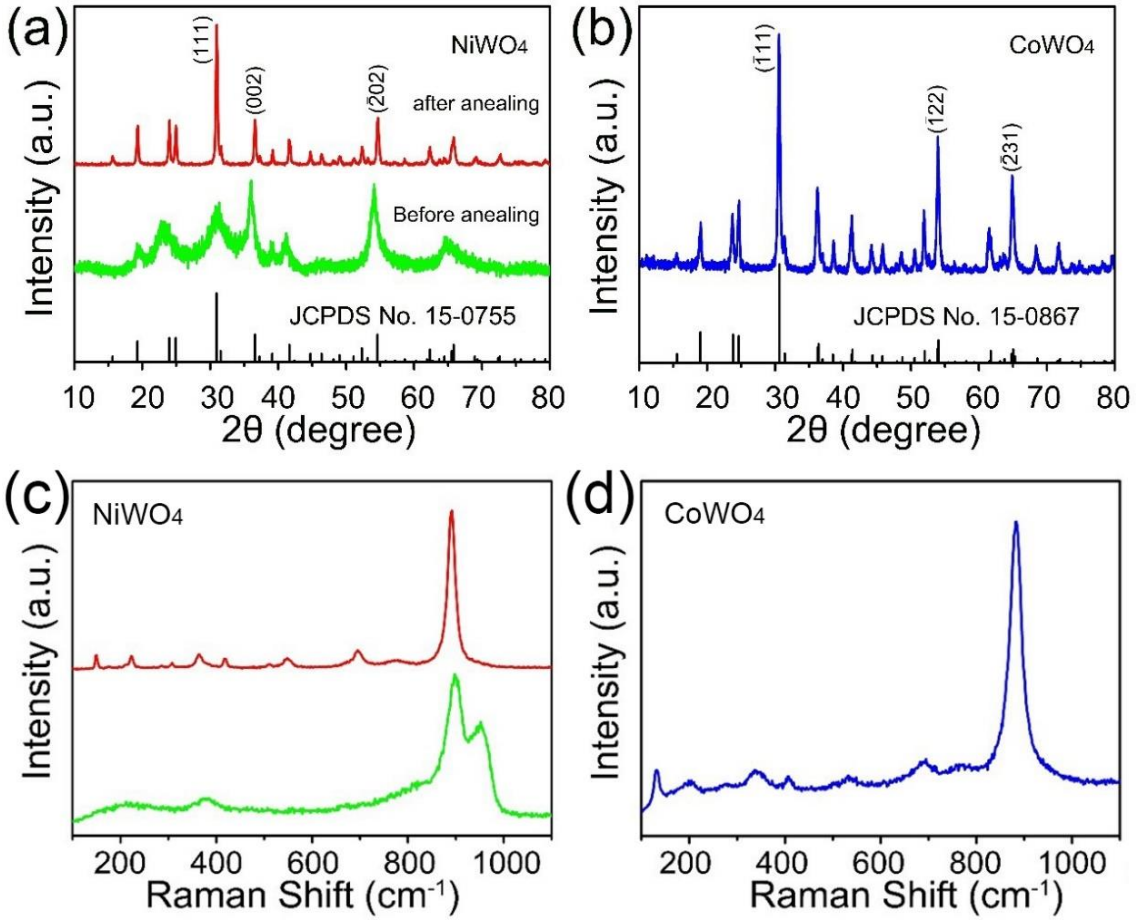

Figure 2. 5 XRD patterns of (a) $NiWO_4$ samples before (green) and after (red) annealing and its standard $NiWO_4$ pattern (JCPDS card No. 15-0755); (b) XRD patterns of $CoWO_4$ samples and its standard $CoWO_4$ pattern (JCPDS card No. 15-0867); (c, d) Raman spectra of (c) $NiWO_4$ nanostructures, before (green) and after (red) annealing; (d) $CoWO_4$ nanostructures, respectively.

To evaluate electrochemical energy storage performances of as-designed binder-free electrodes, cyclic voltammetry (CV) and galvanostatic charge-discharge (GCD) tests were carried out by utilizing $NiWO_4$/Ni foam, $CoWO_4$/Ni foam nanostructures and their powdery analogues as working electrodes in a three-electrode configuration (details in the experimental setup, Page 51). CV and GCD curves of $NiWO_4$/Ni foam and $CoWO_4$/Ni foam nanostructures were recorded after 3,000 cycles of CV scans at the scan rate of 50 mV s^{-1} for activation. As illustrated by CV curves at diverse scan rates in Figure 2.6a and b for Ni foam supported $NiWO_4$ and $CoWO_4$, respectively, obvious paired redox peaks can be clearly detected in each curve, which proved the Faradaic capacitive processes,

i.e. reversible redox reactions among different valence states of the Ni and the Co ions in alkaline electrolyte, respectively. As illustrated by the Pourbaix diagram shown in Ref.[20], W species do not participate in any redox reactions for electrochemical energy storage in alkaline aqueous electrolytes and its role in monoclinic $NiWO_4$ and $CoWO_4$ is to improve the electrical conductivity of the electrode materials. The shapes of the CV curves at diverse scan rates showed no obvious difference; the anodic and cathodic peaks with respect to oxidation and reduction processes shift to opposite directions, due to the need for more rapid ion and electron transfer within the interface of active species and electrolytes at higher scan rates. The above phenomena suggested the remarkable reversibility of the as-designed electrodes. The comparison of the GCD curves in a potential range between 0 and 0.45 V *vs.* Ag/AgCl for Ni foam supported $NiWO_4$ and $CoWO_4$ electrodes, $NiWO_4$ and $CoWO_4$ powders pasted electrodes at the same current density of 1 A g^{-1} are presented in Figure 2.6c. It's widely accepted that GCD test is a reliable method for evaluating gravimetric capacitance of supercapacitor by the following equation

$$C = \frac{It}{m\Delta V} \quad (2.1)$$

where I (A) is the current applied for the constant CD test, t (s) is the discharge time, m (g) is the mass of active materials on the electrodes (excluding the mass of binders and conductive agents), and ΔV (V) is the potential range during the discharge period, the specific capacitance of $NiWO_4$ nanoparticles/Ni foam and $CoWO_4$ nanoshuttles/Ni foam are higher as a result of the longer discharging time compared with the traditional electrodes. The gravimetric capacitance values are 797.8, 738.7, 658.9, 556.7, 486.7 and 443.6 F g^{-1} for Ni foam supported $NiWO_4$ electrodes and 764.4, 697.8, 611.1, 528.9, 430 and 386.7 F g^{-1} for $CoWO_4$/Ni foam electrodes at current densities of 1, 2, 5, 10, 15, 20 A g^{-1}, respectively. The rate performance is imperative for high-power applications which manifests the retention of specific capacitance with an increase of the current density of

charge/discharge. Ni foam supported nanostructures exhibit much better rate ability in comparison with their traditional electrodes counterparts, as shown in Figure 2.6d, which can be attributed to the advantages that Ni foam supported electrodes contain more active species participating in fast redox reactions and more channels for the electrolyte. The specific capacitances were 55.6% and 50.6% retention for Ni foam supported $NiWO_4$ nanoparticles and $CoWO_4$ nanoshuttles compared to their initial values, respectively, with 20 times increase of current densities. These drops from rate performance may be caused by the accessorial voltage drop and the issue that more active materials are not participated in fast reversible redox reactions with the increase of current densities.

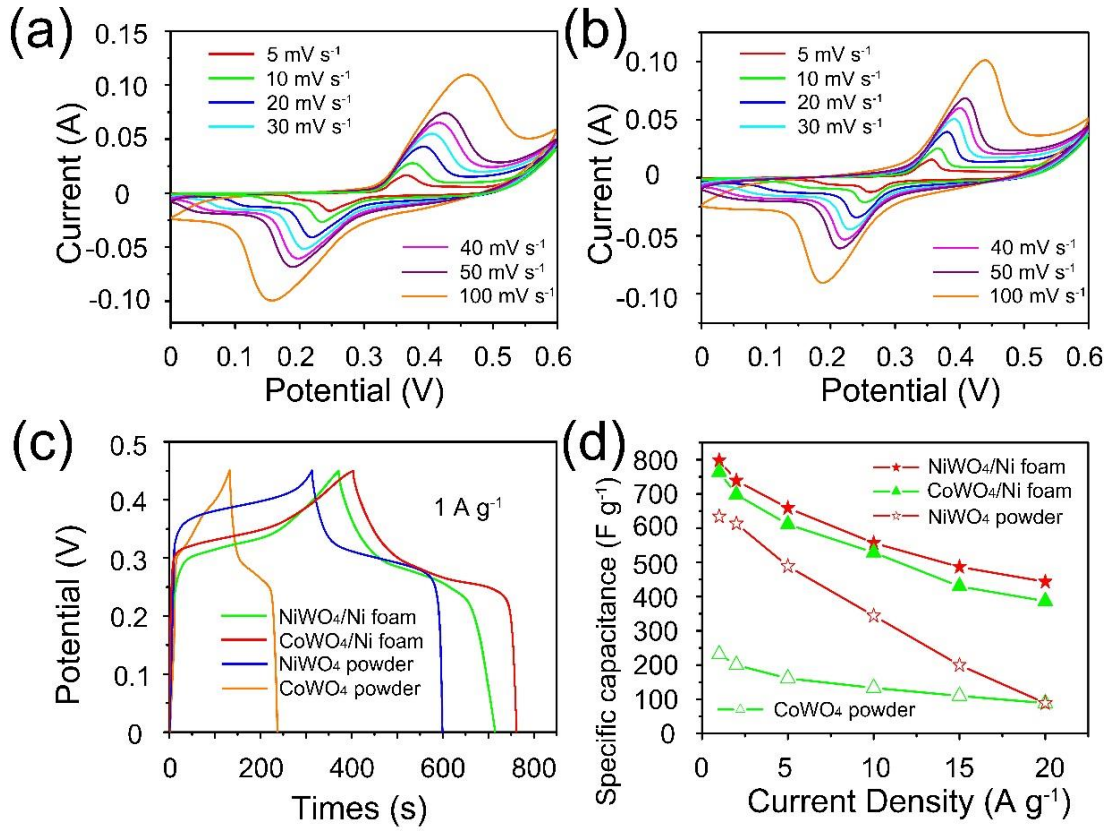

Figure 2. 6 (a, b) Cyclic voltammetry (CV) curves of Ni foam supported $NiWO_4$ and $CoWO_4$ electrodes at different scan rates from 5-100 mV s^{-1}, respectively. (c) The comparison of galvanostatic charge-discharge (GCD) curves of $NiWO_4$/Ni foam, $CoWO_4$/Ni foam, $NiWO_4$ and $CoWO_4$ powders at a current density of 1 A g^{-1}, respectively. (d) The comparison of rate performance of the electrodes made from Ni foam supported $NiWO_4$ and $CoWO_4$, $NiWO_4$ powders and $CoWO_4$ powders.

Electrochemical impedance spectroscopy (EIS) was tested to explore the resistance and ion-transfer capability of the as-designed electrodes. Figure 2.7a shows the Nyquist plots of $NiWO_4$ and $CoWO_4$ nanostructures/Ni foam electrodes, respectively. The inset of Figure 2.7a, showing the high frequency range of EIS spectra, exhibited information about the equivalent series resistance (ESR), consisting of inherent resistances of the active materials, bulk resistance of electrolyte and contact resistance of the interface between electrolyte and electrodes, which are 0.575 and 0.515 Ω for $NiWO_4$/Ni foam and $CoWO_4$/Ni foam, respectively. Additionally, free and multiple interspaces within these self-assembled nanostructures can served as “storage channels” that can shorten the diffusion pathway of ions from the external electrolyte to the interior surfaces, thus reducing ion transport resistance. Moreover, the semi-circle with an unclear arc can also be noticed from the high-frequency region, which reflected the ability of diffusion of electrons by charge-transfer resistance (R_{ct}). The calculated R_{ct} are 4.037 Ω and 3.479 Ω of Ni foam supported $NiWO_4$ and $CoWO_4$ electrodes, respectively. These results suggested that the excellent electrical conductivity and ion-diffusion properties of as-designed electrodes, which outperformed their binary metal oxides (NiO, [25] Co_3O_4, [26] WO_3[27]) nanostructured counterparts in the reported work. The long-term cycling performance is another crucial test to measure performance decay under working conditions of supercapacitor electrodes for practical applications. In this work, the cycling stability of the electrode materials was performed by cyclic CV test at a scan rate of 50 mV s^{-1} for 6000 cycles. It is noteworthy that the individual specific capacitance of the two electrodes increased dramatically in the first period. This long activation period can be allied to the huge number of individual small sizes of nanoparticles that formed rough morphologies, which will cost a certain time to stimulate the majority of active materials. During the activation period, the electrode will be reacted through the surface absorption and somewhat diffusion-controlled intercalation and de-intercalation processes of ions from the electrolyte, thus inducing more

active sites to take part in energy storage redox reactions. Moreover, for both electrodes, there were further increases after several cycles' decline, which can be explained by two reasons: (1) a continuous improvement in the surface wetting of the electrode by the electrolyte during long-term cycling; [28] (2) a small quantity of the active nanostructures dissolved and detached from the current collector during the stability test and the inner nanostructures began to be activated. The specific capacitance after the 6000 cycles were 2.06 and 2.81 times of their first cycle for $NiWO_4$/Ni foam and $CoWO_4$/Ni foam electrodes, respectively. Impressively, the capacitance of $CoWO_4$/Ni foam nanostructures showed a further increased trend even after 6000 cycles. The cyclic performance of pristine Ni foam substrates is shown in Figure 2.9, the result presented almost no influence on the evaluation of Ni foam supported nanostructures.

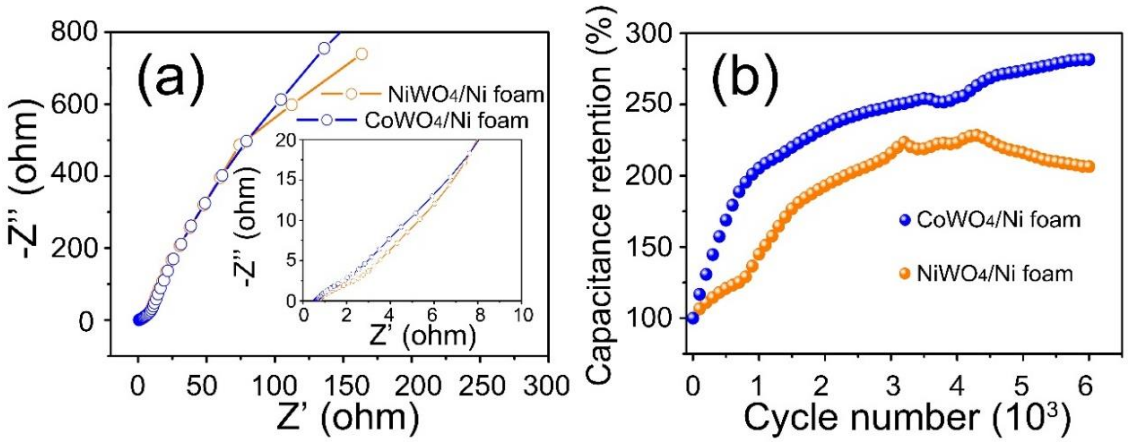

Figure 2. 7 (a) EIS spectra of self-assembled Ni foam supported $NiWO_4$ and $CoWO_4$ electrodes, inset showing high frequency region of the spectra; (b) Cycling performances of Ni foam supported $NiWO_4$ and $CoWO_4$ electrodes of 6000 cycles from CV tests at 50 mV s^{-1}.

The $NiWO_4$/Ni foam and $CoWO_4$/Ni foam electrodes after stability test maintained their original self-assembled structures and an even rougher morphology, as shown by SEM images in Figure 2.8. This result provides evidence of stable structures even after long-term cycles and improved electrochemical energy storage properties. The electrochemical energy storage performance of Ni foam

supported $NiWO_4$ and $CoWO_4$ nanostructures in this work is superior compared to other reported tungstate-based electrodes in the literature, as listed in Table 2.1.

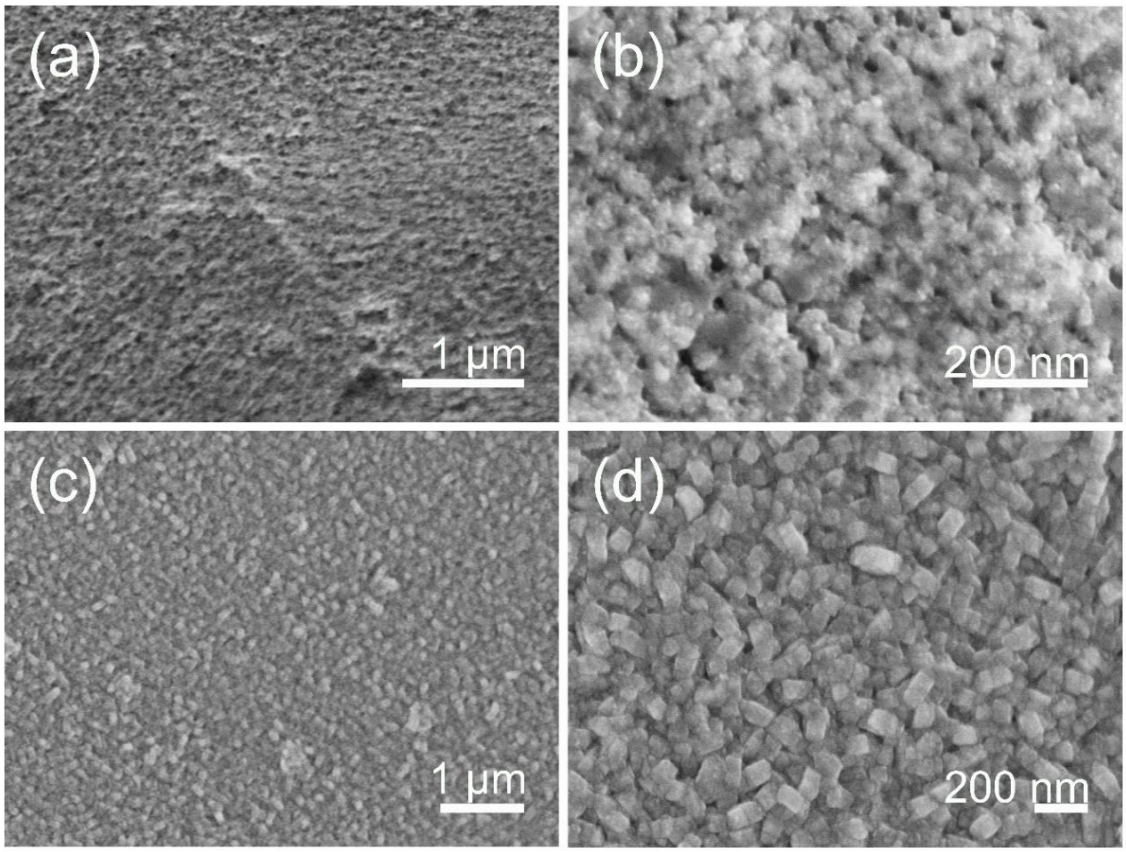

Figure 2. 8 (a) Low- and (b) high-magnification SEM image of $NiWO_4$/Ni foam nanostructures after stability test; (c) Low- and (d) high-magnification SEM image of $CoWO_4$/Ni foam nanostructures after stability test.

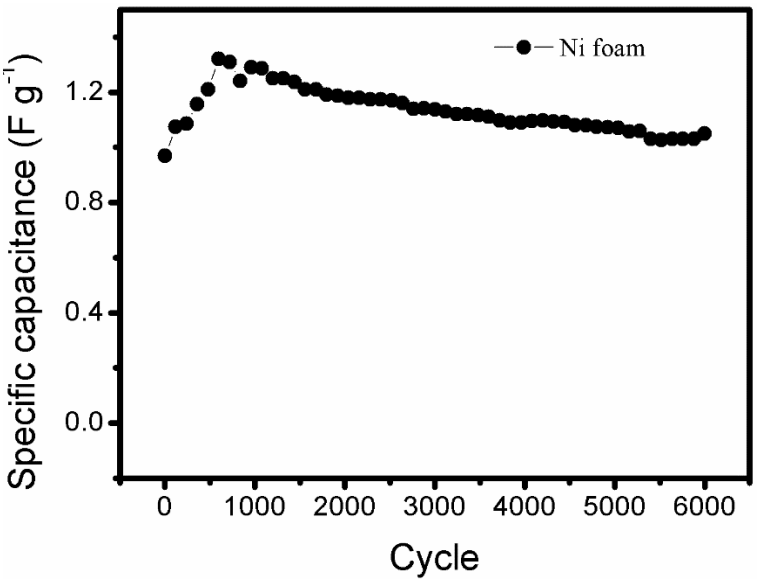

Figure 2. 9 Cycling performance of Ni foams.

Table 2. 1 Comparison of electrochemical energy storage performances

Nanostructures	Specific capacitance	Cycling Stability (Compared with initial value)	Reference
$NiWO_4$/Ni foam nanostructures	797.8 F g^{-1} at 1 A g^{-1}	2.06 times after 6000 cycles	Our work
$CoWO_4$/Ni foam nanostructures	764.4 F g^{-1} at 1 A g^{-1}	2.81 times after 6000 cycles	Our work
$NiWO_4$ amorphous nanostructure	586.2 F g^{-1} at 0.5 A g^{-1}	0.9 times after 1000 cycles	[13]
$CoWO_4$/rGO nanocomposites	159.9 F g^{-1} at 5 mV s^{-1}	0.947 times after 1000 cycles	[20]
$NiWO_4$ DNA Scaffold	173 F g^{-1} at 5 mV s^{-1}	0.9 times after 1000 cycles	[29]
WO_3/carbon aerogel composites	700 F g^{-1} at 25 mV s^{-1}	0.95 times after 4000 cycles	[30]
ZrO_2-SiO_2/ultrasmall WO_3 nanoparticles	313 F g^{-1} at 1 A g^{-1}	0.9 times after 2500 cycles	[31]

2.4 Conclusion

$NiWO_4$ and $CoWO_4$ are seldom studied as electrode materials for electrochemical energy storage application. In this chapter, a manageable one-step hydrothermal approach was developed to synthesize Ni foam supported $NiWO_4$ and $CoWO_4$ nanostructures with excellent electrochemical energy storage properties during use as supercapacitor electrodes. This is the first reported work by using a binder-free electrode making strategy to synthesize $NiWO_4$ and $CoWO_4$ nanostructures on current collectors. The as-designed electrodes showed remarkable electrochemical performance, such as a high gravimetric capacitance of 797.8 F g^{-1} and 764.4 F g^{-1} at the current density of 1 A g^{-1} after activation of 3000 cycles; both of these electrodes revealed superior cycling stability, the 6000^{th} cycle in the cyclic CV test at the scan rate of 50 mV s^{-1} were 2.06 and 2.81 times of their initial cycles for $NiWO_4$/Ni foam and $CoWO_4$/Ni foam electrodes, respectively. These prominent electrochemical performances can be ascribed to the excellent electrical conductivity and high structural stability of the binder-free

nanostructured electrodes, improved transport pathways of electron and ion and enlarged contacting area with the electrolyte. However, in this work, the use of tungsten atoms was required to improve the electron conductivity of binary metal materials (tungstate) compared to NiO or CoO/Co_3O_4. Other efficient materials of nickel or cobalt based electrodes combining with the binder-free strategies are needed. Moreover, although a lot of literature including this chapter claimed Ni or Co-based materials in alkaline aqueous electrolyte as pseudocapacitor electrodes, the blurred electrochemical energy storage mechanism should be clarified.

2.5 References

[1] P. Simon, Y. Gogotsi, *Nat. Mater.* **2008**, *7*, 845.

[2] W. W. Liu, C. X. Lu, X. L. Wang, K. Liang, B. K. Tay, *J. Mater. Chem. A* **2015**, *3*, 624.

[3] J. H. Kim, K. Zhu, Y. F. Yan, C. L. Perkins, A. J. Frank, *Nano Lett.* **2010**, *10*, 4099.

[4] Q. Yang, Z. Y. Lu, T. Li, X. M. Sun, J. F. Liu, *Nano Energy* **2014**, *7*, 170.

[5] A. Ferris, S. Garbarino, D. Guay, D. Pech, *Adv. Mater.* **2015**, *27*, 6625.

[6] D. Z. Kong, J. S. Luo, Y. L. Wang, W. N. Ren, T. Yu, Y. S. Luo, Y. P. Yang, C. W. Cheng, *Adv. Funct. Mater.* **2014**, *24*, 3815.

[7] S. Cong, Y. Y. Tian, Q. W. Li, Z. G. Zhao, F. X. Geng, *Adv. Mater.* **2014**, *26*, 4260.

[8] C. H. An, Y. J. Wang, Y. N. Huang, Y. N. Xu, L. F. Jiao, H. T. Yuan, *Nano Energy* **2014**, *10*, 125.

[9] G. Q. Zhang, X. W. Lou, *Adv. Mater.* **2013**, *25*, 976.

[10] L. Q. Mai, F. Yang, Y. L. Zhao, X. Xu, L. Xu, Y. Z. Luo, *Nat. Commun.* **2011**, *2*, 381.

[11] S. J. Peng, L. L. Li, H. B. Wu, S. Madhavi, X. W. Lou, *Adv. Energy Mater*.

2014, *5*, 1401172.

[12] L. Zhou, D. Y. Zhao, X. W. Lou, *Adv. Mater.* **2012**, *24*, 745.

[13] L. Y. Niu, Z. P. Li, Y. Xu, J. F. Sun, W. Hong, X. H. Liu, J. Q. Wang, S. R. Yang, *ACS Appl. Mater. Interfaces* **2013**, *5*, 8044.

[14] R. Bharati, R. A. Singh, *J. Mater. Sci.* **1983**, *18*, 1540.

[15] B. Moreno, E. Chinarro, M. T. Colomer, J. R. Jurado, *J. Phys. Chem. C* **2010**, *114*, 4251.

[16] P. K. Pandey, N. S. Bhave, R. B. Kharat, *Mater. Res. Bull.* **2006**, *41*, 1160.

[17] J. Yan, T. Wang, G. Wu, W. Dai, N. Guan, L. Li, J. Gong, *Adv. Mater.* **2015**, *27*, 1580.

[18] U. M. García-Pérez, A. Martínez-de la Cruz, J. Peral, *Electrochim. Acta* **2012**, *81*, 227.

[19] Y. F. Bi, H. Nie, D. D. Li, S. Q. Zeng, Q. H. Yang, M. F. Li, *Chem. Commun.*, **2010**, *46*, 7430.

[20] X. W. Xu, J. F. Shen, N. Li, M. X. Ye, *Electrochim. Acta* **2014**, *23*, 150.

[21] Y. J. Cao, W. Y. Li, K. B. Xu, Y. X. Zhang, T. Ji, R. J. Zou, J. M. Yang, Z. Y. Qin, J. Q. Hu, *J. Mater. Chem. A* **2014**, *2*, 20723.

[22] W. Y. Li, G. Li, J. Q. Sun, R. J. Zou, K. B. Xu, Y. G. Sun, Z. G. Chen, J. M. Yang, J. Q. Hu, *Nanoscale* **2013**, *5*, 2904.

[23] V. H. Nguyen, J. J. Shim, *J. Power Sources* **2015**, *110*, 2730.

[24] M. N. Mancheva, R. S. Iordanova, D. G. Klissurski, G. T. Tyuliev, B. N. Kunev, *J. Phys. Chem. C* **2007**, *111*, 1101.

[25] L. Wang, H. Tian, D. L. Wang, X. J. Qin, G. J. Shao, *Electrochim. Acta* **2014**, *151*, 407.

[26] J. C. Deng, L. T. Kang, G. L. Bai, Y. Li, P. Y. Li, X. G. Liu, Y. Z. Yang, F. Gao, W. Liang, *Electrochim. Acta* **2014**, *132*, 127.

[27] L. Gao, X. F. Wang, Z. Xie, W. Song, L. Wang, X. Wu, F. Qu, D. Chen, G. Z. Shen, *J. Mater. Chem. A* **2013**, *1*, 7167.

[28] J. Yan, Z. J. Fan, W. Sun, G. Q. Ning, T. Wei, Q. Zhang, R. F. Zhang, L. J. Zhi, F. Wei, *Adv. Funct. Mater.* **2012**, *22*, 2632.

[29] U. Nithiyanantham, S.R. Ede, S. Anantharaj, S. Kundu, *Cryst. Growth Des.* **2015**, *15*, 673.

[30] Y. H. Wang, C. C. Wang, W. Y. Cheng, S. Y. Lu, *Carbon* **2014**, *69*, 287.

[31] G. H. Jeong, H. M. Lee, J. G. Kang, H. Lee, C. K. Kim, J. H. Lee, J. H. Kim, S. W. Kim, *ACS Appl. Mater. Interfaces* **2014**, *6*, 20171.

Chapter 3

Boosting Energy Storage and Conversion Performance by S, N-co-doped Graphene-Nickel Cobalt Sulfide Aerogels

3.1 Introduction

Graphene was widely invetigated and exhibited various applications after its first exfoliation in 2004.[1] Exhibiting two-dimensional single-layered carbon structures, graphene delivers distinct physical and chemical properties, such as ultra-high specific surface area (2630 $m^2 g^{-1}$),[2] remarkable chemical and thermal stability,[3] and excellent mechanical and electronic properties,[4, 5] *etc.* However, relatively strong van deer Waals forces between single carbon layers causes a trend of aggregation of graphene and forming graphite,[6] which results in an intense decline of specific surface area and kinetic ion-transport, influencing electrochemical properties of graphene materials when used in electrochemical energy storage[4] and coversion areas[7]. To avoid aggregation phenomenon and build up of rapid ion and electron pathways, novel graphene structures such as 3D carbon frameworks have been developed and synthesized. Methods for 3D graphene materials include template-assisted CVD approaches[8], self-assembled aerosol or hydrogel from hydrothermal synthesis[9, 10], electrospray ionization processes [11] and layered composites through filtration fabrication[6, 12]. However, graphene derived composites without further modification, sustain low electrochemical energy storage capacity and limited numbers of reactive species[3, 13, 14], which impede their application as highly active materials for electrochemical energy storage and catalysis. The background of graphene materials, especially aerogels made them potential applications for binder-free electrodes fabrication as a replacement of directly synthetic approach.

One efficient approach to improve the electrochemical properties of graphene composites, and broaden and boost their function is to use these materials as the conductive supports that form nanocomposites with metal-based semiconductors [15]. Nickel cobalt-based materials, such as oxides, sulfides and selenides, have been utilized as attractive candidates in the fields of energy storage and conversion applications, such as metal-ion batteries[16, 17], supercapacitors[6, 18, 19]

and eletrocatalysts[20-22], for example hydrogen or oxygen evolution[23-25]. A series of materials and nanostructures have been designed and produced from 1D to 3D hierarchical build-up.[26-29] For example, a series of $NiCo_2S_4$ ball-in-ball core-shell hollow spheres were fabricated by Lou *et al.* through solvothermal reaction combining with anion exchange approaches, and employed in supercapacitor electrode applications[28]. These materials when used in electrodes presented a gravimetric capacitance of 1036 F g^{-1} from charge-discharge test at a current density of 1 A g^{-1} and retained 87 % of the original capacitance after 2000 cycles. Moreover, Dai's group fabricated $Co_{1-x}S$/graphene hybrids for oxygen reduction electrocatalysts, which showed a relatively high ORR current density of 1.1 mA cm^{-2} at 0.7 V *vs.* RHE from LSV test.[30] Compared with transition metal oxides, sulfides and selenides generally deliver improved electron conductivity[31-33]. In consideration of the cost, performance stability or toxicity, transition metal sulfides are encouraging for electrochemical functions. The major obstacle to their wide use in aqueous electrolyte is the easy oxidization problem thus causing the decline of electron conductivity and charge mobility during long-term use in particular.[34] To figure out this problem, it is critical to design and synthesize Ni-Co-S materials with reformative electrochemical stability and capabilities by structural engineering.

Based on the above background, in this chapter, S, N co-doped graphene-based nickel cobalt sulfide aerogels (Ni-Co-S/SNGA) were designed and synthesized with the primary aspiration to optimize the electrochemical performances of Ni-Co-S, especially their long-term stability. Furthermore, this work will solve the concerns raised in Chapter 2 about the blurred energy storage mechanism by illustrating their reaction mechanism from kinetic analysis and their potentially extensive application. The Ni-Co-S/SNGA presented modified electrochemical performance as electrode materials for rechargeable alkaline batteries and electrocatalysts for ORR in aqueous alkaline electrolyte.

3.2 Experimental section

Graphite powders were acquired from Hopkin & Williams Company (U.K.). Ni foams were from the Suzhou JSD foam metal Co. Ltd. (China). The glassy fiber papers were received from Fisher Scientific (U.K.). Polyvinyl alcohol (PVA) was purchased from Tokyo Chemical Industry Co., Ltd. All the other chemicals were obtained from Sigma-Aldrich (U.K.) or VWR International (U.K.) and used as received without further purification.

3.2.1 Synthesis of four different ratios of nickel cobalt sulfide nanostructures

Four solutions with different molar ratios of $Ni(NO_3)_2•6H_2O$ and $Co(NO_3)_2•6H_2O$ (1 mmol of $Ni(NO_3)_2•6H_2O$ and 2 mmol of $Co(NO_3)_2•6H_2O$; 2 mmol of $Ni(NO_3)_2•6H_2O$ and 1 mmol of $Co(NO_3)_2•6H_2O$; 3 mmol of $Ni(NO_3)_2•6H_2O$; 3 mmol of $Co(NO_3)_2•6H_2O$) were prepared. The nickel and cobalt precursors were dissolved in 15 mL of DI water and 20 mL of ethanol with magnetic stirring for 1 hour. After that, 1 g of thiourea was dissolved in the above solutions sequentially with another 1 hour stirring. Finally, the pH of each solution was controlled as 8.0 by ammonium hydroxide solution (ACS reagent, 28 - 30% NH_3 basis). The solutions were transferred into four 50 mL-autoclaves separately and kept in the oven at 180 ^oC for 12 h. The powder samples were washed by water and ethanol in centrifugation and dried through lyophilization for further use.

3.2.2 Synthesis of graphene oxide (GO)

GO was synthesized from graphite powder by an improved Hummer s' method with minor modification.[24] At first, 3 g of graphite powder was mixed with 69 mL of 98 % H_2SO_4 in an 800 mL container with 145 r/min magnetic stirring for 1 h. After that, 9 g of $KMnO_4$ was added into the above suspension slowly and whole process lasted ~ 45 min. The container was then kept in an oil bath at 35 ^oC for

2 h without further stirring. The reaction temperature of the system was increased from 35 °C to 98 °C and 138 mL of DI water was added into the above solution slowly and kept at 98 °C for 15 min during this process. Additional 420 mL of water together with preheated 7.5 mL of H_2O_2 (30%) was dropped in to react with the excess potassium permanganate while the colour of the solution changed from dark brown to light yellow. Then, the solution was kept at room temperature with magnetic stirring for 24 h. Subsequently, the powder was filtered and washed by HCl solution (750 mL H_2O and 7.5 mL concentrated HCl to remove metal ions). The filter cake was re-dispersed in DI water and the aggregates were removed from the dispersion by 15 min of centrifugation at 3000 rpm. Finally, the dispersion was purified by dialysis for three days to remove any impurities.

3.2.3 Synthesis of S, N doped graphene-based nickel cobalt sulfide aerogel (Ni-Co-S/SNGA) and S, N co-doped graphene aerogel (SNGA).

In a typical synthesis, GO dispersion solution was diluted to ~ 2 mg/ml. Different ratios of nickel cobalt sulfide nanoparticles (2:1 ratio is 0.14 g from step 1) were added into four 35 ml of GO solution respectively with magnetic stirring for 1 h. Then, 0.5 g of thiourea was added to each solution with further magnetic stirring. Finally, the above solutions were transferred to four 50 ml autoclaves and kept in a preheated oven at 180 °C for 12 h. The as-synthesized hydrogels were placed into the beakers with 50 ml DI water (water changed every ~ 10 h) for three days to remove any impurities and freeze-dried at ~ -50°C. SNGA were prepared by the same process without adding Ni-Co-S nanoparticles initially.

3.2.4 Characterization

The morphology and micro/nanostructures of aerogels were recorded by scanning electron microscopy (SEM, Hitachi S-4800 and JSM-6700F equipped with an energy-dispersive X-ray spectrometer) and transmission electron microscopy (TEM, JEOL, JEM-2100). The phases and chemical compositions

were tested by D4 ENDEAVOR X-ray diffractometer (XRD; Cu-Ka radiation), X-ray photoelectron spectroscopy (XPS; Thermo scientific K-alpha photoelectron spectrometer), Raman spectroscopy (Renishaw Raman microscope spectrometer with the laser wavelength of 514.5 nm). *Ex-situ* XRD for different charge and discharge stages of the alkaline battery electrodes were performed on a STOE SEIFERT diffractometer (Mo source radiation). The mass of the materials used for electrodes and active materials for ORR test was weighed accurately by an analytical balance (Ohaus; δ = 0.01 mg).

3.2.5 Electrochemical measurements

Performance evaluation of alkaline battery electrodes. Electrochemical measurement of as-designed electrodes was performed on a Gamry (Gamry Interface 1000) or Autolab (PGSTAT302N) in a three-electrode configuration with 6 M KOH as the electrolyte. A platinum foam (~ 2 cm^2) and Ag/AgCl electrode were used as counter and reference electrodes, respectively. The active materials were pressed into Ni foams directly as the binder-free and conductive agent-free working electrodes. The mass of the active materials on nickel foam is ~ 2 mg (area of ~ 1 cm^2) for testing. The electrochemical impedance spectroscopy (EIS) tests were carried out at open circuit potential with a sinusoidal signal over a frequency range from 100 kHz to 0.01 Hz at an amplitude of 10 mV. The specific capacity was calculated by the equation as follows:

$$C = \frac{I \times \Delta t}{m} \quad (3.1)$$

Where I is the applied current for the GCD test (A); Δt is the discharge time (s); m is the mass of the active material (g). The values were recorded and calculated after 100 cycles of cyclic voltammetry (CV) at 50 mV s^{-1} for activation.

3.2.6 Fabrication and evaluation of hybrid battery devices

Electrolyte preparation: The solid-state electrolyte was prepared by mixing two parts of solution: 1. 6 g of PVA was dissolved into 40 mL of DI water at a temperature of 90 ^oC; 2. 20 mL of 6 M KOH water solution. Above two solutions

were transferred to the room temperature and mixed with magnetic stirring for further use.

Devices fabrication

Hybrid batteries were manufactured by pressing $CoNi_2S_4$/SNGA into a piece of Ni foam (~ 1 cm^2) as the cathode and the SNGA into another piece of Ni foam (~ 1 cm^2) as the anode. The mass ratio of the positive to negative electrodes was calculated according to the charge balance equation ($Q_+ = Q_-$). Before device fabrication, the electrodes were pre-activated by CV tests at a scan rate of 50 mV s^{-1} in the 6 M KOH electrolyte. The fabricated devices were put in the fume hood to wait for extra water evaporation and gel formation. ~ 0.5 mL of prepared PVA/KOH solutions were added to each device.

To meet the requirement of $Q_+ = Q_-$, the mass ratio of active materials on two electrodes were controlled by the following equation:

$$\frac{m_+}{m_-} = \frac{C_-}{C_+} \quad (3.2)$$

Where C_+ and C_- (mAh g^{-1}) are the gravimetric capacity of $CoNi_2S_4$/SNGA and SNGA, respectively. The mass ratio was calculated as ~ 1:7 based on the measured capacities of the electrodes.

Device evaluation

The volumetric capacity of the device (C_{device}) was calculated by the equation (3.3):

$$C_{device,volume} = \frac{I \times \Delta t}{V} \quad (3.3)$$

Where $C_{device,volumn}$ (mAh cm^{-3}) is the volumetric capacity of the device, I (A) is the applied current for the galvanostatic charge-discharge (GCD) test, Δt (s) is the discharge time, V (cm^3) is the entire volume of the device.

The volumetric and gravimetric energy ($E_{volume}\ or\ E_{mass}$) and power density ($P_{volume}\ or\ P_{mass}$) based on the volume or mass of the devices (including all the materials and packaging) were calculated according to equations shown below:

$$\mathrm{E} = I \int_0^{t_{max}} U_{(t)} dt \quad (3.4)$$

$$P_{output,max} = \frac{U^2}{4R_s} \quad (3.5)$$

$$R_s = \frac{U_{drop}}{2I} \quad (3.6)$$

$$E_{volume}\ or\ E_{mass} = \frac{E}{V_{device}}\ or\ \frac{E}{m_{device}} \quad (3.7)$$

$$P_{volume}\ or\ P_{mass} = \frac{P_{output,max}}{V_{device}}\ or\ \frac{P_{output,max}}{m_{device}} \quad (3.8)$$

In the above equations, E is the total energy released from the system, t_{max} is the whole discharge time, U is the voltage range of GCD test for the device (excluding the voltage drop), R_s is the internal resistance within the device, U_{drop} is the voltage drop from the discharge curve and I is the applied current from galvanostatic tests. P_{output}, I_{output} and R_e are the power, output current and resistant within the external circuit, respectively.

The equation (3.5) was derived from:

$$I_{output} = \frac{U}{R_e+R_s} \quad (3.9)$$

$$P_{output} = {I_{output}}^2 R_e = \frac{U^2}{R_e+R_s} \times \frac{R_e}{R_e+R_s} = \frac{U^2}{R_e+\frac{{R_s}^2}{R_e}+2R_s} = \frac{U^2}{\frac{(R_e-R_s)^2}{R_e}+4R_s} \quad (3.10)$$

When $R_\mathrm{e} = R_s$, the P_{output} exhibits the maximum value.

In addition, 1 cm^2 device includes: nickel foam, active materials, separator and gel electrolyte, the total mass: 0.24222 g; the total volume: 0.08 cm^3; the thickness was evaluated by the Vernier caliper (resolution: 0.02 mm).

3.2.7 Oxygen reduction reaction evaluation

During the ORR performance test, the electrodes were prepared by mixing 4 mg of catalysts, 964 µL of DI water and 36 µL of nafion solution (5 % w/w). The mixture was then sonicated for ~ 40 min in the ice bath to obtain a homogeneous ink. For preparing rotating disk electrodes (RDE), 5 µL of the slurry was then deposited onto the glassy carbon disk (diameter of 3 mm) electrodes and dried for ~ 30 min under room temperature in air. 14 µL of the same ink was applied to prepare the rotating ring-disk electrode (RRDE, diameter of 5 mm) test. All electrochemical tests were performed on a potentiostat (Metrohm Autolab

PGSTAT204) in a standard three-electrode configuration. The Ag/AgCl electrode and a platinum wire were used as the reference and the counter electrode, respectively. CV was performed in oxygen-saturated 0.10 M KOH solution at a scan rate of 100 mV s^{-1}. LSV curves were obtained by rotating the electrode at 400, 800, 1200, 1600, 2000 and 2400 rpm respectively at a scan rate of 10 mV s^{-1} in oxygen-saturated 0.10 M KOH solution. The final current density from oxygen reduction reaction is obtained by subtracting the current density in nitrogen-saturated electrolyte to eliminate the influence from hydrogen evolution.

The analysis of transferred electron number per O_2 in the ORR procedure was based on:

$$n = \frac{4I_d}{I_d + \frac{I_r}{N}} \quad (3.11)$$

Where I_d is the disk current, I_r is the ring current and N is the current collection efficiency of the Pt ring. In this system, N was tested to be 0.25 from the reduction of $K_3Fe[CN]_6$. The current-time chronoamperometric responses was recorded after the first 500 s activation period for stabilizing the electrodes at -0.45 V *vs.* Ag/AgCl with a rotation rate of 800 rpm in O_2-saturated 0.1 M KOH.

3.3 Results and discussion

3.3.1 Structure and composition

The synthetic process to fabricate Ni-Co-S/SNGA is presented in Figure 1a. Four types of Ni-Co-S nanostructures were obtained by one-step hydrothermal method with controlled ratios of precursors. A series of hybrids were obtained from mixtures of specific amounts of GO solutions, thiourea and Ni-Co-S nanostructures by hydrothermal reaction followed with a three-day lyophilized process. Nitrogen-doped graphene was incorporated to provide optimized electron conductivity and ion electroactivity of the structure, which is due to lone

electron pairs from the nitrogen species constituting delocalized conjugated systems with sp^2-hybridized carbon frameworks.[35] Moreover, sulfur-doping strategy was demonstrated to increase space utilization of carbon materials and thus improve electrochemical properties.[36] In addition, sulfur atoms are covalently incorporated into graphene framework and boosted the bridging of metal sulfides to graphene materials, which allowed the formation of robust composites.[37] In the synthesis, thiourea could act as a N and S source but also serve as a reductant for graphene oxides in the solvothermal process, which further promotes the electron conductivity of the carbon skeleton. A photograph of an aerogel is presented in Figure 3.1b, the macroscopic foam provided the possibility for binder and conductive-agents free electrode candidates. The water contact angle measurements in Figure 3.1c of a water droplet on hybrids shows a 0° contact angle, demonstrating that it is fully wetted and superhydrophilic. The character is highly effective and beneficial to electrochemical energy storage and conversion properties in aqueous electrolytes.

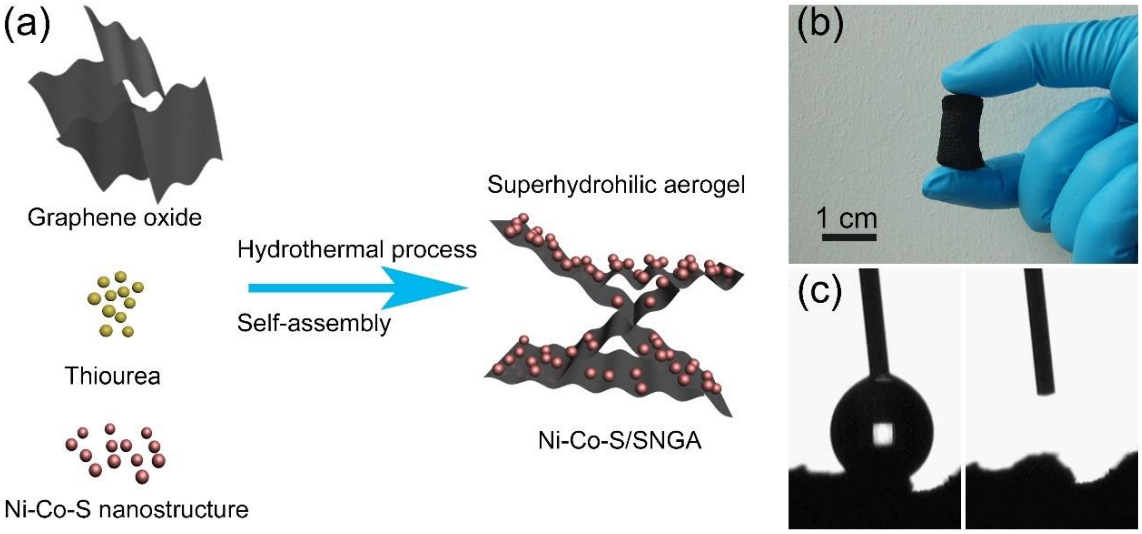

Figure 3. 1 (a) Schematic illustration of the synthetic procedure for Ni-Co-S/SNGA electrode materials; (b) Digital camera picture of a representative aerogel; (c) contact angle tests before (left) and after (right) water dropping.

The basic morphologies of these series of materials were explored by scanning electron microscopy (SEM). It is noted Ni-Co-S nanostructures were dispersed on the surface of porous graphene supports from low-magnification SEM images in Figure 3.2. Multiple channels from all Ni-Co-S/SNGA are observed and can be utilized for ion transfer. From high-magnification images in Figure 3.3, the size of Ni-Co-S nanoparticles could be detected. The nanoparticles have the size of several tens to hundreds of nanometers with round or a nanorod shape forming nanoclusters. The small metal sulfide particle sizes together with large contacting areas with the electrolyte is suggested to promote the rate of energy storage or catalytic processes.

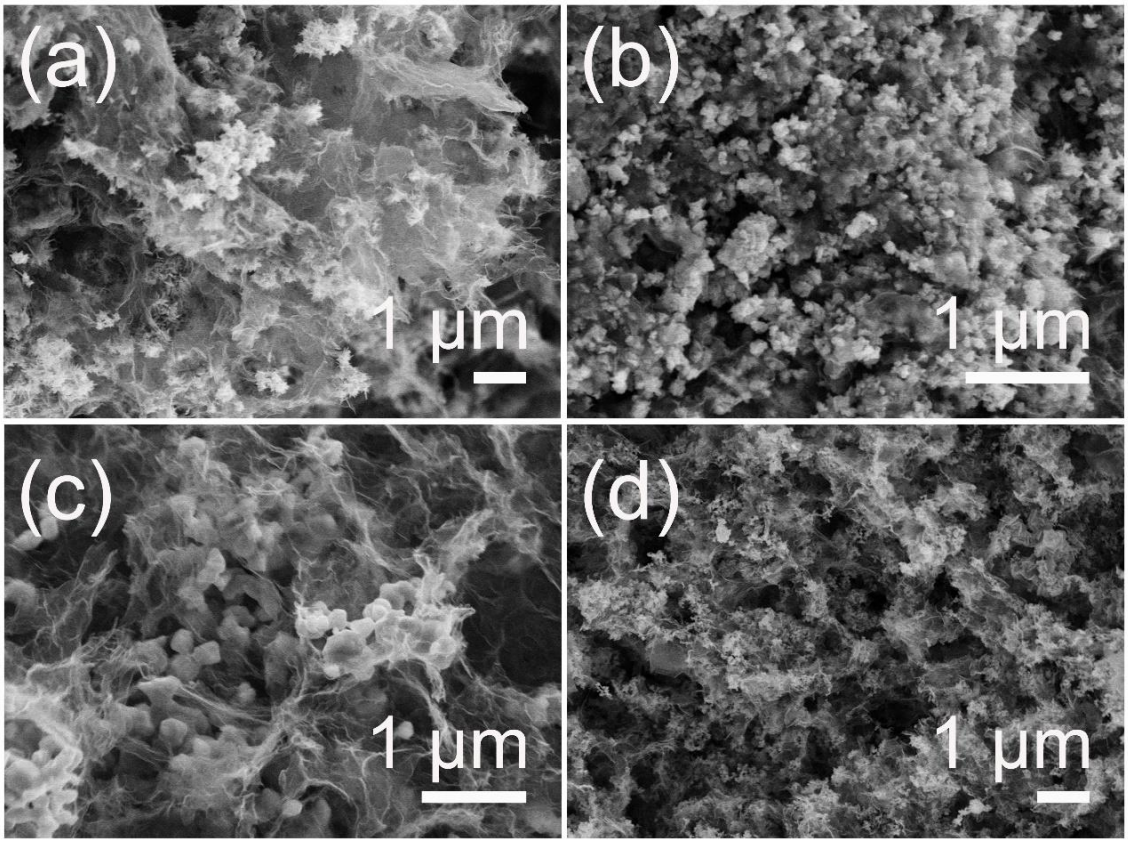

Figure 3. 2 Low-magnification SEM images of (a) $CoNi_2S_4$/SNGA, (b) $NiCo_2S_4$/SNGA, (c) Ni-S/SNGA and (d) Co-S/SNGA, respectively.

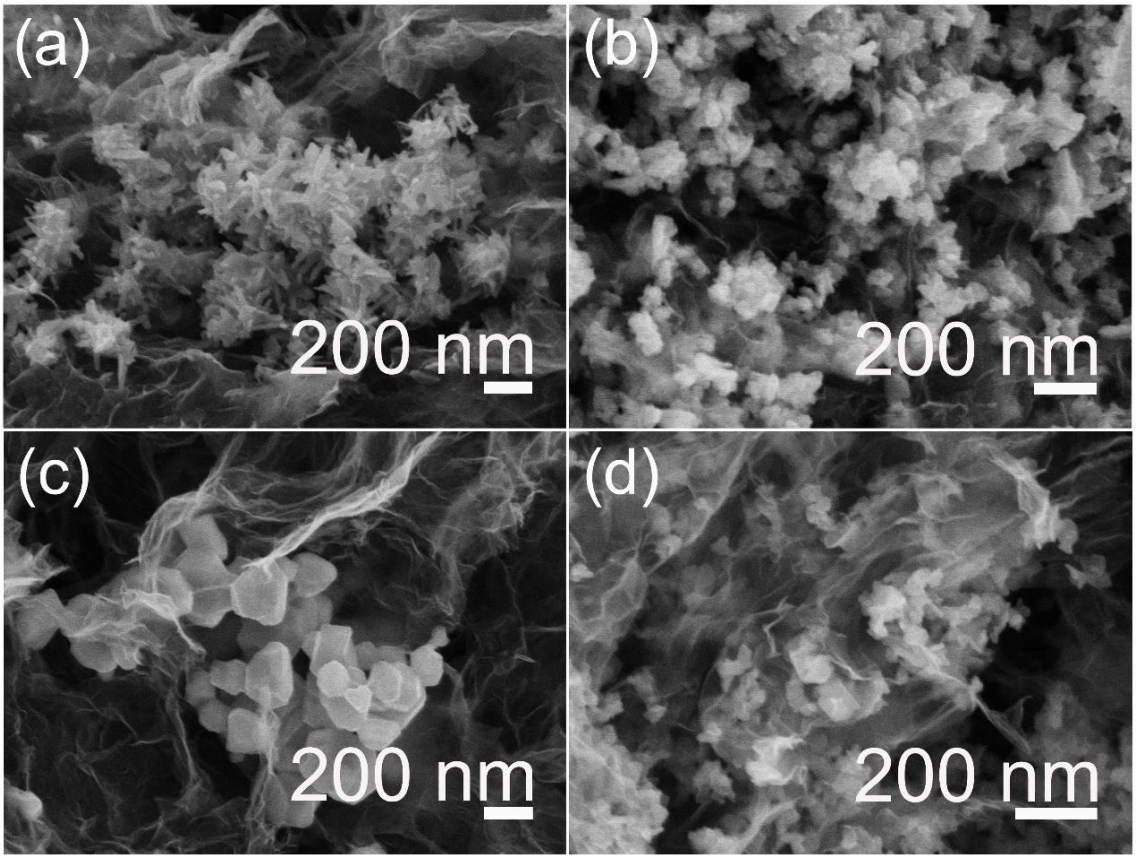

Figure 3. 3 High-magnification SEM images of (a) $CoNi_2S_4$/SNGA, (b) $NiCo_2S_4$/SNGA, (c) Ni-S/SNGA and (d) Co-S/SNGA, respectively.

The crystallographic phases of four kinds of Ni-Co-S /SNGA were investigated by X-ray diffraction (XRD). The obvious peak at 2θ = 10.8° from the diffraction pattern in Figure 3.4 can be indexed to the 002 reflections of GO and disappeared as for the rGO.[38] The $NiCo_2S_4$ nanoparticles in $NiCo_2S_4$/SNGA is the pure phase and corresponds to Fd-3m crystal structures of spinel $NiCo_2S_4$ (JCPDS no. 20-0782). By reasonably controlling precursor ratios of Ni-Co-S, the mixed phases of Ni-S and Co-S samples could be synthesized, which can be assigned to the Ni_3S_4 (JCPDS no. 47-1739), NiS (JCPDS no. 12-0041) shown in Figure 3.4c and mixed Co_3S_4 (JCPDS no. 47-1738), $Co_{1-x}S$ (JCPDS no. 42-0826) in Figure 3.4d, respectively.

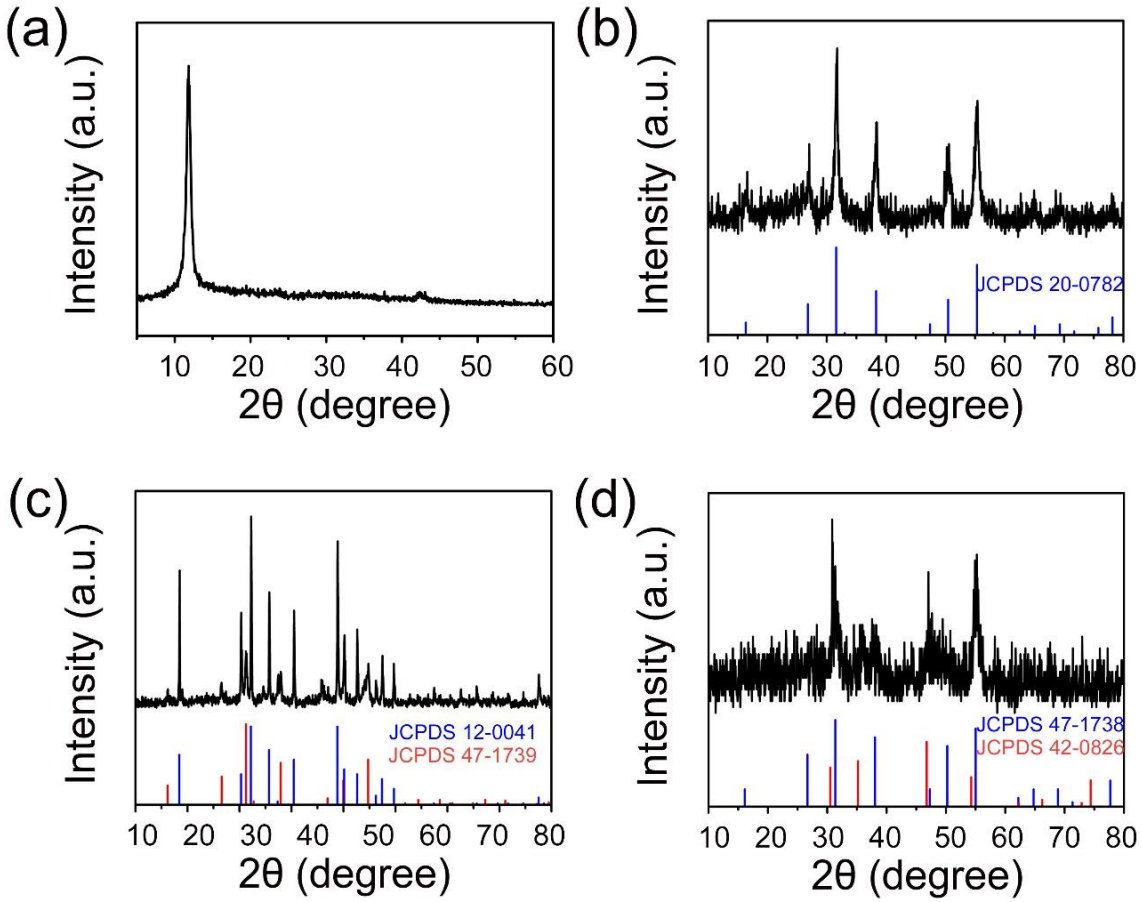

Figure 3. 4 Phase examination from XRD patterns of (a) GO; (b-d) Ni-Co-S/SNGA nanostructures: (b) $NiCo_2S_4$/SNGA and its corresponded standard pattern (JCPDS 20-0782), (c) Ni-S/SNGA and its corresponded standard patterns (JCPDS 12-0041 and 47-1739) and (d) Co-S/SNGA and its corresponded standard patterns (JCPDS 47-1738 and 42-0826), respectively.

Take $CoNi_2S_4$/SNGA as an example, its XRD pattern can be indexed to reference $CoNi_2S_4$ Fd-3m structures (JCPDS no. 24-0334) in Figure 3.5. The weak peaks shifted to ~ 24^o can be ascribed to the (002) lattice plane of SNGA after hydrothermal reduction process. The TEM image in Figure 3.5b presents that as-fabricated $CoNi_2S_4$ materials sustained a consistent urchin-like structure with nanorods self-assembled radially and grown from the nucleation centre, forming $CoNi_2S_4$ nanoclusters capped by the graphene aerogel (GA). The individual nanorod has a diameter of ~ 15 nm (Figure 3.5c). HRTEM image of $CoNi_2S_4$/SNGA in Figure 3d showed a d-spacing of 0.54 nm caculated from clear

lattice fringes, which can be attributed to the (111) plane of Fd-3m structures of $CoNi_2S_4$, in conformity to the phase information.

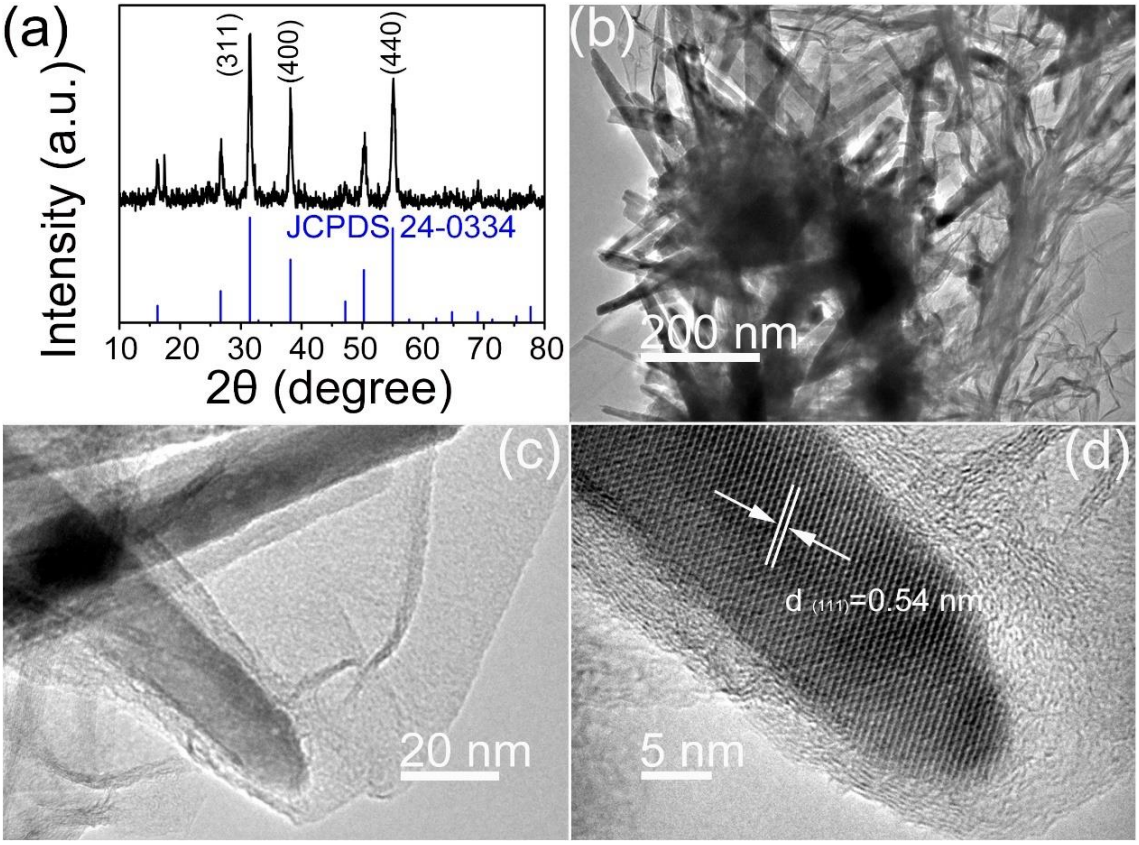

Figure 3. 5 (a) XRD patterns of $CoNi_2S_4$/SNGA and its corresponding standard pattern; (b-c) TEM images from low and high-magnification and (d) HRTEM of $CoNi_2S_4$/SNGA, repectively.

Raman spectroscopy in Figure 3.6a was conducted to illustrate the graphitization and structural information of the GO, $CoNi_2S_4$/GA, and $CoNi_2S_4$/SNGA materials, respectively. The distinct D and G peaks of GO and $CoNi_2S_4$/SNGA are at 1353.2 and 1591.3 cm^{-1}, respectively. The ratio of I(D)/I(G) of aerogels varied as different compositions of $CoNi_2S_4$ nanostructures and S, N co-doping into GO and revealed the degree of graphitization decreased as the increase of doping atoms although the GO aerogel reduced to rGO.[10] Among these three composites, $CoNi_2S_4$/SNGA occupied the highest I(D)/I(G) value, showing it possesses the

highest reduction degree of GO and defects-rich features were appeared than its counterparts[35].

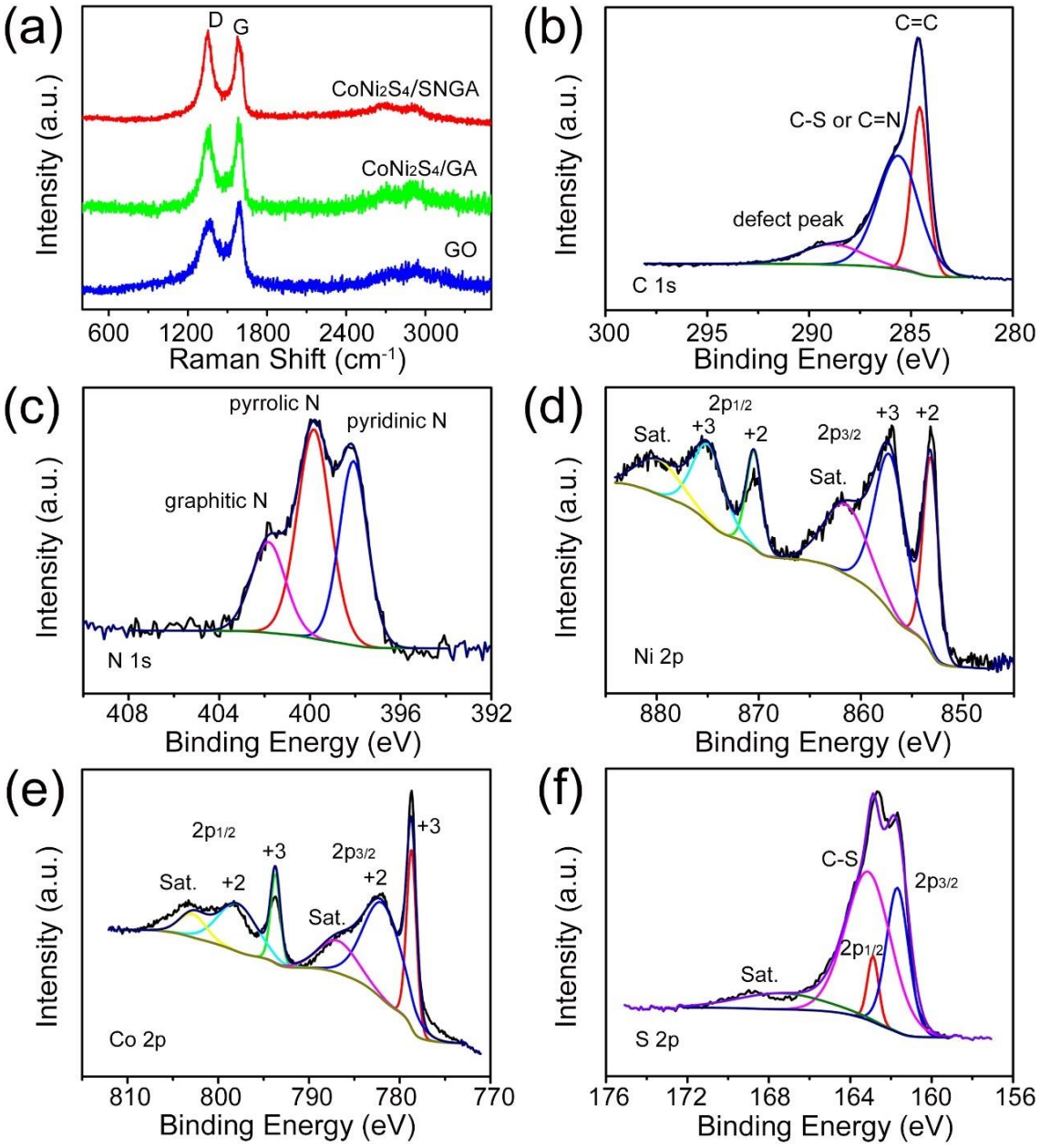

Figure 3. 6 (a) Raman spectra of GO, $CoNi_2S_4$/GA and $CoNi_2S_4$/SNGA, respectively; XPS spectra of (b) C 1s, (c) N 1s, (d) Ni 2p, (e) Co 2p and (f) S 2p from $CoNi_2S_4$/SNGA materials, respectively.

The property of surface chemical states were analyzed by X-ray photoelectron spectroscopy (XPS). Figure 3.6b reveals the C 1s spectrum, the discernible peak

at ~ 284.4 eV correponds to the sp^2 hybrids of C=C bond; while the peak at ~ 285.6 eV can be assigned to C-S and C=N bond, suggesting S and N co-doped carbon frameworks. The relatively lower intensity peak at ~ 288.3 eV is as a result of defects and functional groups including C-N, C-O and O-C-O,[39] the defect aspects among SNGA can be straightly relevant to the I(D)/I(G) value of Raman spectroscopy. The N 1s spectrum is displayed in Figure 3.6c, and can be divided into three different peaks: pyridinic N (~ 398.1 eV), pyrrolic N (~ 399.9 eV) and graphitic N (~ 401.7 eV), respectively, demonstrating different N species within the carbon support.[40] The individual spectra of Ni 2p and Co 2p are presented in Figure 3.6d and e, both of Ni and Co elements can be fitted by two spin-orbit doublets and satellite peaks. The doublets include low, *i.e.* Ni 2p3/2 and Co 2p3/2, and the Ni 2p1/2 and Co 2p1/2 from high energy bands, respectively, proving the existence of both +2 and +3 valence states of Ni and Co.[16, 19] The S 2p spectrum in Figure 3.6f can be split to two primary peaks located at ~ 162.0 and ~ 163.2 eV and one shake-up satellite at ~ 169.0 eV. The one at ~ 163.2 eV was assigned to metal-sulfur bonds, and the peak at 162.0 eV could be ascribed to sulfur atoms in low coordination numbers on the surface.[41, 42]

3.3.2 Electrochemical energy storage

To illustrate the electrochemical energy storage properties of the designed electrode materials, cyclic voltammetry (CV) and galvanostatic charge-discharge (GCD) tests were conducted by pressing the as-obtained active materials directly into the Ni foam as the conductive agent- and binder-free working electrodes in a three-electrode configuration. The optimized specific capacity of the materials was acquired by controlling the composition of metal sulfide nanostructures. From Figure 3.7a, the gravimetric specific capacities of $CoNi_2S_4$/SNGA, $NiCo_2S_4$/SNGA, Ni-S/SNGA and Co-S/SNGA were 192.1, 190.9, 167.5 and 184.0 mAh g^{-1} at 10 A g^{-1}, respectively.

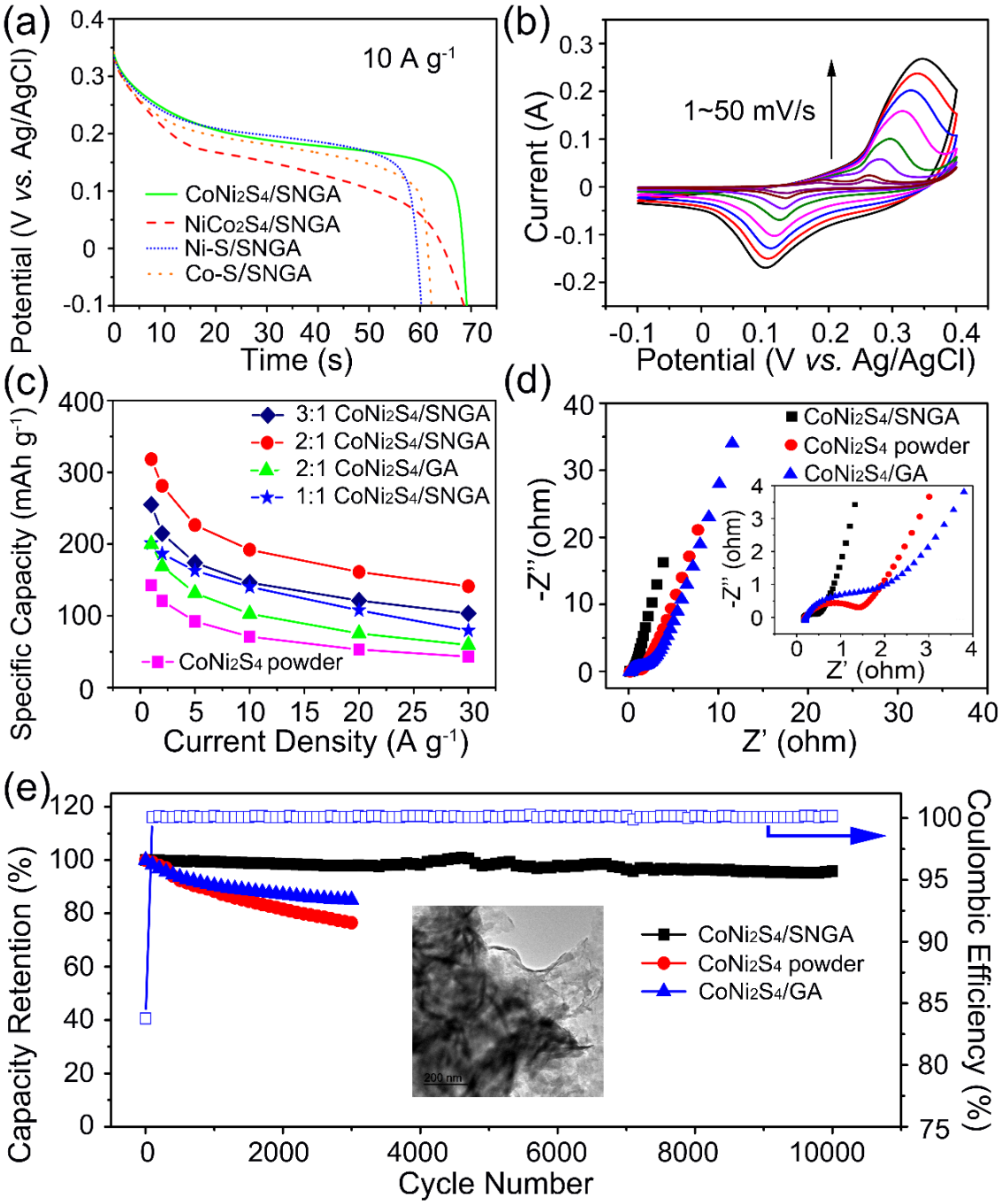

Figure 3. 7 (a) Discharge plots of several kinds of active materials at a current density of 10 A g^{-1}; (b) Cyclic voltammetry curves of $CoNi_2S_4$/SNGA at different scan rates; (c) The relationship between discharge capacity for controlled mass ratios of $CoNi_2S_4$/SNGA, $CoNi_2S_4$/GA and $CoNi_2S_4$ powders with current densities; (d) Nyquist plots of $CoNi_2S_4$/SNGA, $CoNi_2S_4$/GA and $CoNi_2S_4$ electrodes, inset showing high-frequency range of EIS spectra; (e) Stability test of the $CoNi_2S_4$/SNGA electrode for 10000 cycles and $CoNi_2S_4$/GA and $CoNi_2S_4$ electrodes for 3000 cycles, respectively, inset demonstrating the morpology evolution reflected by TEM of $CoNi_2S_4$/SNGA after long-term cycles.

The best performing active material is the $CoNi_2S_4$/SNGA although similar values could be detected from $NiCo_2S_4$/SNGA. This is due to more abundant active sites and the synergistic effect of both nickel and cobalt species in hybrids. Figure 3.7b revealed the CV plots of $CoNi_2S_4$/SNGA electrodes within the voltage range of -0.1 to 0.4 V at scan rates from 1 to 50 mV s^{-1}.

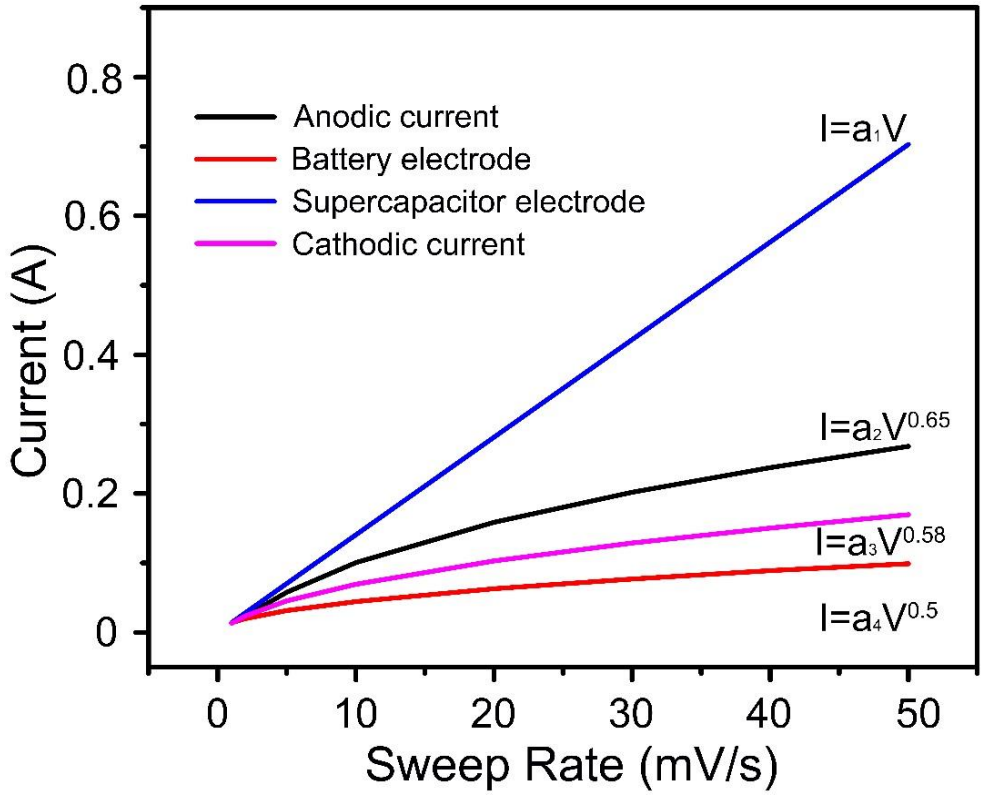

Figure 3. 8 The peak current as a function of the sweep rate from the CV curves for $CoNi_2S_4$/SNGA electrodes, ideal supercapacitor electrode and battery electrode, respectively.

As defined by Dunn. *et al*[43], if an electrochemical redox process is restricted by diffusion-controlled battery type, the peak current I varies as sweep rate $V^{1/2}$; as for a capacitive charge storage, this value varies as V, suggesting the surface-dominated process. The function relationship is noted as $I = aV^b$, where the value of b indicates the categories of charge storage mechanisms. In this electrochemical reaction, the pairs of distinct redox peaks can be noted in all CV curves. The fitted value of b = 0.65 for the anodic peak current and b = 0.58 for

cathodic peak current in Figure 3.8, the peak current I closely varies as $V^{1/2}$, suggesting diffusion-controlled reactions. The CV plots in Figure 3.7b shows that the anodic peaks shift towards more positive potentials while the cathodic ones move to negative parts, respectively. With the increase of the scan rate, these redox peaks become more distinct and only one pair can be reflected from CV curves at scan rates of 40 and 50 mV/s, suggesting the polarization of the electrodes at high sweep rates. The conspicuous peaks are on account of reversible Faradaic redox processes of Ni^{2+}/Ni^{3+} and $Co^{2+}/Co^{3+}/Co^{4+}$ redox couples shown as follows:

$$NiS + OH^- \rightleftarrows NiSOH + e^- \quad (3.12)$$

$$CoS + OH^- \rightleftarrows CoSOH + e^- \quad (3.13)$$

$$CoSOH + OH^- \rightleftarrows CoSO + H_2O + e^- \quad (3.14)$$

Overall, Ni and Co-based materials in alkaline aqueous reaction systems for electrochemical energy storage application were defined as rechargeable alkaline battery electrodes from this chapter instead of the normally regarded capacitor-type electrodes in the literature.

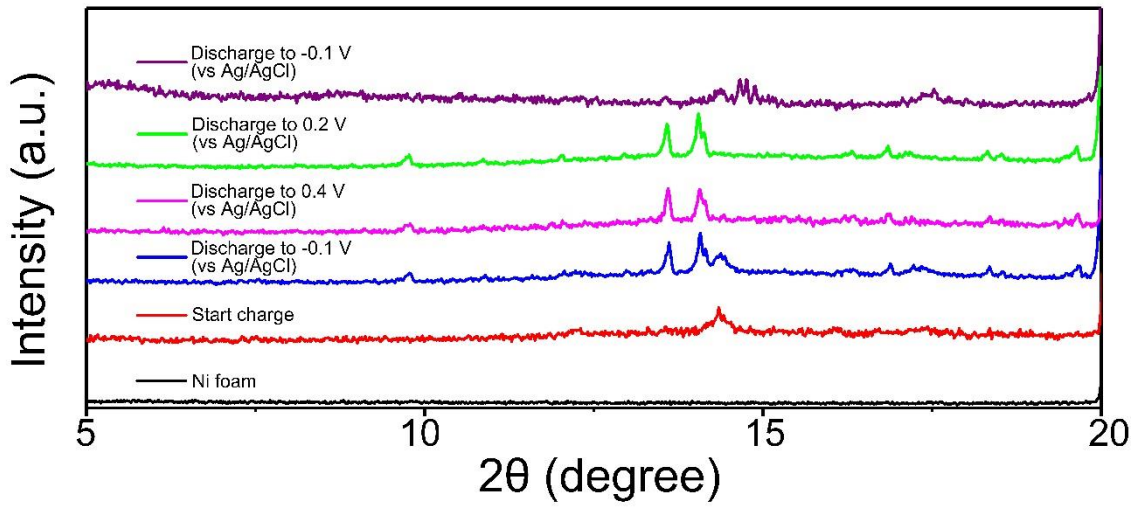

Figure 3. 9 *Ex-situ* XRD measurements of $CoNi_2S_4$/SNGA electrodes at different potentials during charge and discharge processes.

Ex-situ XRD tests of $CoNi_2S_4$/SNGA electrodes during different electrochemical steps were accomplished in Figure 3.9. The change in diffraction peaks implied the phase change during reversible charge/discharge processes and reflected that bulk redox reactions occurred, further defining alkaline battery-type energy storage mechanism, contrary to the previously reported active materials which were defined as pseudocapacitor electrodes.[6, 19, 26, 28, 29, 42, 44]

By controlling different mass ratios of $CoNi_2S_4$ nanostructures and SNGA during synthesis, *i.e.* 2:1 $CoNi_2S_4$/SNGA (0.14 g of as-synthesized $CoNi_2S_4$ nanoparticles mixed with 70 mg of GO precursors), a higher specific capacity and rate capacity was realized compared with other ratio electrodes. In comparison with $CoNi_2S_4$ nanoclusters and the same 2:1 ratio of $CoNi_2S_4$/GA, 1:1 and 3:1 ratio $CoNi_2S_4$/SNGA electrodes proved higher specific capacity. The specific capacities of 2:1 $CoNi_2S_4$/SNGA were 318.3, 281.3, 226.5, 192.1, 161.1 and 141.2 mAh g^{-1} at current densities of 1, 2, 5, 10, 20 and 30 A g^{-1}, respectively, calculated from discharge curves. The rate capability was ~ 44.3 % retention compared to the original value as current densities increased 30 times. The best performed $CoNi_2S_4$/SNGA is because of an optimized ratio of active materials and porous structures. All of the other experiments were carried out using 2:1 mass ratio of $CoNi_2S_4$ to SNGA accordingly unless stated otherwise.

The electronic conductivities of $CoNi_2S_4$/SNGA, $CoNi_2S_4$/GA and $CoNi_2S_4$ nanostructures are supposed to further elucidate the noted discrepancy in electrochemical performances among these electrodes. The Nyquist plots detected from electrochemical impedance spectra (EIS) were exhibited in Figure 3.7. These plots contained a semicircle in the high-to-medium frequency region, shown in the inset in Figure 3.7d, and a slope line in the low frequency area. The semicircle corresponds to the charge transfer process within the interface of electrode and electrolyte, and the slope line indicates the electrolyte diffusion process (mainly OH^- ions) into the bulk structure of the active materials, *i.e.*

Warburg diffusion.[44, 45] As for $CoNi_2S_4$/SNGA electrodes, the gradient was larger suggesting the Warburg resistance (Zw) is not the determining factor. Therefore, $CoNi_2S_4$/SNGA electrode could deliver more stored charges.

The equivalent circuit model of this battery-type system is shown in Figure 3.10. The inherent resistances of active materials, bulk resistance of electrolyte and interface contact resistance between electrolyte and active materials can be reflected from the equivalent series resistance (Rs). The fitted Rs values were 0.155, 0.192 and 0.185 Ω for $CoNi_2S_4$/SNGA, $CoNi_2S_4$/GA and $CoNi_2S_4$ nanostructures, respectively. The low resistance are of the similar values for these three electrodes, which can explain the spinel structures of $CoNi_2S_4$ deliver metallic electronic conductivity.[31] GA reduced from GO with a lower reduction degree could lead to a decline of the electronic conductivity of the electrodes to some extent. The semi-circle region in the high-frequency was used to determine the charge-transfer resistance (Rct), which are 0.43, 2.02 and 1.37 Ω for $CoNi_2S_4$/SNGA, $CoNi_2S_4$/GA and $CoNi_2S_4$ nanoclusters, respectively. The relatively low specific capacity of $CoNi_2S_4$ powder fabricated electrodes can be clarified by the same binder-free electrode fabrication, which result in the leakage of active materials during electrochemical working conditions. The $CoNi_2S_4$/SNGA one exhibited the smallest resistance among the three electrodes, its electronic conductivity provides an advantage for realizing the high-performance rechargeable alkaline battery electrode.

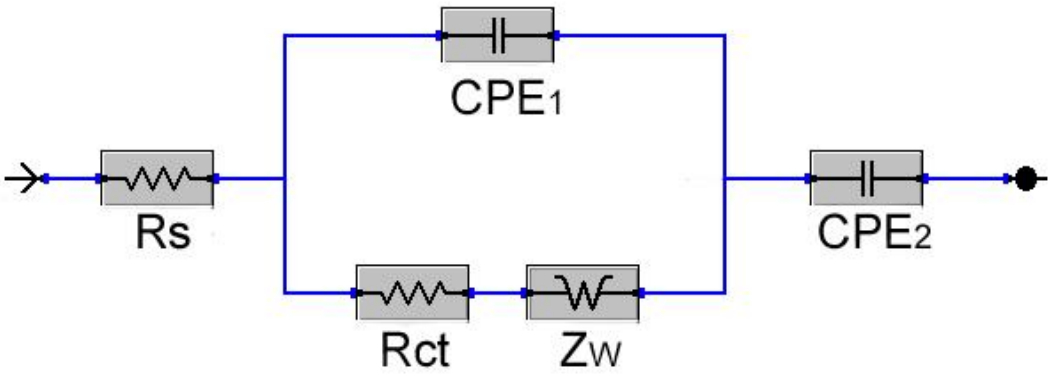

Figure 3. 10 Equivalent circuit of EIS for $CoNi_2S_4$/SNGA.

As reported previously, metal sulfides, especially the surface of these materials, can be electrochemically transformed to metal hydroxides during repeated cycling charge/discharge tests.[28] Actually, the challenge of metal sulfides materials when used in elelctrochemical energy storage application is poor durability, due to the decline of electronic conductivity when forming metal hydroxide materials. The long-term cyclic GCD measuements for as-fabricated $CoNi_2S_4$/SNGA elelctrodes were carried out at the high current density of ~ 10 A g^{-1}. It is noted that the specific capacity of the 10000th cycle was ~ 95.8 % of its initial value. The Coulombic efficiency of the electrodes stayed at ~ 100 % except for the first few cycles, suggesting an excellent reversible redox process and cyclability. The same test were conducted for $CoNi_2S_4$/GA and $CoNi_2S_4$ powdery electrodes, however, the retention of specific capacity of the 3000th cycle for $CoNi_2S_4$/GA and $CoNi_2S_4$ powder samples was ~ 85.1 % and ~ 76.5 % compared to its original value under the same test conditions.

The TEM images in inset of Figure 3.7e and the mapping images in Figure 3.11 after cycling test confirmed the structural and compositional stability of the $CoNi_2S_4$/SNGA electrodes. The morphology of $CoNi_2S_4$ nanorods became rough because of the long-term electrochemical reaction which may etch the materials. However, the $CoNi_2S_4$ nanostructures were still capped by SNGA frameworks. Sulfur and nitrogen can also be perceived in the elemental mapping images, which implies that the hybrid design, especially the SNGA aerogel, improves the structural stability of $CoNi_2S_4$ and slows down the electrochemical oxidation of the metal sulfides materials.

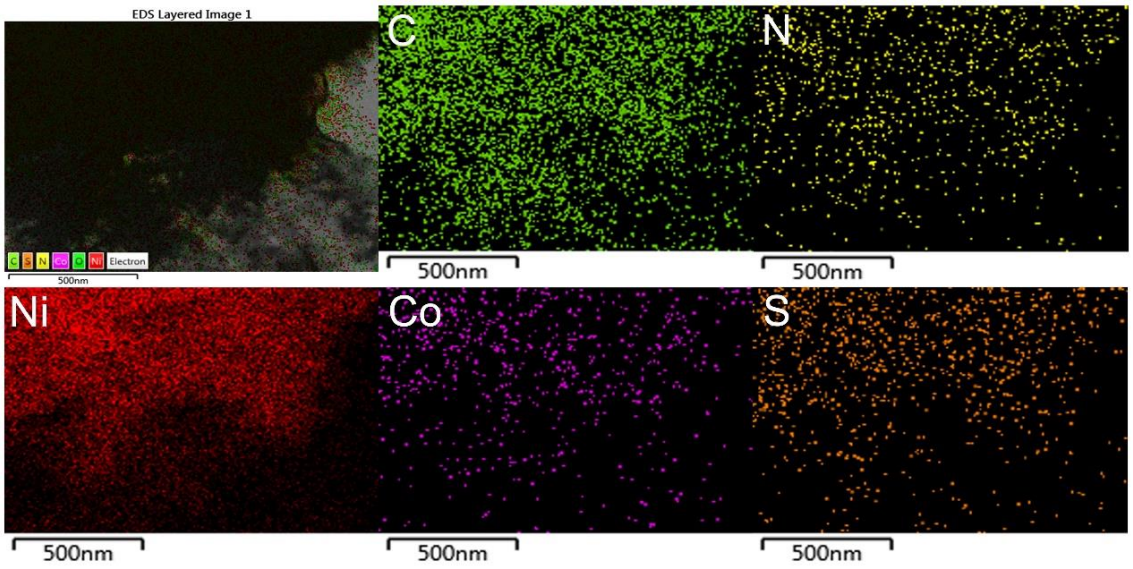

Figure 3. 11 TEM-EDS mapping images of the $CoNi_2S_4$/SNGA active materials after 10000 GCD cycles.

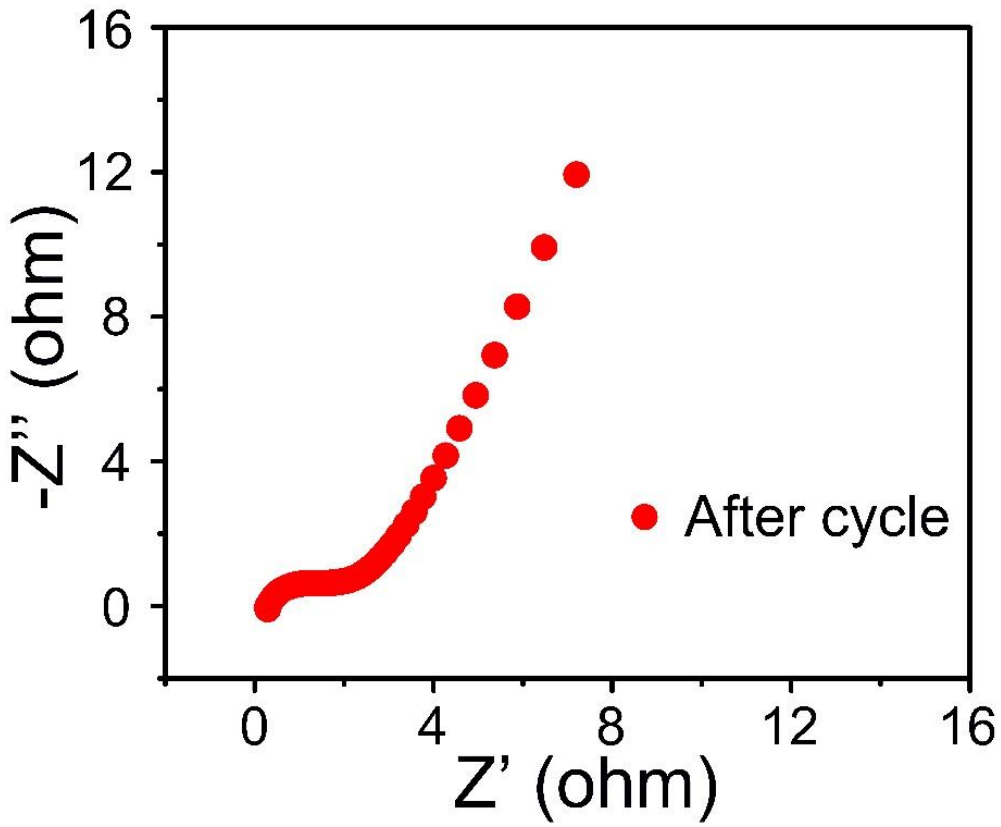

Figure 3. 12 The EIS spectrum of $CoNi_2S_4$/SNGA electrodes after 10000 GCD cycles.

The EIS spectrum after cycling stability were presented in Figure 3.12 and showed the values of Rs and Rct are 0.294 and 1.85 Ω, respectively, which increased slightly in comparison with their initial values, and have relatively smaller or comparable values compared to other binder-free transition metal sulfide electrodes in the initial states from the literature.[19, 44, 46]

To assess $CoNi_2S_4$/SNGA electrodes for practical applications, a quasi-solid-state hybrid device was fabricated by utilizing nickel foam supported $CoNi_2S_4$/SNGA materials as the cathode; the SNGA in nickel foam as the anode; a mixture of 2 M KOH-PVA solution as the electrolyte and glassy fiber paper as the separator. Solid-state hybrid battery has similar components as previously reported asymmetric supercapacitors. The electrochemical reactions at the anode was the same as in three electrodes by reactions 3.12-3.14. The negative electrode is attributed to electrical double layer capacitor (EDLC) and somewhat pseudocapacitor contribution, which has the mechanisms of electrostatic adsorption for energy storage at the interface of the carbon and redox reactions between ions and defect-rich structure of doped graphene aerogel. Possible reactions are: [47, 48]

$$-C=O(S) + OH^- \rightleftarrows -CO(S)OH + e^- \quad (3.15)$$

$$-CH=NH + OH^- \rightleftarrows -CH\text{-}NHOH + e^- \quad (3.16)$$

The device is defined as the hybrid battery due to its hybrid mechanisms of rechargeable alkaline battery and supercapacitor electrodes. Figure 3.13a shows the CV curves of a solid-state hybrid battery (SNGA//$CoNi_2S_4$/SNGA) in a potential range of 0~1.6 V, at scan rates from 10~200 mV s^{-1}. CV curves showed mixed charge storage of both a surface- and a diffusion-controlled processes. The volumetric capacity of the hybrid battery was calculated according to GCD tests in Figure 3.13b. The fabricated SNGA//$CoNi_2S_4$/SNGA device possessed a volumetric capacity of 2.37, 1.99, 1.49, 1.24, 1.14, 0.92 and 0.76 mAh cm^{-3} at 1, 2, 5, 8, 10 and 20 mA cm^{-2}, respectively. The voltage plateaus were not prominent, which indicated a hybrid feature similar to a pseudocapacitor. Energy and power

density based on volumes are two pivotal parameters for evaluating performance of devices. Figure 3.13c depicts the Ragone plot of the as-fabricated hybrid battery based on its whole volume. The energy density and power density of the hybrid battery were estimated by the well-defined equations in experimental sections (equation 4-10). Accordingly, the device delivered a superb volumetric maximum output power density of 17.5 W cm^{-3} and retained the high energy density of 1.95 mWh cm^{-3} at 1 mA. The value remained no obvious decrease with an increase of the applied current. The performance herein is comparable or better than most of the previously reported symmetric or asymmetric devices (SDs or ADs)[49] based on the whole volume of devices, such as ZnO@C@MnO_2[50], TiO_2@C[51], WO_{3-x}/MoO_{3-x}//PANI/carbon fabric[52], H-TiO_2@MnO_2//H-TiO_2@C[53], laser-scribed graphene[54], MnO_2//Fe_2O_3[55], Co_9S_8//Co_3O_4@RuO_2[56] and ZnO@MnO_2//RGO[57]. The cycling stability from the GCD test, at a high current of 20 mA, for the hybrid battery is shown in Figure 3.13d. It proved high cyclability and an overall capacity decrease of around ~ 0.002 % per cycle over 8000 cycles. The Coulumbic efficiency of the hybrid battery stayed at ~ 100 %. Moreover, introducing new gel electrolyte into the quasi-solid-state hybrid battery, dramatically increased the capacity after several hundred cycles, which manifested a reduction of specific capacity as further water evaporation in the electrolyte thus inducing an increase of internal resistance in the device.

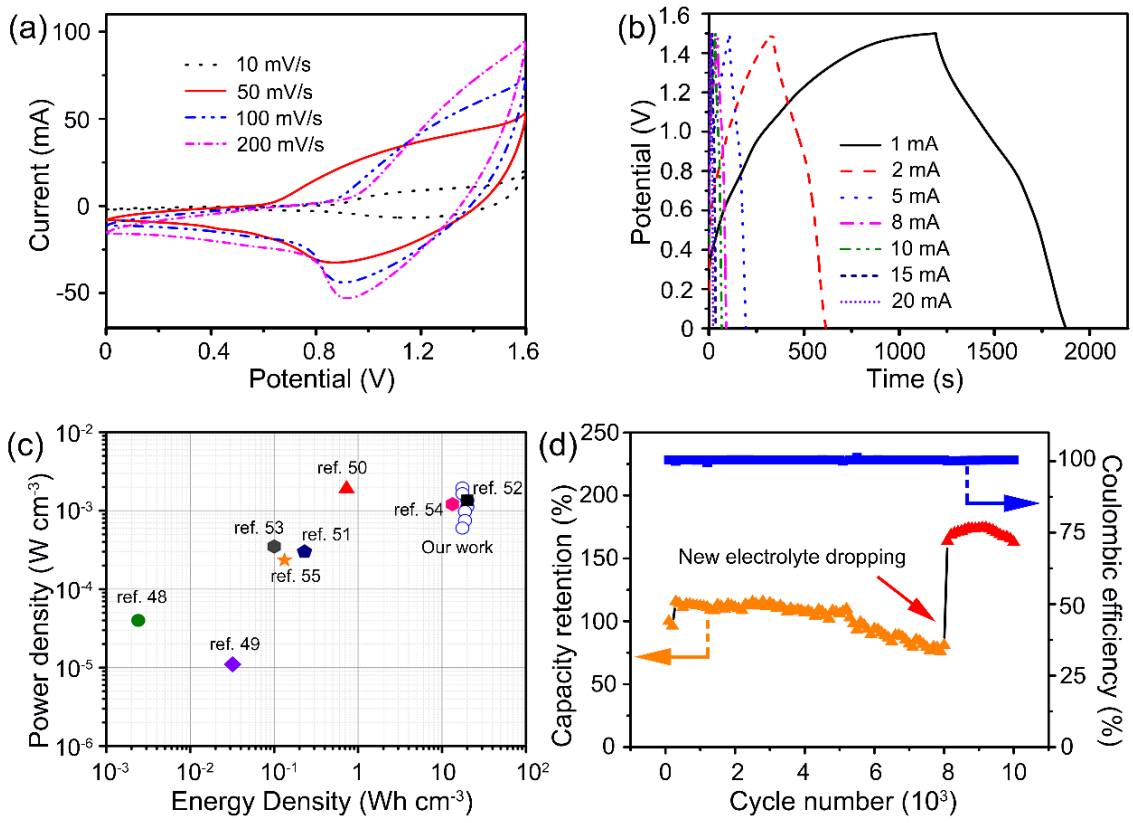

Figure 3. 13 (a) CV tests for the hybrid battery at a series of scan rates; (b) GCD curves at different currents; (c) Ragone plot of the hybrid battery in this work and compared with some state of the art devices in literature; (d) Cycling performance of the devices at a current of 20 mA.

Ni-Co-S ternary metal sulfides could be utilized in electrocatalysis for oxygen as these materials deliver noble-metal like catalytic behaviours, while their performance declined when used in an aqueous electrolyte such as O_2-saturated KOH. Therefore, the use of Ni-Co-S/SNGA materials as ORR catalysts was further explored. Figure 3.14a shows the CV plots of Ni-Co-S/SNGA materials in O_2-saturated 0.1 M KOH. The peak potential of Co-S/SNGA eletrodes (0.750 V *vs.* RHE) is more positive than other Ni-Co-S/SNGA nanostructures, with similar values of 0.746 V *vs.* RHE for $NiCo_2S_4$/SNGA. The ORR performances of the four catalysts were further compared by rotating-disk electrode (RDE) tests as shown in Figure 3.14b. The Co-S/SNGA materials showed an onset potential of 1.0 V *vs*. RHE and limiting current density of 4.6 mA cm^{-2}, which represents the best performing catalyst compared with other Ni-Co-S/SNGA nanostructures. As

reported, the ORR performance of the catalysts declines with an increased amount of Ni^{3+} species in Ni-Co-S.[58] From the results of LSV curves, with an increase of Ni ions in the hybrids, the ORR performance declined accordingly. The electron transfer number of Co-S/SNGA falled into the range of 3.8~3.95 within the potential range of 0.2~0.8 *vs.* RHE, suggesting the four-electron pathway catalytic process. Stability is another important parameter to evaluate the performance of ORR catalysts. Compared with the counterparts, the Co-S/SNGA catalysts delivered better stability, and maintained ~ 88.6 % of its initial value after 12000 s of CA tests at a rotation rate of 1600 rpm in O_2-saturated 0.1 M KOH electrolyte, higher than that of Co-S nanoparticles and Co-S/GA.

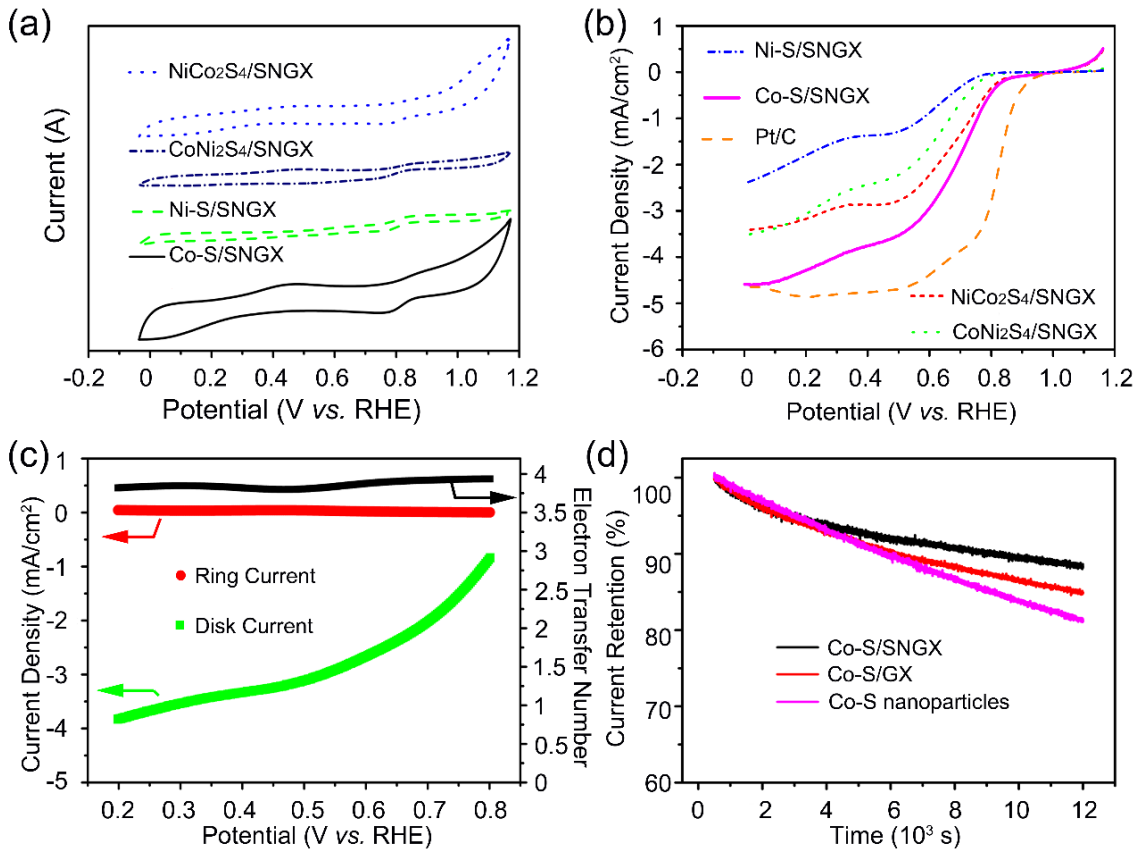

Figure 3. 14 (a) CV plots of four types of Ni-Co-S/SNGA materials; (b) Rotating-disk electrode (RDE) measurement of Ni-Co-S/SNGA and commercial Pt/C materials; (c) Rotating ring-disk electrode (RRDE) test of Co-S/SNGA. Current densities showed by green curve on the disk (i_{disk}) and red curve on the ring (i_{ring}) electrodes respectively, and the electron transfer number in black curve; (d) Current-time chronoamperometric (CA) responses of Co-S/SNGA, Co-S/GA and Co-S nanostructures at a rotation rate of 1600 rpm.

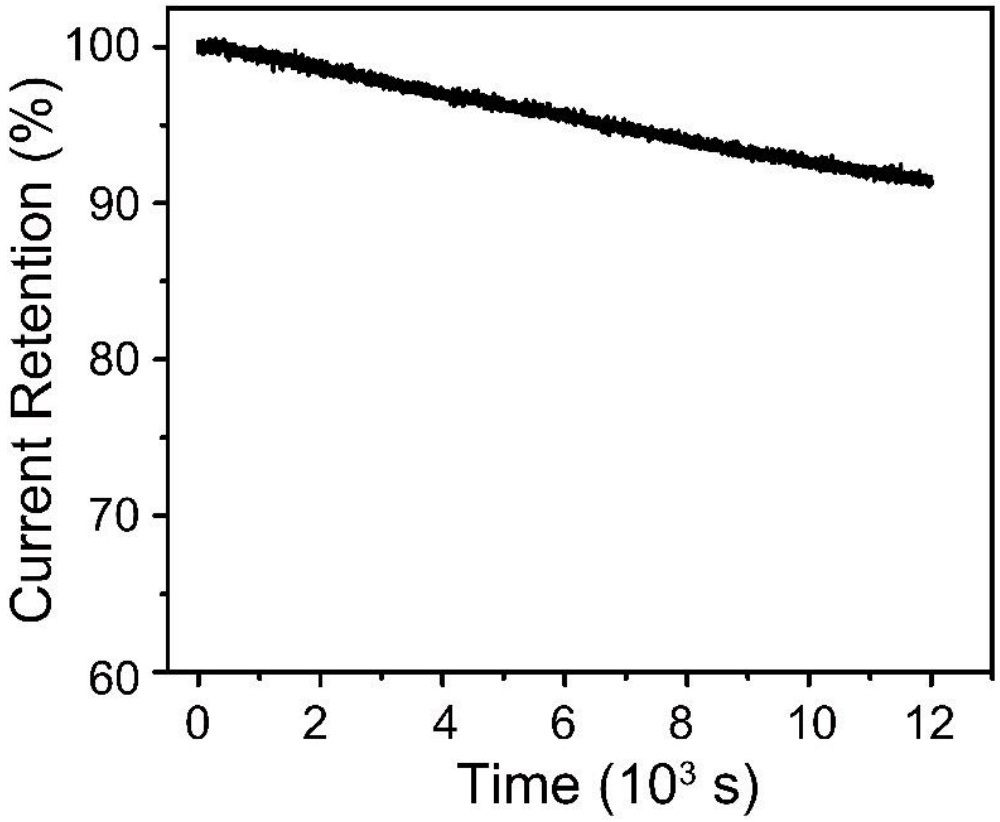

Figure 3. 15 Current−time chronoamperometric responses of $NiCo_2S_4$/SNGA at a rotation rate of 800 rpm for 12000 s in O_2-saturated 0.1 M KOH.

The practicability of these structures can also be proved by $NiCo_2S_4$/SNGA nanostructures, with the ~ 91.5 % retention (Figure 3.15) after 12000 s in the CA responses.

3.4 Conclusion

In this chapter, a strategy was developed by using SNGA aerogels to endose Ni-Co-S materials with the target of improving the electrochemical performances of energy storage and conversion, especially the stability of Ni-Co-S ternary metal sulfides for rechargeable alkaline battery electrodes and ORR catalysts. Among four types of Ni-Co-S/SNGA, $CoNi_2S_4$/SNGA nanostructures presented the best performance as electrode materials, and exhibited a high gravimetric discharge

capacity of 318.3 mAh g^{-1} at a current density of 1 A g^{-1}. The material showed a high rate performance of 44.3 % retention of its initial value after a 30 times increase of the current density. A capacity retention of ~ 95.8 % was noted after a long GCD cycle of 10000 times from a three-electrode test configuration. The hybrid battery based on $CoNi_2S_4$/SNGA as the cathode and SNGA as the anode showed a superb volumetric power density of 17.5 W cm^{-3} while it maintained the relatively high volumetric enegy density of 1.95 mWh cm^{-3} at a current of 1 mA. The hybrid battery showed excellent cycling performance and a capacity decrease of only ~ 0.002 % per cycle over 8000 cycles. When these materials were used as electrocatalysts in ORR, an increase of Ni ion in the hybrid structures could decrease the electrocatalytic performance. Moreover, SNGA structures capped with metal sulfides exhibited enhanced stability for ORR. Importantly, the commonly regarded supercapacitor electrodes based on Ni or Co-based materials as electrode was confirmed as rechargeable alkaline batteries from a kinetic view in this chapter. The detailed caculation formulas for evaluating hybrid devices were proposed. These contribution could serve as a standardization for performance comparisons in future work for hybrid battery systems.

Compared to the ternary transition metal materials for electrodes in Chapter 1. Both metal ions in Ni-Co-S materials participate in electrochemical energy storage applications. The energy storage mechanism is clarified in this work, which demonstrated that nickel and cobalt-based materials are not suitable for pseudocapacitors electrodes. In addition, flexible devices are attracting research attention. In the following content, the work related to bendable electrodes are designed and synthesized.

3.5 References

[1] K. S. Novoselov, A. K. Ceim, S. V. Morozov, D. Jiang, Y. Zhang, S. V. Dubonos, I. V. Grigorieva，A. A. Firsov, *Science*, **2004**, *306*, 666.

[2] C. L. A. Peigney, E. Flahaut, R. R. Bacsa, A. Rousset, *Carbon*, **2001**, *39*, 507.

[3] F. Bonaccorso, L. Colombo, G. Yu, M. Stoller, V. Tozzini, A. C. Ferrari, R. S. Ruoff, V. Pellegrini, *Science*, **2015**, *347*, 1246501.

[4] Y. Shao, M. F. El-Kady, L. J. Wang, Q. Zhang, Y. Li, H. Wang, M. F. Mousavi, R. B. Kaner, *Chem. Soc. Rev.*, **2015**, *44*, 3639.

[5] H. Chang, H. Wu, *Adv. Funct. Mater.*, **2013**, *23*, 1984.

[6] J. Yang, C. Yu, X. Fan, C. Zhao, J. Qiu, *Adv. Funct. Mater.*, **2015**, *25*, 2109.

[7] X. Wang, J. Wang, D. Wang, S. Dou, Z. Ma, J. Wu, L. Tao, A. Shen, C. Ouyang, Q. Liu, S. Wang, *Chem. Commun. (Camb)*, **2014**, *50*, 4839.

[8] Z. Chen, W. Ren, L. Gao, B. Liu, S. Pei, H. M. Cheng, *Nat. Mater.*, **2011**, *10*, 424.

[9] W. Wei, S. Yang, H. Zhou, I. Lieberwirth, X. Feng, K. Mullen, *Adv. Mater.*, **2013**, *25*, 2909.

[10] C. Zhao, C. Yu, S. Liu, J. Yang, X. Fan, H. Huang, J. Qiu, *Adv. Funct. Mater.*, **2015**, *25*, 6913.

[11] J. T. Tai, Y. C. Lai, J. H. Yang, H. C. Ho, H. F. Wang, R. M. Ho, D. H. Tsai, *Anal. Chem.*, **2015**, *87*, 3884.

[12] Y. Xu, Z. Lin, X. Zhong, X. Huang, N. O. Weiss, Y. Huang, X. Duan, *Nat. Commun.*, **2014**, *5*, 4554.

[13] L. M. Dai, L. T. Qu, H. Choi, J. B. Baek, *Chem. Rev.*, **2015**, *115*, 4823.

[14] D. Higgins, P. Zamani, A. Yu, Z. Chen, *Energy Environ. Sci.*, **2016**, *9*, 357.

[15] Z. Yu, L. Tetard, L. Zhai, J. Thomas, *Energy Environ. Sci.*, **2015**, *8*, 702.

[16] D. Bhattacharjya, A. Sinhamahapatra, J. J. Ko, J. S. Yu, *Chem. Commun. (Camb)*, **2015**, *51*, 13350.

[17] R. Zou, Z. Zhang, M. F. Yuen, M. Sun, J. Hu, C.-S. Lee, W. Zhang, *NPG Asia Mater.*, **2015**, *7*, e195.

[18] R. Zou, K. Xu, T. Wang, G. He, Q. Liu, X. Liu, Z. Zhang, J. Hu, *J. Mater. Chem. A*, **2013**, *1*, 8560.

[19] B. Yang, L. Yu, H. Yan, Y. Sun, Q. Liu, J. Liu, D. Song, S. Hu, Y. Yuan, L. Liu, J. Wang, *J. Mater. Chem. A*, **2015**, *3*, 13308.

[20] H. Hu, B. Y. Guan, X. W. Lou, *Chem*, **2016**, *1*, 102.

[21] X. Y. Yu, L. Yu, X. W. Lou, *Adv. Energy Mater.*, **2016**, *6*, 1501333.

[22] L. Yu, L. Zhang, H. B. Wu, X. W. Lou, *Angew. Chem. Int. Ed.*, **2014**, *53*, 3711.

[23] Z. Zhang, X. Wang, G. Cui, A. Zhang, X. Zhou, H. Xu, L. Gu, *Nanoscale*, **2014**, *6*, 3540.

[24] J. Wu, S. Dou, A. Shen, X. Wang, Z. Ma, C. Ouyang, S. Wang, *J. Mater. Chem. A*, **2014**, *2*, 20990.

[25] D. Kong, J. J. Cha, H. Wang, H. R. Lee, Y. Cui, *Energy Environ. Sci.*, **2013**, *6*, 3553-3558.

[26] L. Shen, J. Wang, G. Xu, H. Li, H. Dou, X. Zhang, *Adv. Energy Mater.*, **2015**, *5*, 1400977.

[27] H. Chen, L. Hu, M. Chen, Y. Yan, L. Wu, *Adv. Funct. Mater.*, **2014**, *24*, 934.

[28] L. Shen, L. Yu, H. B. Wu, X. Y. Yu, X. Zhang, X. W. Lou, *Nat. Commun.*, **2015**, *6*, 6694.

[29] R. Zou, Z. Zhang, M. F. Yuen, J. Hu, C. S. Lee, W. Zhang, *Sci. Rep.*, **2015**, *5*, 7862.

[30] H. Wang, Y. Liang, Y. Li, H. Dai, *Angew. Chem. Int. Ed. Engl.*, **2011**, *50*, 10969.

[31] C. Xia, P. Li, A. N. Gandi, U. Schwingenschlögl, H. N. Alshareef, *Chem. Mater.*, **2015**, *27*, 6482.

[32] X. Liu, X. Wang, B. Zhou, W.-C. Law, A. N. Cartwright, M. T. Swihart, *Adv. Funct. Mater.*, **2013**, *23*, 1256.

[33] W. Maneeprakorn, M. A. Malik, P. O'Brien, *J. Mater. Chem.*, **2010**, *20*, 2329.

[34] C. Yuan, B. Gao, L. Su, L. Chen, X. Zhang, *J. Electrochem. Soc.*, **2009**, *156*, A199.

[35] S. Chen, S. Qiao, *ACS Nano*, **2013**, **7**, 10190.

[36] M. Seredych, T. J. Bandosz, *J. Mater. Chem. A*, **2013**, *1*, 11717.

[37] X. Wang, G. Li, M. H. Seo, F. M. Hassan, M. A. Hoque, Z. Chen, *Adv. Energy Mater.*, **2015**, *5*, 1501106.

[38] B. Zhao, S.-Y. Huang, T. Wang, K. Zhang, M. M. F. Yuen, J.-B. Xu, X.-Z. Fu, R. Sun, C.-P. Wong, *J. Power Sources*, **2015**, *298*, 83.

[39] Y. Gao, H. Zhao, D. Chen, C. Chen, F. Ciucci, *Carbon*, **2015**, *94*, 1028.

[40] L. Fu, Y. Chen, Z. Liu, *J. Mol. Catal. A: Chem.*, **2015**, *408*, 91.

[41] Q. Liu, Z. Wu, Z. Ma, S. Dou, J. Wu, L. Tao, X. Wang, C. Ouyang, A. Shen, S. Wang, *Electrochimi. Acta*, **2015**, *177*, 298.

[42] M. Sun, J. Tie, G. Cheng, T. Lin, S. Peng, F. Deng, F. Ye, L. Yu, *J. Mater. Chem. A*, **2015**, *3*, 1730.

[43] P. Simon, Y. Gogotsi, B. Dunn, *Science*, **2014**, *343*, 1210.

[44] J. Xiao, L. Wan, S. Yang, F. Xiao, S. Wang, *Nano Lett.*, **2014**, *14*, 831.

[45] G. He, J. Li, W. Li, B. Li, N. Noor, K. Xu, J. Hu, I. P. Parkin, *J. Mater. Chem. A*, **2015**, *3*, 14272.

[46] H. Huo, Y. Zhao, C. Xu, *J. Mater. Chem. A*, **2014**, *2*, 15111.

[47] C. Wang, W. Wen, H. Hsu, B. Yao. *Adv. Powder Technol.* **2016**, *27*, 1387.

[48] L. Sun, L. Wang, C. Tian, T. Tan, Y. Xie, K. Shi, M. Li, H. Fu, *RSC Advances*, **2012**, *2*, 4498.

[49] X. Lu, M. Yu, G. Wang, Y. Tong, Y. Li, *Energy Environ. Sci.*, **2014**, **7**, 2160.

[50] P. Yang, X. Xiao, Y. Li, Y Ding, P. Qiang, X. Tan, W. Mai, Z. Lin, W. Wu, H. Jin, P. Liu, J. Zhou, C. P. Wong, Z. L. Wang, *ACS Nano*, **2013**, *7*, 2617.

[51] H. Zheng, T. Zhai, M. Yu, S. Xie, C. Liang, W. Zhao, S. C. I. Wang, Z. Zhang, X. Lu, *J. Mater. Chem. C*, **2013**, *1*, 225.

[52] X. Xiao, T. Ding, L. Yuan, Y. Shen, Q. Zhong, X. Zhang, Y. Cao, B. Hu, T. Zhai, L. Gong, J. Chen, Y. Tong, J. Zhou, Z. L. Wang, *Adv. Energy Mater.*, **2012**, *2*, 1328.

[53] X. Lu, M. Yu, G. Wang, T. Zhai, S. Xie, Y. Ling, Y. Tong, Y. Li, *Adv. Mater.*, **2013**, *25*, 267.

[54] V. S. Maher F. El-Kady, Sergey Dubin, R. B. Kaner, *Science*, **2012**, *335*, 1326.

[55] X. Lu, Y. Zeng, M. Yu, T. Zhai, C. Liang, S. Xie, M. S. Balogun, Y. Tong, *Adv.*

Mater., **2014**, *26*, 3148.

[56] J. Xu, Q. Wang, X. Wang, Q. Xiang, B. Liang, D. Chen, G. Shen, *ACS Nano*, **2013**, ***7***, 5453.

[57] Z. Wang, Z. Zhu, J. Qiu, S. Yang, *J. Mater. Chem. C*, **2014**, *2*, 1331.

[58] Q. Liu, J. Jin, J. Zhang, *ACS Appl. Mater. Interfaces*, **2013**, *5*, 5002.

Chapter 4

Tungsten Nitrides Used as Self-standing Electrodes for High-performance Supercapacitors

4.1 Introduction

In previous chapters, the definition of supercapacitors and batteries, especially Li-ion battery was described. Commonly regarded pseudocapacitor materials, *i.e.* Ni and Co nanostructures in aqueous electrolyte, were identified as battery-type charge storage mechanism. As a promising type of energy storage configurations, supercapacitors, especially pseudocapacitors, could deliver higher power densities than the metal-ion batteries.[1] In this chapter, the design and synthesis of high-performance active materials for pseudocapacitor are presented. The practical applications of normally reported pseudocapacitor materials, such as amorphous RuO_2,[2,3] MnO_2[4] and WO_3[5], *etc.*, require further enhancement around specific capacitance and energy density. As an emerging class of electrode materials, metal nitrides exhibit superb electrical conductivity (4000-55500 S cm^{-1}) and improved charge storage and transfer properties. Prof. Hong Jin Fan's group reported the fabrication of devices by TiN cathodes and Fe_2N anodes, which realized high-rate and stable asymmetric supercapacitors[6]. From their statement, structural modifications, such as carbon coating, was declared effective to further improve the stability of metal nitrides during electrochemical reactions. Among all the reported transiton metal and their derivatives in electrochemical energy storage applications, tungsten-based active materials possess numerous intrinsic advantages, such as relatively low toxicity and cost, high specific capacitance and excellent cyclability[5,7,8]. Intensive studies have been reported to utilize tungsten oxide as electrodes in pseudocapacitors, for some examples: MoO_{3-x}/WO_{3-x} core-shell nanostructures on carbon cloth[8]; titanium foam supported WO_3 nanoflowers[9] and WO_3/graphene aerogel composites[10]. These materials deliver enhanced electrochemical energy storage performances compared to pure WO_3 couterparts by the design and fabrication of nanostructure and composites. However, tungsten-based materials for electrodes still need further modification, either in synthetic technique, electrode fabrication or performance amelioration to meet practical requirements. It is worth

noting that little work has been reported using tungsten nitrides for electrochemical charge storage applications[11] and no previous work has uncovered the origin of their excellent pseudocapacitive performance. Moreover, no comprehensive research has been conducted so far related to device fabrication based on tungsten nitride active materials.

As an alternative approach of commonly reported electrode making procedure, the strategies for design of self-standing electrodes include integration of active materials and conductive current collectors, such as elastic carbon films[12] and metal substrates supported electrodes[9,13], which eliminated the sophisticated electrodes fabrication process for powdery active mateirals. Chemical vapor deposition (CVD) has proved an effective process for surface engineering and delivers distinct advantages compared to other synthetic methods for self-standing electrodes, such as the hydrothermal synthesis and electrochemical deposition. In general, CVD is an industrially relevant technique for production of films with uniform coatings[14], which can produce more robust adhesion strength between the coated layers and the substrates. Recently, the synthesis and growth mechanism of WO_3 nanorod arrays on glass by aerosol-assisted chemical vapour deposition (AACVD) was studied from our group[14]. This approach achieves uniform film at relatively low deposition temperature compared with other types of CVD[8,15] and is potentially considerable for large-scale industrialization due to its merits of energy conservation.

In this chapter, W_2N@C core-shell structures on carbon cloth were prepared by a facile one-step AACVD (formation of WO_{3-x} and carbon coating) followed by ammoniation. The nanorod arrays on current collectors contribute to the enlarged specific surface area and have potential application as frameworks for supporting other active species for electrochemical energy storage with low electrical conductivity. Supercapacitors were fabricated by utilizing solid-state electrolyte for bendable devices and ionic liquid electrolyte for high working potential

applications. The improved electrochemical energy storage performances of W_2N materials in aqueous acid electrolyte in comparison with oxide counterparts (WO_{3-x}) were uncovered by electrochemical testing, density functional theory (DFT) calculations and *in-situ* electrical property measurements.

4.2 Experimental section

4.2.1 Synthetic process

The illustration of the AACVD is shown in Figure 4.1. Tungsten precursors [$W(CO)_6$] (99%, Aldrich) were dissolved in a mixed solution of acetone (99%, Emplura) and methanol (99.5%, Emplura) with a volumetric ratio of 2:1 to produce a solution with a concentration of 1.37×10^{-2} M. The aerosol was generated by an ultrasonic humidifier (Liquifog, Johnson Matthey operating at 2 MHz) from a precursor solution (volume was used from 5 to 25 mL to control the loading density of WO_{3-x}@C coatings) and transported to the reactor by nitrogen (99.99%, BOC) with a flow rate of 300 standard cubic centimeter per minutes (sccm) controlled by a mass flow controller (MFC, Brooks). After deposition of all the percursor solution at a temperature of 375 °C on the substrate, the heater and humidifier were switched off and naturally cooled down to room temperature. The inlet to the cold wall reactor of the AACVD system is equipped with a water jacket (filled with floating ice) and turned on during the whole deposition process, which can avoid overheating of the precursor and decompositing prior to entering the reactor chamber. The exhaust was directly vented into the extraction system of the fume cupboard. Finally, the as-synthesized electrodes were transferred into a tube furnace for annealing under a 500 sccm ammonia gas (BOC, U.K.) flow with a temperature rate of 5 ^oC/min up to 600 °C. The system was maintained at 600 °C for 3 hours and then cooled to room temperature. To remove the carbon shell from the WO_{3-x} nanorod, the as-synthesized electrodes were annealed in

air at 600 ^{o}C for 2h. W_2N/carbon cloth was annealed in NH_3 gas with the same procedure by using the carbon cloth supported WO_{3-x} nanorods.

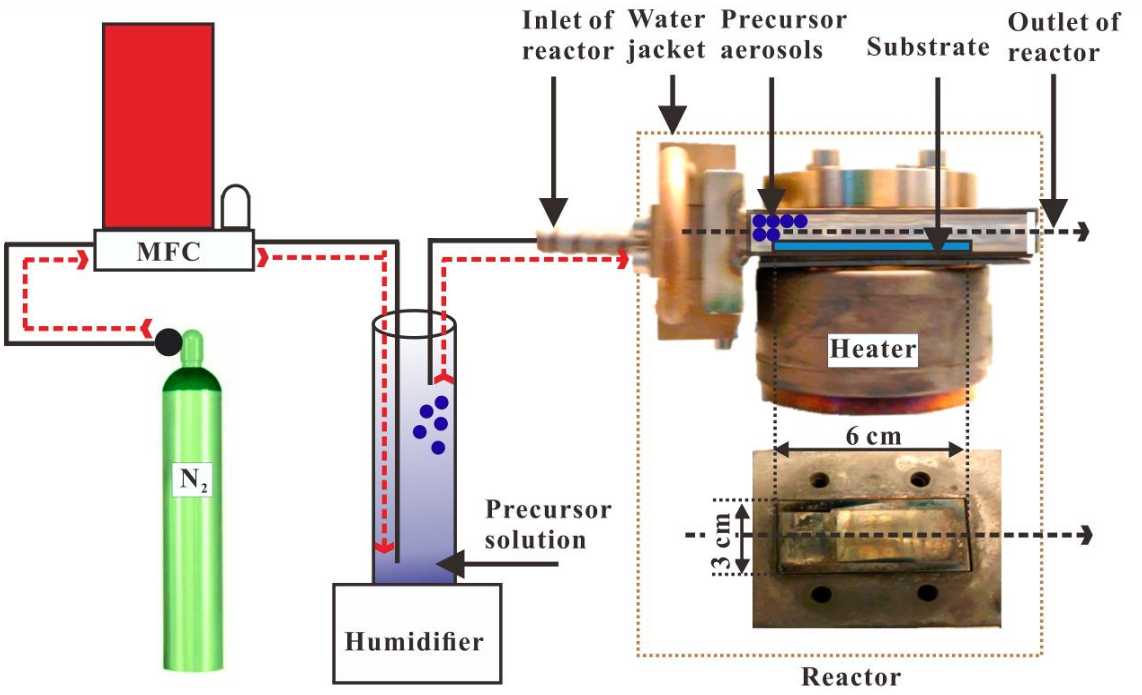

Figure 4. 1 Schematic diagram showing the Aerosol-assisted Chemical Vapour Deposition (AACVD) equipment.

4.2.2 Materials characterization

The morphology of the electrodes were characterized by scanning electron microscopy (SEM, JSM-6700F equipped with an energy-dispersive X-ray spectrometer) and TEM (JEOL, JEM-2100). The phase and chemical compositions were determined by a STOE SEIFERT diffractometer (Mo source radiation) and X-ray photoelectron spectroscopy (XPS; Thermo scientific K-alpha photoelectron spectrometer). The mass of the active materials was weighed by an analytical balance (Ohaus; δ = 0.01 mg). The *in-situ* electrical properties were measured by a transmission electron microscope-scanning tunneling microscope (TEM-STM) holder (Nanofactory Instruments AB, Goteborg, Sweden) within a

200 kV high resolution TEM (JEM-2100F) with beam-blank irradiation at low illumination.

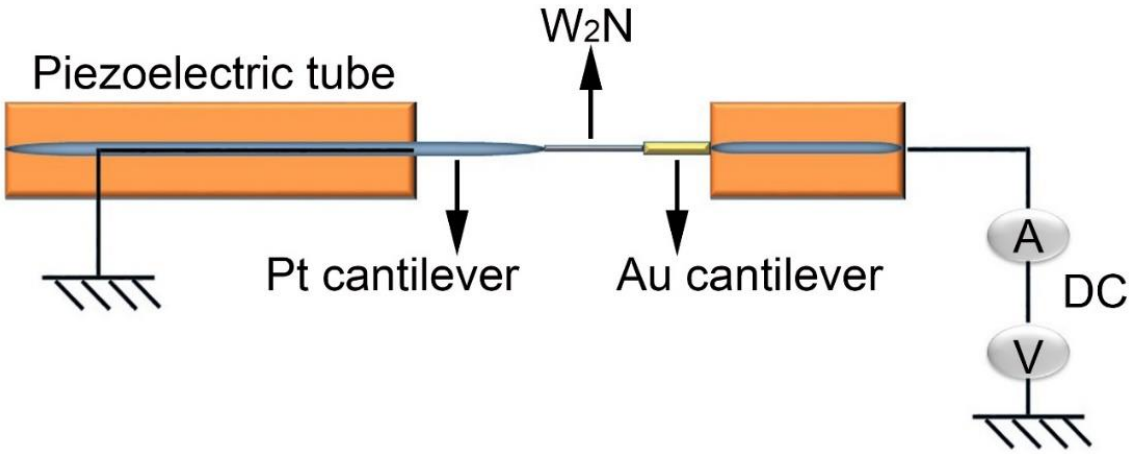

Figure 4. 2 The experimental setup of *in-situ* electrical properties test of the W_2N (WO_{3-x}) nanorod within the TEM-STM holder.

This experiment was carried out at Donghua University in collaboration with Prof. Rujia Zou. The procedure and results are included in this chapter. Firstly, a gold tip attached with the single nanorod was fitted to an electrical holder, and a platinum probe was set at the piezo-driven movable part of the holder. A tweezer was used to adapt position between the tip and probe manually under the observation of an optical microscope to minimize the possible gap. After that, the position of the Pt probe was modified by a piezodriven manipulator with nanoscale precision, and an ideal alignment resulted in the Pt probe approaching and adhering onto the nanorod on the Au tip side, forming the nanorod bridge between the Au tip and the Pt probe. Then, a current was applied to weld the contact domains of the nanorod on Au tip and Pt probe to induce a robust contact with low contact resistance between the nanorod, the tip and the probe. At last, the *in-situ* electrical property of the nanorod was appraised based on the classical electricity model by Nanofactory Instruments AB.

4.2.3 Electrochemical evaluation

The electrochemical performance of a single electrode test were conducted by potentiostats Gamry Interface 1000 or Autolab PGSTAT302N in a three-electrode configuration with 2 M H_2SO_4 as the electrolyte. A platinum foam (~ 2 cm^2) and an Ag/AgCl electrode were used as the counter and reference electrodes, respectively. The free-standing electrodes were tested directly with an area of ~ 1 cm^2 in the electrolyte. The thickness of the electrode is ~ 0.30 mm as measured by Vernier caliper (Resolution: 0.02 mm). The electrochemical impedance spectroscopy (EIS) measurements were carried out at open circuit voltage with a sinusoidal signal in a frequency range of 100 kHz to 0.01 Hz at an amplitude of 10 mV. Specific capacitances were calculated from CV plots by calculating the slope of the integrated discharge Q versus voltage range, as shown in the following equations:

$$C_{area} = \frac{\Delta Q}{S \cdot \Delta V} \qquad (4.1)$$

$$C_{mass} = \frac{\Delta Q}{m \cdot \Delta V} \qquad (4.2)$$

where C_{mass} is the gravimetric specific capacitance (F g^{-1}), C_{area} is the specific areal capacitance (mF cm^{-2}); $\frac{\Delta Q}{\Delta V}$ is the slope of the integrated discharge Q versus voltage range; m is the mass of the active materials and S is the area of the tested electrodes. The specific capacitance of W_2N@C/carbon cloth with different volumes of precursor in the AACVD process were recorded and calculated by at least three independent electrodes.

Asymmetric solid-state supercapacitors were fabricated by a piece of carbon cloth supported W_2N@C CSA as the negative electrode and flexible carbon paper loaded commercial nitrogen doped graphene (Nanjing XFNANO Materials TECH Co., Ltd) as the positive electrode, a piece of glassy fibre paper (Fisher Scientific, U.K.) as the separator and H_2SO_4-polyvinyl alcohol (PVA) as the electrolyte (5 g

of PVA were dissolved in 50 ml of distilled water at a temperature of 85 ^{o}C and cooled down to room temperature with mixing 5 g of H_2SO_4 for further use). The devices were sealed in two pieces of PET films.

Symmetric two-electrode devices in coin-type cells (CR 2032) were fabricated in the glove box by using 2 M ethyl-methyl-immidazolium tetra-fluoro-borate (EMI, BF_4) in acetonitrile as the electrolyte, two pieces of W_2N@C CSA/carbon cloth as working electrodes directly and Celgard 3501 as the separator.

Areal energy density (E_{area}, mWh cm^{-2}) and power density (P_{area}, mW cm^{-2}) were calculated based on the following equation:

$$E_{area} = \frac{C_{area}U_w^2}{S} \quad (4.3)$$

$$P_{area} = \frac{E_{area}}{t} \quad (4.4)$$

$$t = \frac{U_w}{v} \quad (4.5)$$

Where U_w is the voltage window and v is the scan rate.

4.2.4 DFT calculations

Computational simulation was done by our collaborator, Dr. Xiaoyu Han in Prof. Zheng Xiao Guo's group from UCL Chemistry Department. The related part was rewritten according to the results. DFT calculations were performed based on a projector-augment wave (PAW) pseudopotential, implanted in the Vienna Ab initio Simulation Package (VASP). From Table 1, PBE functional produced larger lattice parameters than LDA functionals for c-WN and ß-W_2N structure, contrast to t-W_2N structure. Compared with experimental data, the PBE functional is more suitable for the description of the W-rich W_2N, while LDA functional is more suitable for WN. For the absorption and desorption of H* on the surface of ß-W_2N structure, newly developed van der Waals correction, optB88-vdW functional, were accomplished[16], which shows improvement on the description of the electronic dispersion, especially for H*.[17] Kohn-Sham orbitals are expanded in a

plane wave basis set with a cut-off energy of 560 eV, which is 40% higher than the default cutoff of N by performing accurate convergence tests. The systems were relaxed until all forces were less than 0.01 eV/Å. The k-points was set to 15 × 15 × 15 for sampling.

4.3 Results and discussion

The synthetic procedure for substrates supported W_2N@C core-shell nanoarrays (CSA) contains two processes in Figure 4.3. At first, WO_{3-x}@C CSA were deposited on the substrates directly by using a mixed solution of $[W(CO)_6]$, acetone and methanol as sources for both tungsten and carbon. The mixture of acetone and methanol solution with low boiling point could accelerate the formation of aerosols by a humidifier. It confirmed that this approach is potentially more efficient for commercialization. The uniform films on hard, soft and porous substrates and similar structure of WO_{3-x}@C CSA nanorods on copper foils, nickel foams and carbon clothes detected by SEM in Figure 4.4 suggested that AACVD is a useful technique for the fabrication of thin films on a variety of substrates.

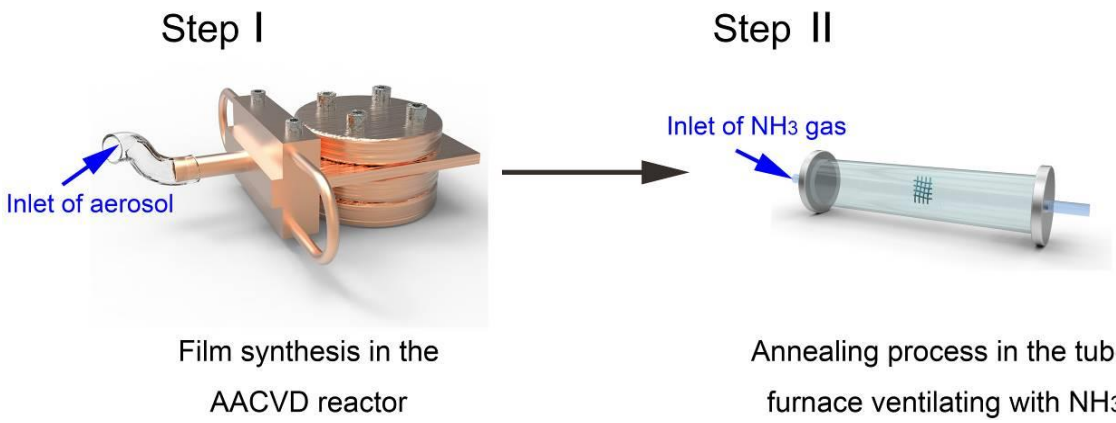

Figure 4. 3 Schematic illustration representing the synthesis of self-standing electrodes.

Then, the as-synthesized WO_{3-x}@C CS/carbon cloth was annealed for 3 hours in a tube furnace under the flow of ammonia gas at 600 ^{o}C. The ramp rate of temperature was controlled at 5 ^{o}C/min for mild ion-exchange without destroying the morphology of nanorod arrays and core-shell structures. The colour of the thin films changed from blue to black after the annealing process.

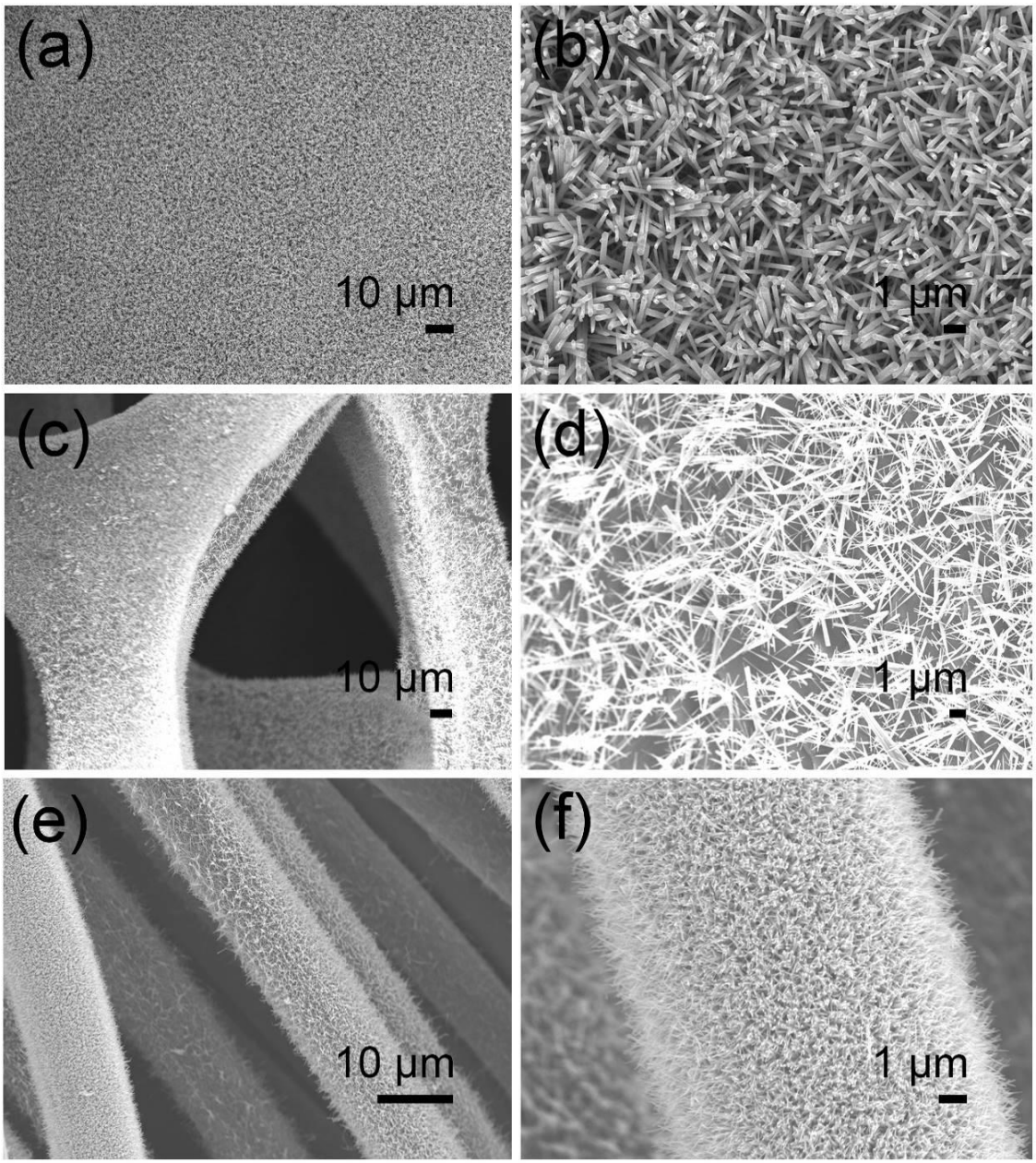

Figure 4. 4 SEM images of WO_{3-x}@C CSA on (a, b) copper foils; (c, d) nickel foams and (e, f) carbon clothes in low- and high-magnification, respectively.

The morphology and microstructures of the W_2N@C/carbon cloth materials was illustrated by scanning electron microscopy (SEM) in Figure 4.5a and b. The W_2N formed as needle-structured nanorod arrays with similar morphology as oxide counterparts. The orderly coated films can be demonstrated from low-magnification SEM images. The detailed nanostructure of W_2N@C arrays are uncovered by high-magnification SEM images in Figure 4.3b. The width of a typical nanorod is 20~30 nm, while the length is more than 1 μm. Figure 4.5c shows transmission electron microscopy (TEM) image of the edge of a W_2N@C nanorod. The thin-layered carbon shell covered the W_2N nanorod uniformly. The simultaneous synthesis of WO_{3-x} and formation of carbon shell during one-step process can be utilized to preserve metal nitrides and further enhance the electrical conductivity of the structures. These morphologies displayed by TEM are almost the same as WO_{3-x}@C nanorods (Figure 4.6a and b), illustrating the annealing in ammonia gas had no disruption for structures of the nanorod and the carbon shell. The high-resolution TEM (HRTEM) image in Figure 4.5d revealed nanostructures and phases of the as-synthesized electrodes, which clearly presented the ~ 3 nm thickness of carbon layer. The identified lattice space of ~ 0.205 nm correspond to the (200) crystal plane of cubic structured W_2N. Moreover, the blue dashed circle can be indexed to amorphous carbon lattices. In order to further elucidate the structural composition of the W_2N@C/carbon cloth, energy dispersive X-ray spectroscopy (EDS) characterization was performed to obtain elemental distribution. EDS spectra disclosed the target element peaks of C, W, N in the electrodes with no other extra peaks detected. Figure 4.5g-i showed the SEM mapping images of the W_2N@C/carbon cloth. The dense blue signals revealed the high tungsten content. Nitrogen elements, signals from red spots, overlapped with tungsten uniformly, suggesting nitrogen was homogeneously distributed in the crystals. Additionally, the carbon was shown in a low intensity, in accordance with thin shell-layers detected from TEM images.

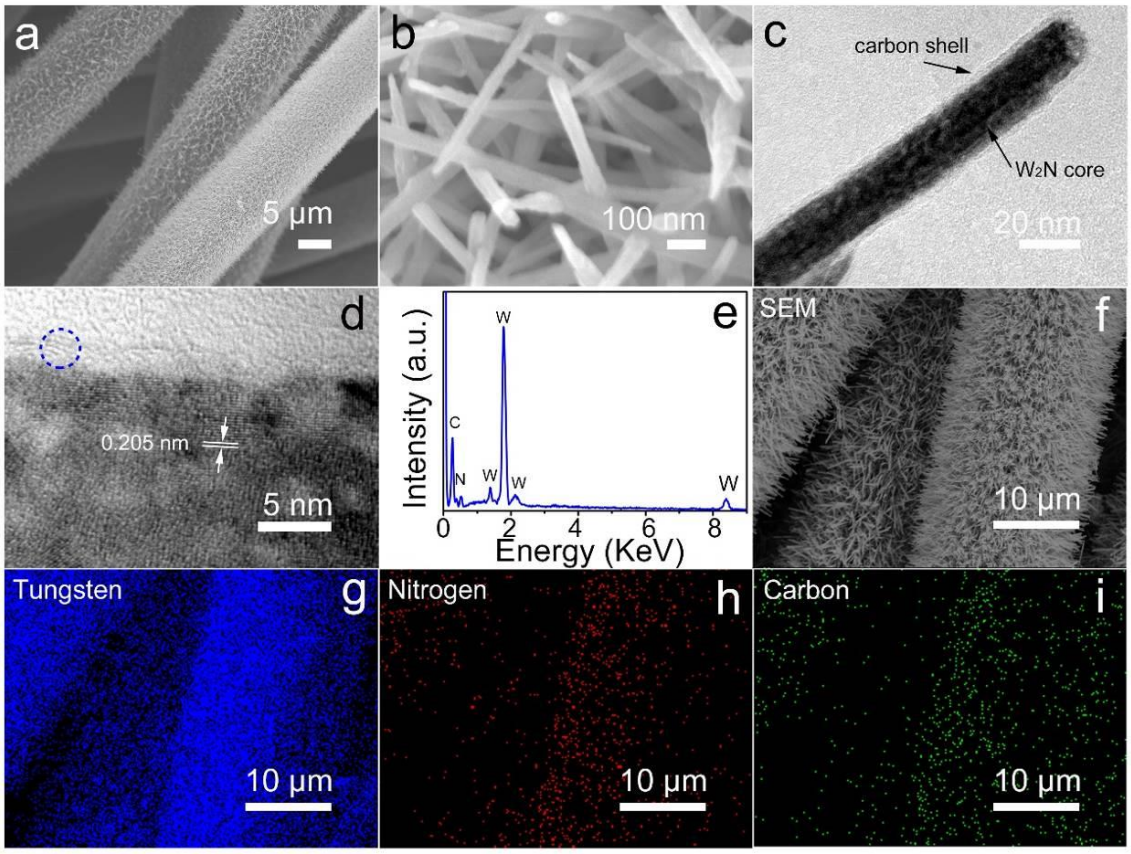

Figure 4. 5 (a), (b) SEM images of W_2N@C/carbon cloth in low and high magnification, respectively; (c) TEM image of the W_2N@C nanorod; (d) HRTEM image of the edge stucture of a representative W_2N@C nanorod; (e) EDS spectrum of the carbon cloth supported W_2N@C detected from SEM image; (f-i) Mapping images of W_2N@C/carbon cloth; (f): its corresponding SEM images; (g): tungsten; (h): nitrogen and (j): carbon elements, respectively.

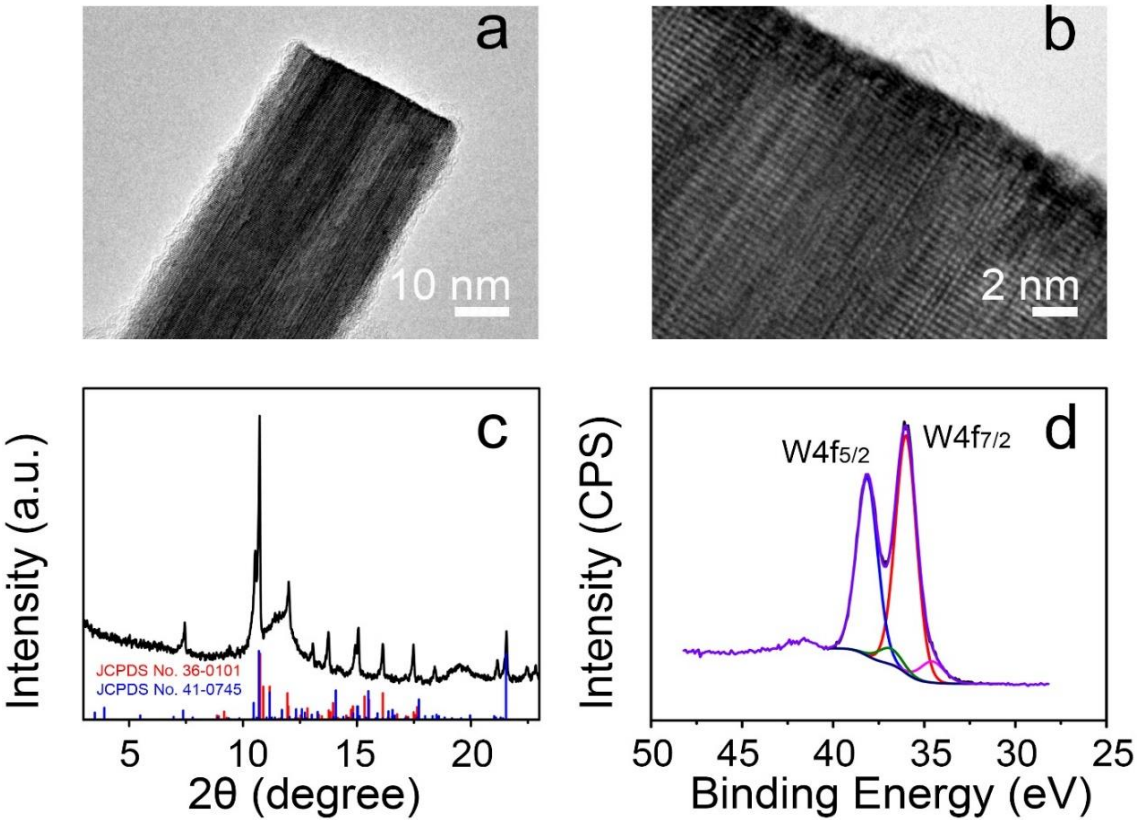

Figure 4. 6 (a, b) TEM image and HRTEM image of the WO_{3-x}@C nanorod, respectively. (c) XRD pattern of WO_{3-x}@C/carbon cloth and its corresponding standard patterns (JCPDS No. 36-0101 and 41-0745) (d) XPS spectrum of the W 4f.

X-ray Diffraction (XRD) investigated phase evolutions of the materials after the annealing step in ammonia. The phases of the synthesized WO_{3-x} (Figure 4.6c) corresponded to the mixed phases of $W_{18}O_{49}$ (JC-PDS No. 36-0101) and W_5O_{14} (JC-PDS No. 41-0745) and the blue colour of films instead of the white one illustated the oxygen vacancy features within the stoichiometric tungsten oxide. After the ammoniation, it is noting that phase-pure W_2N was synthesized successfully and the diffraction peaks of ~ 17.1°, ~ 19.8°, ~ 28.1°, ~ 33.1° and ~ 34.6° corresponded to the cubic W_2N lattice planes of (111), (200), (220), (311) and (222) (JC-PDS No. 25-1257) with no evidence of residual oxides in Figure 4.7a. The peak in the diffraction pattern at ~ 12° from the carbon ultrathin shell and carbon cloth can be observed from both XRD patterns before and after ammoniation. X-ray photoelectron spectroscopy (XPS) analysis showed that the

C-N bonds from C 1s in Figure 4.7b and N 1s in Figure 4.7d spectra, demonstrating the sp^3 and sp^2 hybridized N species doped into the carbon.[18] In comparison with WO_{3-x}@C/carbon cloth in Figure 4.6d, the W 4f spectrum of W_2N (Figure 4.7c) exhibited diverse chemical compositions. The spin orbital peaks of W $4f_{7/2}$ and W $4f_{5/2}$ for W at ~ 33.2 and ~ 35.2 eV are associated with W species in b.c.c W_2N structure. Residual W-O bond similar to that of WO_{3-x} can be detected from W 4f spectrum of W_2N, which is a ordinary phenomenon for metal nitrides and formed by oxygen contamination on the surface.[19] Moreover, the peak at ~ 396 eV from N 1s in Figure 4.7d suggest the W-N from metal nitrides.

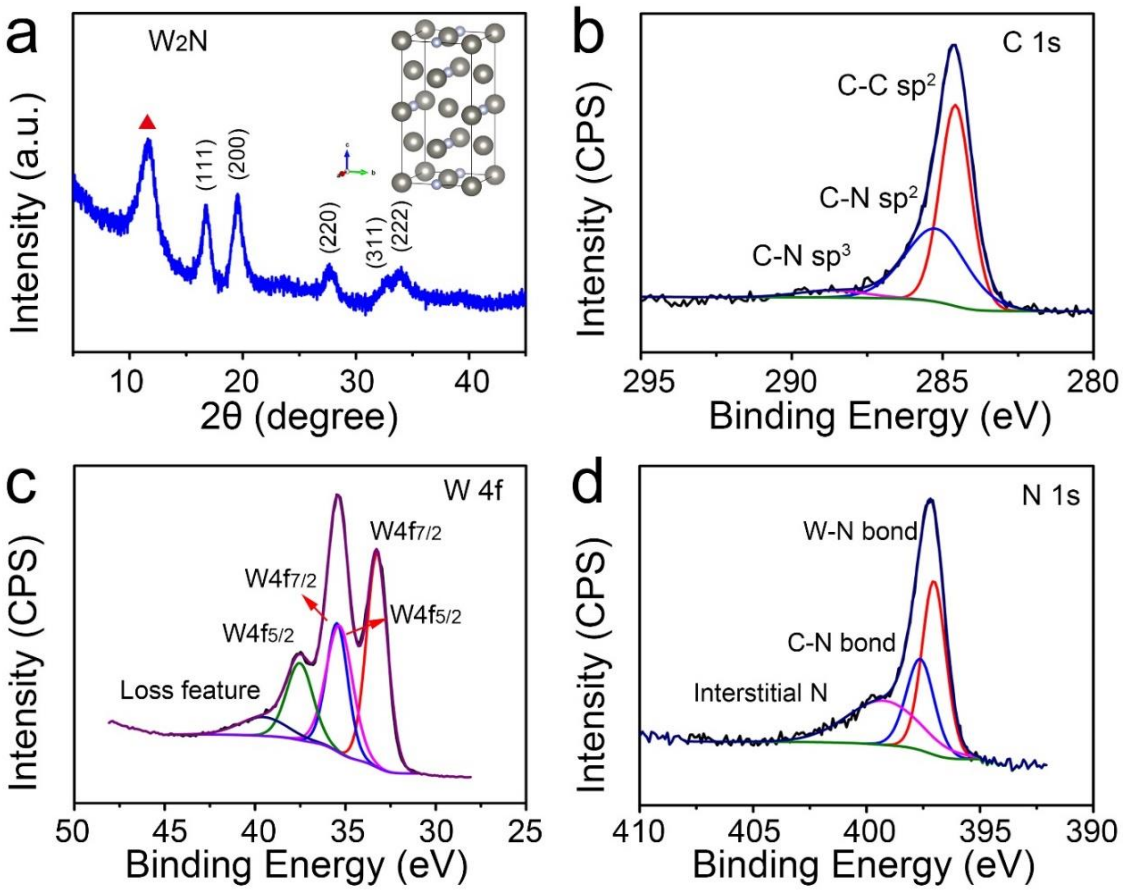

Figure 4. 7 (a) X-ray Diffraction (XRD) pattern of carbon cloth supported W_2N@C. The red triangle showing the peaks from the carbon substrate, inset in (a): the crystal structure of cubic W_2N, large ball: tungsten atoms, small ball: nitrogen atoms; X-ray photoelectron spectroscopy (XPS) spectra of (b) C 1s; (c) W 4f; and (d) N 1s.

To assess the electrochemical capacitive performance of self-standing W_2N@C/carbon cloth, the as-fabricated electrodes were evaluated in a three-electrode configuration directly using 2 M H_2SO_4 solution as the electrolyte. To optimize the energy storage properties of the materials, different volumes of the precursor solutions were firstly prepared to control the loading amount of W_2N@C on carbon cloth substrates. Figure 4.8a shows the rate performance of the W_2N@C/carbon cloth obtained from different volumes of precursor solution, calculated from the cyclic voltammetry (CV) curves of at least three individual electrodes. At the low scan rate of 5 mV s^{-1}, the areal capacitance improves with the increased loading amount of the active species. The highest areal capacitance of 752.3 mF cm^{-2} could be realized at 25 mL of precursor solution. However, the high loading amount of the W_2N@C on carbon cloth prohibited the utilized surface areas and porous structures for mass transfer thus reducing the electrochemical capacitive storage especially at high scan rates. Compared with other amounts of the precursor solution, the one with 20 mL delivered the best rate properties. It realized average areal capacitances of 693.0, 598.9, 519.7, 469.8, 436.2 and 410.0 mF cm^{-2} at scan rates of 5, 10, 20, 30, 40 and 50 mV s^{-1}, respectively, showing the highest specific capacitance at almost all scan rates. Therefore, 20 mL of precursor solutions was utilized as the optimized volume for synthesis. Compared with the capacitive performance before (WO_{3-x}@C) and after (W_2N@C) annealing process by galvanostatic charge-discharge (GCD) tests in Figure 4.8b, W_2N@C/carbon cloth electrodes showed nearly linear GCD curves for surface-controlled energy storage and longer discharge time, which demonstrate it possessed higher specific capacitance, in line with the larger enclosed area of the W_2N@C from CV curves in Figure 4.8c. In addition, the CV curves varied from the “dolphin-like” shape to a rectangular one after the ammoniation treatment. The notable pairs of the redox peaks can be identified for W_2N@C/carbon cloth electrodes at 0.05 and 0.45 V during oxidation process and 0 and 0.39 V for reduction, respectively. Nevertheless, nearly undetected CV peaks are observed for WO_{3-x}@C electrodes, which is a normal character for

various types of tungsten oxide analogues. This is as a result of the tortuous ion-diffusion within the lattice/surface of oxide counterparts.[20] Furthermore, the potential discrepancy of anodic and cathodic peaks can illustrate the reversibility of electrochemical redox reactions. The value of potential discrepancy for W_2N@C/carbon cloth electrodes is ~ 0.05 V, less than that of reported tungsten oxide electrodes [5, 8-10, 20], demonstrating its reversibility of redox reactions. Therefore, the capacitive behaviours of W_2N materials could be contributed from both electrical double-layer capacitance and pseudocapacitance. The possible Faradaic reactions can be described as: $W_2N + \alpha H^+ + \alpha e^- \leftrightarrow H_\alpha W_2N$. The inherent resistance and the ion-mobility of these two electrodes were further evaluated by EIS spectra. The equivalent series resistance (R_s), composing of inherent resistances of active materials, bulk resistance of the electrolyte and contact resistance of the interface between electrolyte and electrodes, are 0.542 and 0.588 Ω for the W_2N@C/carbon cloth and WO_{3-x}@C/carbon cloth electrodes, respectively. The charge transfer resistance (R_{ct}), revealing the ability of electrodes for diffusion of electrons, are 0.12 and 0.133 Ω for W_2N@C/carbon cloth and WO_{3-x}@C/carbon cloth electrodes, respectively. The relatively small resistance value and the negligible discrepancy between two electrodes validated the fact that coated carbon layers improve the electrical conductivity of the whole structure. To further clarify the enhanced electrochemical energy storage properties of the tungsten nitrides as electrode materials for supercapacitor applications in comparison with the oxide counterparts, *in-situ* electrical properties from transmission electron microscopy-scanning tunneling microscopy (TEM-STM) measurements of the individual W_2N and WO_{3-x} nanorod were investigated and compared. The experiment was conducted within a 200 kV high-resolution TEM with beam-blank irradiation at low illumination and similar to our previous work.[21]

The Schottky contact between nanorods and probes were observed from the I-V curve when a bias was applied in Figure 4.8e. The current changes from -96 to 84 μA with the voltage range of -5.0 to 5.0 V. The resistance can be predicted as $5.56 \times 10^4\ \Omega$ for a single W_2N nanorod; as a contrast, the current varies from -1.6 to 1.4 μA at the same potential range of an individual WO_{3-x} nanorod, which shows a resistance of $3.33 \times 10^6\ \Omega$. The result confirmed that the electrical conductivity of the W_2N nanorod was ~ 2 magnitudes higher than that of WO_{3-x} nanorods and 5-7 magnitudes better than other reported transition metal oxides.[22,23] To prove the effect of the carbon coating on the metal nitride electrodes, a long-term cycling CV tests at a scan rate of 50 mV s^{-1} was compared between carbon cloth supported W_2N@C and W_2N, respectively. As shown in Figure 4f, a capacitance retention was ~ 91 % for W_2N@C CSA/carbon cloth electrodes after 20,000 cycles, better than that of ~ 81.3 % for W_2N/carbon cloth in 5,000 cycles. The inset in Figure 4.8f shows the TEM images of the W_2N@C nanorod after stability test. The rougher surface of nanorods was observed after the long-term redox reactions but still covered by the carbon coating layers, keeping the integrated nanostructures of the electrodes. Thus, an increased capacitance after several cycles may be due to the further activation of the etched surface process. The results illustrates the improved cycling and structural stability as a result of surface carbon layers. The as-synthesized W_2N@C CSA/carbon cloth is among the best tungsten materials and other transition metal nitrides for electrodes in supercapacitors and delivers one of the highest areal capacitances ever reported, as shown in Table 4.1.

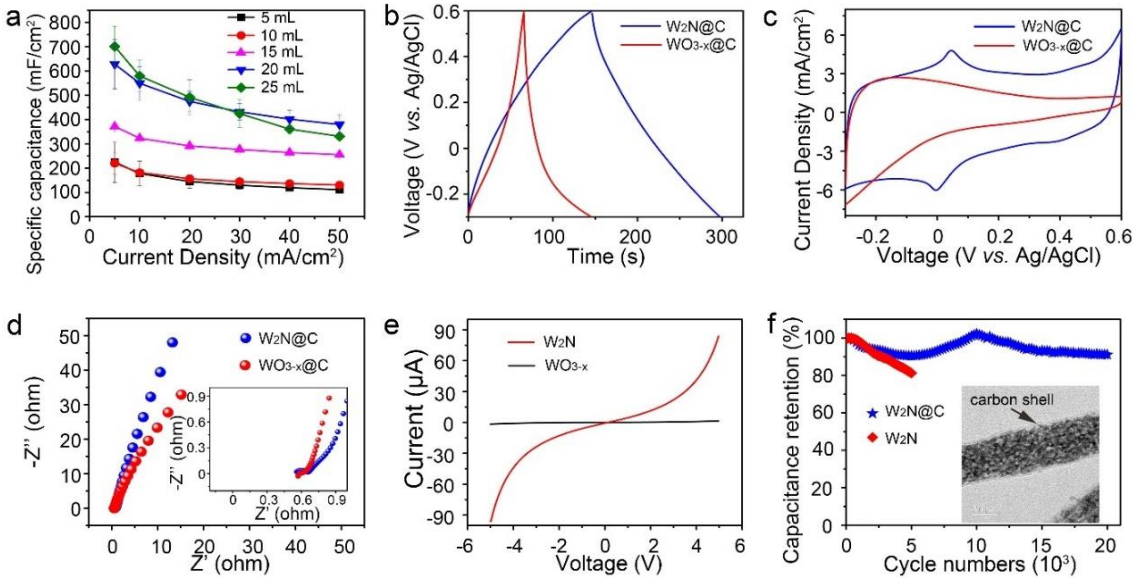

Figure 4. 8 (a) Rate performances of carbon cloth supported W_2N@C electrodes obtained from different amount of precursor solutions; (b) Galvanostatic charge-discharge (GCD) at an areal current density of 3 mA/cm^2; (c) cyclic voltammetry (CV) at the scan rate of 5 mV/s and (d) electrochemical impedance spectra (EIS) curves of carbon cloth supported W_2N@C and WO_{3-x}@C respectively, inset in (d) showing the high frequency range of the spectra; (e) I-V curves detected by *in-situ* TEM for a single W_2N and WO_{3-x} nanorod, respectively; (f) Stability test of W_2N@C/carbon cloth and W_2N/carbon cloth performed from cyclic CV tests, the inset showing the TEM images of W_2N@C after cycling tests.

Table 4. 1 Summary of representative electrochemical performances of tungstate-based materials and other metal nitride electrodes.

Electrodes	Specific capacitance	Mass Loading	Rate performance	Stability	Reference
W_2N@C/carbon cloth	693 mF cm^{-2} CV at 5 mV s^{-1}	~ 3.5 mg/cm^2	78 % retention 10 times scan rate increase*	91 % retention 20000 CV cycles	This work
Ag nanowire/WO_3	13.6 mF cm^{-2} CV at 10 mV s^{-1}	~ 0.1 mg/cm^2 for WO_3	____	72.6 % retention 5000 CV cycles	[24]
WO_3/Ti foam	652 mF cm^{-2} CV at 10 mV s^{-1}	~ 4.0 mg/cm^2	70 % retention 10 times scan rate increase	85 % retention 5000 CV cycles	[9]
h-WO_3/SWCNTs	490.2 mF cm^{-2}	~ 2.0 mg/cm^2	42.3 % retention	87 % retention	[25]

	CV at 2 mV s^{-1}		25 times scan rate increase	5000 CV cycles	
WO_{3-x}/MoO_{3-x}/carbon fabric	~ 500 mF cm^{-2} CD at 2 mA cm^{-2}	~ 3.0 mg/cm^2	~ 35 % retention 15 times current density increase	____	[8]
WO_3 quantum dots	~ 136 mF cm^{-2} CD at 0.2 mA	____	~ 60 % retention 40 times current density increase	____	[18]
WO_{3-x}/porous carbon	~ 125 F cm^{-3} CV at 2 mV s^{-1}	____	77 % retention 10 times scan rate increase	~ 100 % 1000 CD cycles	[26]
TiN@GNS/carbon fiber	~ 180 F g^{-1} mV s^{-1}	< 1 mg/cm^2	80 % rerention 10 times scan rate increase	____	[27]
2D Metallic MoN	~ 278.4 mF cm^{-2} at 2 mV s^{-1}	~ 6.6-9 mg/cm^2	21 % retention 10000 times scan rate increase	~ 95 % retention after 25000 cycles	[28]
molybdenum nitride	~ 275 F g^{-1} at 2 mV s^{-1}	_____	30 % retention 50 times scan rate increase	~ 95 % retention after 1000 cycles	[29]
VN	~ 28 mF cm^{-2} at 2 mV s^{-1}	0.1 mg/cm^2	42 % retention 100 times scan rate increase	_____	[30]
TiVN films	15 mF cm^{-2} at 2 mV s^{-1}	_____	10 % retention 10 times scan rate increase	~ 99 % retention after 10000 cycles	[31]
$Ni_xCo_{2x}(OH)_{6x}$/TiN Nanotube	2543 F g^{-1} at 5mV s^{-1}	____	~ 26 retention 100 times scan rate increase	~ 94 % retention after 5000 cycles	[32, 33]
MnO_2/TiN NTA	681 F g^{-1} at 2 A g^{-1}	0.7 mg/cm^2	55 % retention 1000 times scan rate increase	~ 97 % retention after 1000 cycles	[33, 34]

*Best rate performance sample was shown here.

To further elucidate the capacitive behaviours of the cubic W_2N and oxide counterparts, the computational simulation of the H^* redox reaction on (200) surface of W_2N and (010) surface of $W_{18}O_{49}$ were conducted by density functional theory, implanted in the Vienna ab-initio Package (VASP).[35] The comparison of different functionals and computational settings, including projector augmented wave (PAW) [36] and PBE functional [37, 38] were described in detail in the experimental sections.

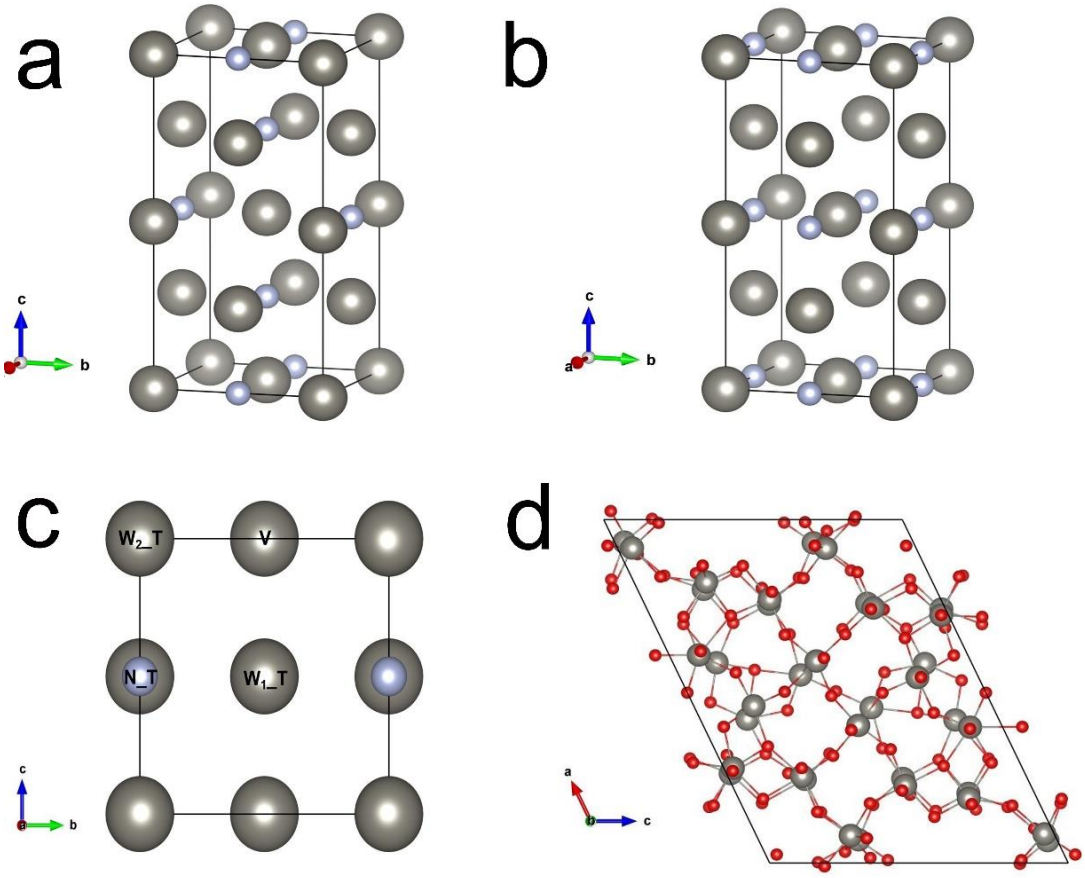

Figure 4. 9 The possible cubic structures of W_2N: ß-W_2N (a) and t-W_2N (b); (c) The top view of (200) surface for cubic W_2N. The W atoms directly above the N atom are noted as W_1, the ones without N atom are W_2; The top and vacancy sites are shortened as T and V, respectively; The grey and light purple balls stand for W and N atoms, respectively; (d) The top view of relaxed (010) surface of $W_{18}O_{49}$. The grey and red balls are W and O atoms, respectively.

In the case of WN_x system, when x<1, two main phases could be formed: tungsten mononitride WN including hexagonal h-WN at low and cubic c-WN at high temperature, and tungsten sub-nitride W_2N.[39] Previous study on deposition of tungsten nitride thin films indicated that WN or other WN_x (x>1) phases would require bias assistance or other non-equilibrium film growth processes.[40] The high formation energy of WN suggested it delivers the metastable phase, which is in line with the experimental observation. The former phases were investigated and reported widely; [41-45] however, few theoretical works are related to the cubic W_2N. [46-48] As for W_2N derived from the c-WN $Fm\bar{3}m$ crystals, two feasible structures, *i.e.* ß-W_2N and t-W_2N, could be proposed and shown in Figure 4.9a and b. On the basis of the c-WN structure, both share the same positions for W atoms, while 50 % vacancy of N atoms occupy at different sites. The formation energies of the two structures were compared and calculated by the equation below:

$$E_f = E_{W_2N} - nE_W - \frac{1}{2}nE_{N_2} \qquad (4.6)$$

where E_{W_2N} represents the chemical energy of ß-/t-W_2N; n represents the numbers of W in the system, E_W and E_{N_2} are the chemical energy of W in bulk tungsten and N in N_2, respectively. As shown in Table 4.2, both ß- and /t-W_2N exhibit relatively low formation energy compared with c-WN, which illustrated that both structures are stable in WN_x system. While the ß-W_2N is more energetically favourable than t-W_2N. Thus, ß-W_2N structure is used for the following calculations.

Table 4. 2 Comparison of the formation energies, lattice parameters in different functionals and the experimental data.

	PBE			LDA			Experiments
	Formation energy (eV)	Lattice parameters		Formation energy (eV)	Lattice parameters		lattice parameters
		a	c		a	c	a
WN	1.18	4.367	N/A	1.12	4.358	N/A	4.13 [49]

ß-W_2N	-1.54	4.085	8.170	-1.59	4.076	8.153	4.126
t-W_2N	-1.13	4.089	N/A	-1.19	4.209	N/A	

The $2 \times 1 \times 1$ and $1 \times 2 \times 1$ supercells were chosen for the study of H^* adsorption/desorption in W_2N (200) and $W_{18}O_{49}$ (010) slabs (Figure 4.8c and d). To prevent periodic interactions, a 10 Å vacuum slab was added to the systems. The atoms in bottom two layers were kept fixed during the calculations, while other atoms including the reactant H are fully relaxed. The k-point samplings were reduced to 15×15×1 and Gamma point only for W_2N and $W_{18}O_{49}$, respectively. The adsorption energy was defined according to:

$$E_{ad} = E_{total} - E_{slab*} - \frac{1}{2}E_{H_2} \qquad (4.7)$$

where E_{ad} stands for the adsorption energy; E_{total} is the total energy in the system; E_{slab*} and E_{H2} are the chemical energy of W_2N (200) or $W_{18}O_{49}$ (010) slabs and the chemical energy of H_2, respectively. From the top view of the W_2N (200) surfaces, four different possible adsorption sites can be detected in Figure 4.8c. To differentiate different surface W atoms as active sites, W atoms with and without N atom below them are labelled as W_1 and W_2, respectively. The T and V represent the top and vacancy sites, respectively.

Table 4. 3 The H^* adsorption energy (eV) at different active sites and H-W/N distance (Å) on different sites of W_2N (200) surfaces.

	W_1_T	W_2_T	N_T	V
E_{ad} (eV)	-0.50	-0.06	0.17	0.39
distance (Å)	1.74	1.77	1.03	2.25

As shown in Table 4.3, the H^* tends to bond with surface tungsten *via* physical adsorption. The W_1 and W_2 are the top two easiest sites with exothermic reactions during formating interactions among H^* and materials. The physical adsorptions are beneficial for H^* association with active sites in the redox reactions. Compared with unfavourable bonding sites with H^* such as N and V, the W_2N

surface delivered more dynamically active sites. Therefore, ß-W_2N structure is not only an energetically stable structure, it also provides a W-rich surface for absorption of H^*. In addition, the diverse range of the valence states of surface W atoms offer the hosts the ability for multi-adsorption of H^*.[50] To elucidate the energy barrier of the H^* diffusion on the W_2N (200) surfaces, the climbing image nudged elastic band (Ci-NEB) method was carried out.[51] The results indicate that the energy barrier within surfaces is relatively huge, which is strong enough to hinder further diffusion of H^*. Consequently, redox reactions between H^* species and electrodes happened only at individual sites without additionally H^* diffusion on the surface.

Nevertheless, the relaxed structure presented a significant distortion for the $W_{18}O_{49}$ (010) surfaces. In this system, the $W_{18}O_{49}$ surface is much more disordered, the dangling O on the surfaces could induce strong bonding sites for H^* due to the adsorption energy of ~ 2eV, which leads to proton passivation of the $W_{18}O_{49}$ (010) surface. The H passivation is indexed to the “dolphin-like” shape CV curve in Figure 4.6c. The formed covalent bonds between H passivition and dangling O are too strong for the H^* to continue reversible redox reactions. Therefore, H passivated $W_{18}O_{49}$ (010) surface will be the next reactant for further reversible redox reaction. However, additional absorption of H^* will not be easy due to the relatively weak bond formation.

A flexible asymmetric supercapacitor device (FASD) was fabricated by using the W_2N@C/carbon cloth as an anode and commercial nitrogen doped graphene (morphology in Figure 4.10a) on carbon paper as the cathode for assessing practical applications of as-designed W_2N@C/carbon cloth electrodes. The redox peaks for NG in Figure 4.10b is common for nitrogen doped carbon materials as the pseudocapacitor electrodes. The GCD tests at the different current densities revealed the excellent rate performances of NG in Figure 4.10c, and the capacitance of the 1000^{th} cycle is higher than the initial one, suggesting the

activation of the materials and in accordance with the EIS results in Figure 4.10d. The capacitance of the W_2N@C/carbon cloth anode and NG cathode was balanced according to $Q_+ = Q_-$.

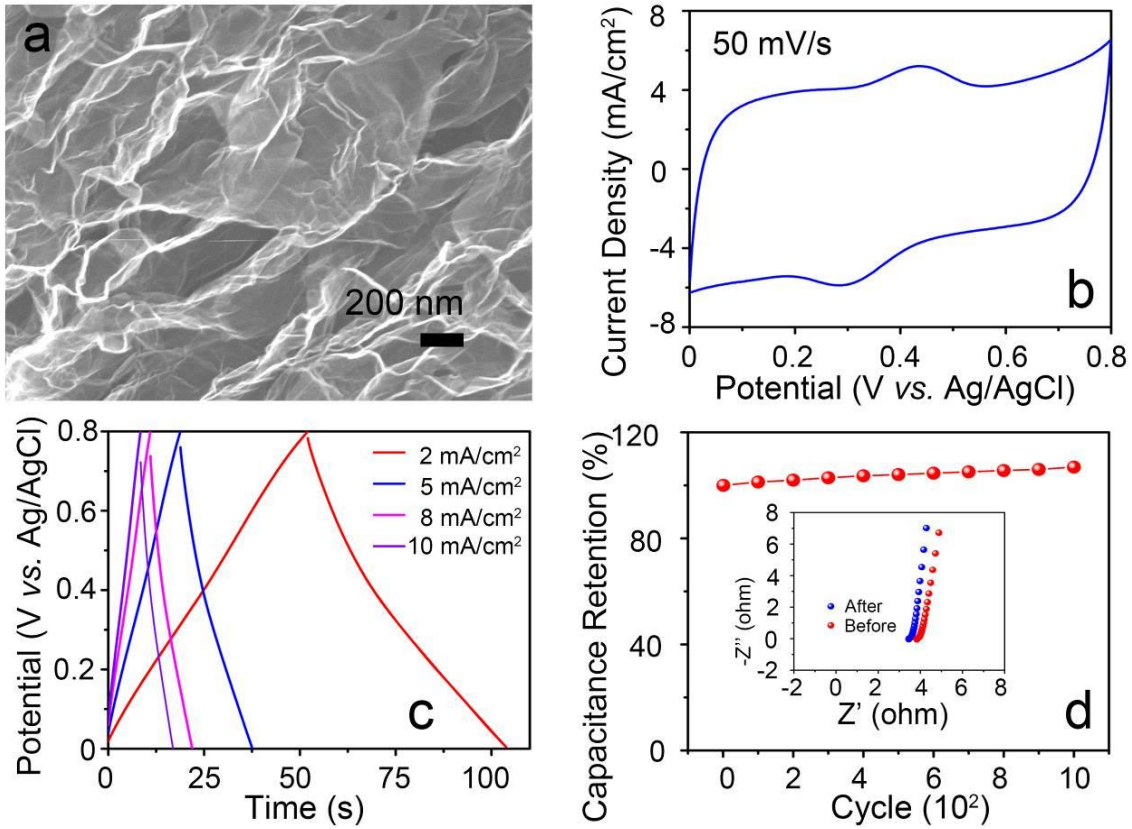

Figure 4. 10 (a) SEM image of the commercial nitrogen doped graphene (NG); (b) CV test of the NG on carbon paper at the scan rate of 50 mV s^{-1} in 2 M H_2SO_4; (c) GCD tests of the NG at different current densities; (Loading mass density: 0.5 mg/cm^2) (d) Stability test of the NG in the continues CV tests for 1000 cycles and inset showing the EIS spectra before and after the cycling CV scans.

As for the gravimetric capacitance, the W_2N@C/carbon cloth processed specific capacitance of 236 F g^{-1} at the scan rate of 50 mV s^{-1}, and NG/carbon paper exhibited the specific capacitance of 225 F g^{-1}. According to $Q_+ = Q_-$:

$$Q = C_m \times m \times \Delta E \quad (4.8)$$

$$\frac{m_{W_2N}}{m_{carbon}} = \frac{225\times0.8}{236\times0.9} = 1:1.18 \quad (4.9)$$

The mass ratio of two electrodes is calculated as ~ 1:1.18. The mass loading of W_2N@C/carbon cloth is ~ 3.2 mg/cm^2, thus the mass density of NG is coated as ~ 3.8 mg/cm^2 on carbon paper for device fabrication.

The CV curves in Figure 4.11a of the FASD suggests that the as-fabricated FASD worked well up to a voltage range of 1.6 V. The shape of the CV curves deviates from the rectangular shape and the unapparent redox peaks indicating that both pseudocapacitance and electrical double-layer capacitance (EDLC) contributed to the total asymmetric capacitance. To eliminate side reactions, especially oxygen evolution reactions, GCD tests were characterized within the voltage window of 1.2 V at different current densities as shown in Figure 4.11b. The superb specific capacitance was calculated as ~ 180 mF/cm^2 at 1 mA/cm^2. It is noted that a high rate performance of ~ 85.5 % capacitance was retained when the current density was increased 10 times. With the aim of realizing large working voltage range applications, symmetric devices (SD) were manufactured by using W_2N@C/carbon cloth in ionic liquid electrolyte within coin cell configurations. The near rectangular and revesible shape of CV in Figure 4.11c even at a fast scan rate of 1000 mV s^{-1} indicated high rate capability of the devices. The cycling performances were performed by 5000 cyclic CV tests at a high scan rate of 100 mV s^{-1} in Figure 4.11d. The capacitance retention of 83.3 %, indicating the superb cycling stability of the ionic liquid electrolyte based SD, which is also reflected by limited difference of the area in CV curves between the first and final cycles.

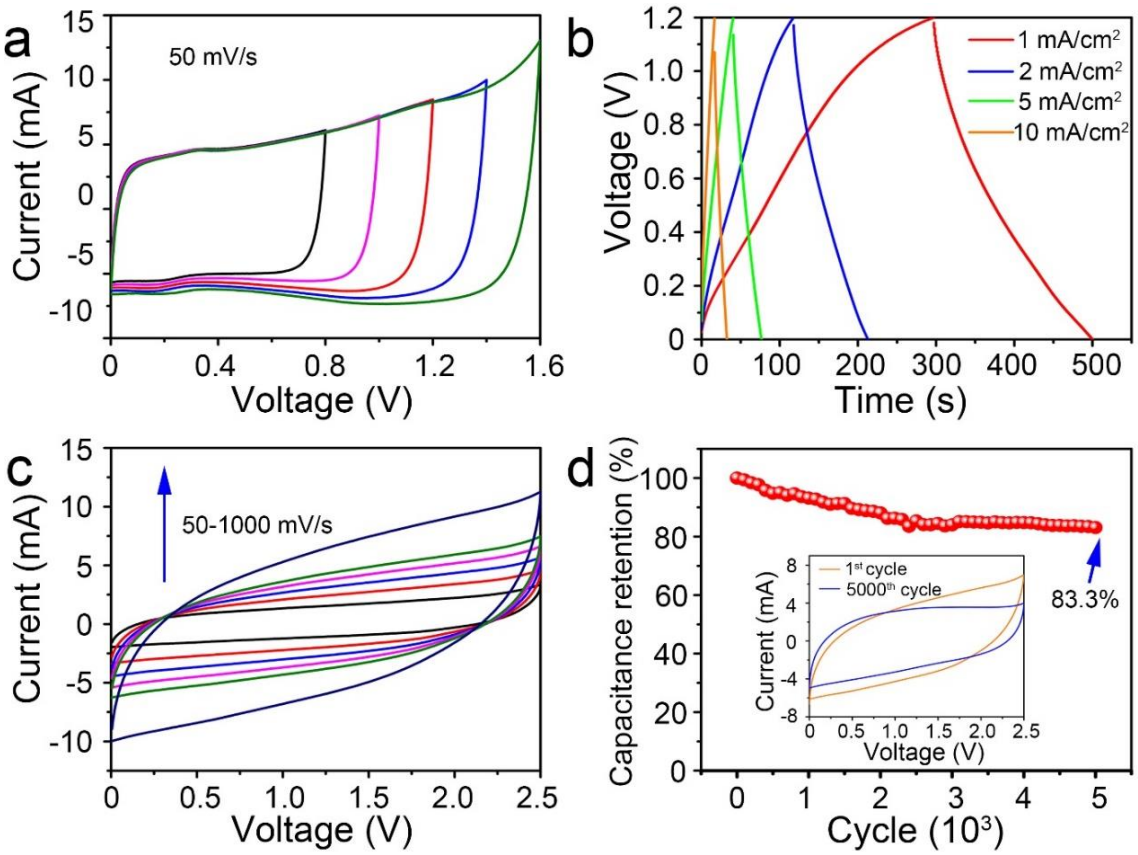

Figure 4. 11 (a) CV curves of a flexible asymmetric supercapacitor device (FASD); (b) GCD test of the FASD in the voltage range of 1.2 V; (c) CV tests of the ionic liquid-based electrolyte for symmetric devices (SD); (d) Cycling stability of the SSD at a CV scan rate of 100 mV s^{-1}.

4.4 Conclusions

In this chapter, an easily ready-to-industry approach by combining AACVD and ammoniation process was develop to fabricate self-standing electrodes for bendable supercapacitors. The carbon cloth was introduced as the flexible current collectors from this chapter to support W_2N@C active materials. The as-designed electrodes are among the highest areal capacitances of tungsten-based electrodes with excellent rate capability and long-term stability for the single electrode evaluation. Moreover, the merits of tungsten nitride materials over the oxide counterparts for use as electrodes were confirmed by a combined electrochemical analysis, *in-situ* electrical property test within TEM-STM and

computational caculation approach. The pratical applications of supercapacitors were confirmed by assembled flexible device and coin cells. This chapter provides insights and attracts research interests for exploring metal nitride materials in energy storage and conversion and designing of hierarchical nanostructure based on the electrically conductive self-standing electrodes. In Chapter 5, by integration of the carbon cloth-based electrode fabrication technique and nanostructure design strategies, the validation of the flexible electrodes were expanded and proved for Li-ion battery electrodes.

4.5 References

[1] V. Augustyn, P. Simon, B. Dunn, *Energy Environ. Sci.* **2014**, *7*, 1597.

[2] L. Deng, J. Wang, G. Zhu, L. Kang, Z. Hao, Z. Lei, Z. Yang, Z.-H. Liu, *J. Power Sources* **2014**, *248*, 407.

[3] W. Sugimoto, H. Iwata, Y. Yasunaga, Y. Murakami, Y. Takasu, *Angew. Chem. Int. Ed. Engl.* **2003**, *42*, 4092.

[4] H. Jiang, J. Ma, C. Li, *Adv. Mater.* **2012**, *24*, 4197.

[5] Z. Chen, Y. Peng, F. Liu, Z. Le, J. Zhu, G. Shen, D. Zhang, M. Wen, S. Xiao, C.-P. Liu, Y. Lu, H. Li, *Nano Lett.* **2015**, *15*, 6802.

[6] C. Zhu, P. Yang, D. Chao, X. Wang, X. Zhang, S. Chen, B. K. Tay, H. Huang, H. Zhang, W. Mai, H. J. Fan, *Adv. Mater.* **2015**, *27*, 4566.

[7] V. Chakrapani, J. Thangala, M. K. Sunkara, *Int. J. Hydrogen Energ.* **2009**, *34*, 9050.

[8] X. Xiao, T. Ding, L. Yuan, Y. Shen, Q. Zhong, X. Zhang, Y. Cao, B. Hu, T. Zhai, L. Gong, J. Chen, Y. Tong, J. Zhou, Z. L. Wang, *Adv. Energy Mater.* **2012**, *2*, 1328.

[9] M. Qiu, P. Sun, L. Shen, K. Wang, S. Song, X. Yu, S. Tan, C. Zhao, W. Mai, *J. Mater. Chem. A* **2016**, *4*, 7266.

[10] Y.-H. Wang, C.-C. Wang, W.-Y. Cheng, S.-Y. Lu, *Carbon* **2014**, *69*, 287.

[11] D. K. Nandi, U. K. Sen, S. Sinha, A. Dhara, S. Mitra, S. K. Sarkar, *Phys.*

Chem. Chem. Phys. **2015**, *17*, 17445.

[12] P. Huang, C. Lethien, S. Pinaud, K. Brousse, R. Laloo, V. Turq, M. Respaud, A. Demortiere, B. Daffos, P. L. Taberna, B. Chaudret, Y. Gogotsi, P. Simon, *Science* **2016**, *351*, 691.

[13] G. He, J. Li, W. Li, B. Li, N. Noor, K. Xu, J. Hu, I. P. Parkin, *J. Mater. Chem. A* **2015**, *3*, 14272.

[14] M. Ling, C. Blackman, *Phys. Status Solidi C* **2015**, *12*, 869.

[15] S. Vallejos, P. Umek, T. Stoycheva, F. Annanouch, E. Llobet, X. Correig, P. De Marco, C. Bittencourt, C. Blackman, *Adv. Funct. Mater.* **2013**, *23*, 1313.

[16] J. Klimeš, D. R. Bowler, A. Michaelides, *J. Phys.: Cond. Matt.* **2010**, *22*, 022201.

[17] J. Klimeš, D. R. Bowler, A. Michaelides, *Phys. Rev. B* **2011**, *83*, 195131.

[18] G. He, M. Qiao, W. Li, Y. Lu, T. Zhao, R. Zou, B. Li, J. A. Darr, J. Hu, M.-M. Titirici, I. P. Parkin, *Adv. Sci.* **2016**, *4*, 1600214.

[19] Y. G. Shen, Y. W. Mai, *Surf. Coat. Technol.* **2000**, *127*, 239.

[20] S. Cong, Y. Tian, Q. Li, Z. Zhao, F. Geng, *Adv. Mater.* **2014**, *26*, 4260.

[21] R. Zou, K. Xu, T. Wang, G. He, Q. Liu, X. Liu, Z. Zhang, J. Hu, *J. Mater. Chem. A* **2013**, *1*, 8560.

[22] R. Zou, Z. Zhang, Q. Tian, G. Ma, G. Song, Z. Chen, J. Hu, *Small* **2011**, *7*, 3377.

[23] Q. Liu, R. Zou, Y. Bando, D. Golberg, J. Hu, *Prog. Mater. Sci.* **2015**, *70*, 1.

[24] L. Shen, L. Du, S. Tan, Z. Zang, C. Zhao, W. Mai, *Chem. Commun. (Camb.)* **2016**, *52*, 6296.

[25] W. Sun, M. T. Yeung, A. T. Lech, C. W. Lin, C. Lee, T. Li, X. Duan, J. Zhou, R. B. Kaner, *Nano Lett.* **2015**, *15*, 4834.

[26] Y. Zhou, S. Ko, C. W. Lee, S. G. Pyo, S.-K. Kim, S. Yoon, *J. Power Sources* **2013**, *244*, 777.

[27] C. Zhu, P. Yang, D. Chao, X. Wang, X. Zhang, S. Chen, B. K. Tay, H. Huang, H. Zhang, W. Mai, H. J. Fan, *Adv. Mater.* **2015**, *27*, 4566.

[28] X. Xiao, H. Yu, H. Jin, M. Wu, Y. Fang, J. Sun, Z. Hu, T. Li, J. Wu, L. Huang, Y. Gogotsi, J. Zhou, *ACS Nano* **2017**, *11*, 2180.

[29] S. I. U. Shah, A. L. Hector, J. R. Owen, *J. Power Sources* **2014**, *266*, 456.

[30] P. J. Hanumantha, M. Kanchan Datta, K. Kadakia, C. Okoli, P. Patel, P. N. Kumta, *Electrochim. Acta* **2016**, *207*, 37.

[31] A. Achour, R. Lucio-Porto, M. Chaker, A. Arman, A. Ahmadpourian, M.A. Soussou, M. Boujtita, L. Le Brizoual, M.A. Djouadi, T. Brousse, *Electrochem. Commun.* **2017**, *77*, 40.

[32] C. Shang, S. Dong, S. Wang, D. Xiao, P. Han, X. Wang, L. Gu, G. Cui, *ACS Nano* **2013**, *7*, 5430.

[33] Y. Zhong, X. Xia, F. Shi, J. Zhan, J. Tu, H. J. Fan, *Adv. Sci.* **2016**, *3*, 1500286.

[34] S. Dong, X. Chen, L. Gu, X. Zhou, L. Li, Z. Liu, P. Han, H. Xu, J. Yao, H. Wang, X. Zhang, C. Shang, G. Cui, L, Chen, *Energy Environ. Sci.* **2011**, *4*, 3502.

[35] G. Kresse, J. Furthemüller, *Comput. Mat. Sci.* **1996**, *6*, 15.

[36] P. E. Blochl, *Phys. Rev. B* **1994**, *50*, 17953.

[37] J. P. Perdew, K. Burke, M. Ernzerhof, *Phys. Rev. Lett.* **1996**, *77*, 3865.

[38] J. P. Perdew, K. Burke, M. Ernzerhof, *Phys. Rev. Lett.* **1997**, *78*, 1396.

[39] H. J. Goldschmidt, *Interstitial Alloy (London: Butterworths)* **1967**, *225*.

[40] C. C. Baker, S. I. Shah, *J. Vac. Sci. Technol. A* **2002**, *20*, 1699.

[41] A. Y. Liu, R. M. Wentzcovitch, M. L. Cohen, *Phys. Rev. B* **1988**, *38*, 9483.

[42] D. V. Suetin, I. R. Shein, A. L. Ivanovskii, *Phys. Stat. Sol. B* **2008**, *245*, 1590.

[43] M. Kavitha, G. Sudha Priyanga, R. Rajeswarapalanichamy, K. Lykutti, *J. Phys. Chem. Solids* **2015**, *77*, 38.

[44] E. I. Isaev, S. I. Simak, I. A. Abrikosov, R. Ahuja, Yu. Kh. Vekilov, M. I. Katsnelson, A. I. Lichtenstein, B. Johansson, *J. Appl. Phys.* **2016**, *101*, 123519.

[45] K. Balasubramanian, S. Khare, D. Gall, *Phys. Rev. B* **2016**, *94*, 174111.

[46] D. V. Suetin, I. R. Shein, A. L. Ivanovskii, *J. Struct. Chem.* **2010**, *51*, 199.

[47] M. J. Mehl, D. Finkenstadt, C. Dane, G. L. W. Hart, S. Curtarolo, *Phys. Rev. B* **2015**, *91*, 184110.

[48] L. Zhou, F. F. Klimashin, D. Holec, P. H. Mayrhofer, *Scr. Mater.* **2016**, *123*, 34.

[49] B. K. Vainshtein, *Pergamon Press 1964*, 334.

[50] S. A. Shevlin, Z. X. Guo, *J. Phys. Chem. C* **2008**, *112*, 17456.

[51] G. Henkelman, H. Jónsson, *J. Chem. Phys.* **2000**, *113*, 9978.

Chapter 5

Structural Design for Realizing Highly Effective and Stable Cathodes in Rechargeable Li-Ion Batteries

5.1 Introduction

Rechargeable lithium-ion batteries (LIBs) are extensively investigated and serve in electrical vehicles and electronic devices because of their low cost, light weight, high energy density, long cycle life and eco-friendly properties.[1, 2] In spite of recent achievements around innovative synthesis of materials and improved technology for fabrication, the increase in demands for high-performance LIBs is encouraging their further developments, in particular, around energy/power density, stability and rate capacity. Compared to the diverse active materials for anodes with higher specific capacity, whereas the electrochemical performance of LIBs full cells is restricted by the relatively low capacity of the cathodes.[3, 4] The majority of commercial cathode materials, for instance $LiCoO_2$, $LiMn_2O_4$ and $LiFePO_4$,[5] in theory could only afford single Li^+ ion insertion/extraction per unit cell due to their inherent crystal structures and redox electrochemistry. Therefore, multi-Li^+ ion insertion/extraction active materials for cathodes could enable high capacity batteries.

Among all materials for cathodes in LIBs, vanadium pentoxide (V_2O_5) is one of the perspective candidates that could meet the high capacity requirements. Its layered structure could insert/extract multiple Li^+ *via* reversible phase transformations, and the structural formula of as-formed $Li_xV_2O_5$ could be formulated as: α phase: $x < 0.1$; ϵ phase: $0.35 < x < 0.7$; δ phase: $x = 1$; γ phase: $1 < x < 3$ and ω phase: $x = 3$.[6] At the voltage range of 2.0-4.0 V, V_2O_5 materials could undergo intercalation of two Li^+ ions with theoretical specific capacity reaching 294.0 mAh g^{-1}. However, low Li diffusion coefficient, poor electrical conductivity and undesirable structural stability affect the electrochemical energy storage performance of V_2O_5.[4, 6-8] From previous work, two representative strategies have been proposed. One focus is the design of novel V_2O_5 structures, such as nanobelts[7], nanosheets[5, 9] and microspheres[10]. These structures could increase the active surface area and enhance the diffusion efficiency of Li^+ ions.

Recently, Liang *et al.* reported the synthesis of ultra-thin and large V_2O_5 nanosheets. These nanosheets possess a high specific discharge capacity of 141 mAh g^{-1} at a current density of 0.1 A g^{-1} with superior stability showing 92.6 % retention after 500 cycles.[11] The other method is to synthesize V_2O_5-based composites, such as V_2O_5-graphene xerogel[6], SnO_2/V_2O_5 composites[12] and V_2O_5/mesoporous carbon composites[13].

Direct synthesis of active materials on current collectors has been proved to escape sophisticated electrode fabrication process compared with powdery materials mentioned above and the mixed slurry procedure as-required[6-13]. Previous work and chapters have reported the disadvantages and complex procedures of making electrode materials with binders and conductive agents.[14, 15] However, some common issues still remain for the reported core-shell structured composites[4, 16-19]. Firstly, the electrochemical energy storage were contributed from reactions of both core and the shell structures simultaneously, which would still cause undesirable stability performance of the electrodes due to cracks formed by large volumetric expansion or sometimes dissolution of the core structures; Secondly, active electrode materials are partially encapsulated by inert conductive or protective layers, which may decrease their full utilization.

Taken into consideration all the points raised above and further guided by computational simulation from our collaborator, Dr. Xiaoyu Han in Prof. Zheng Xiao Guo's group (UCL Chemistry Department), a targeted approach to design and synthesize the V_2O_5 coated $NiCo_2O_4$ porous structure on carbon cloth, *i.e.* 3D $NiCo_2O_4@V_2O_5$ core-shell arrays (CSAs), was developed. In Chapter 2, the use of the bi-transitional metal oxides have been proved to enhance the electrical conductivity of the entire structures compared to single-metal oxides. In Chapter 4, carbon cloth as a flexible current collector were introduced. Inspired by previous strategies, the $NiCo_2O_4$ nanosheet network is firstly grown onto the carbon clothes and then the optimised thickness of layered V_2O_5 is coated onto

the $NiCo_2O_4$ network. This approach effectively separates the proper roles of Li storage in V_2O_5 and electronic conduction *via.* $NiCo_2O_4$ and carbon cloth nano-network. Meanwhile, the volumetric expansion of V_2O_5 during lithiation/delithiation is fully alleviated by the robust $NiCo_2O_4$ nanosheets, without exerting undue stress on the carbon cloth. The as-designed structures as the electrodes for LIBs reached the theoretical capacity of V_2O_5 materials over the high voltage range during 2.0 - 4.0 V *vs.* Li^+/Li and delivered one of the best reported stabilities. Moreover, *in-situ* TEM study and computational simulations also provide insights into the robustness of the structural design and the mechanism of the layer effects in these rational electrodes, which will guide studies around V_2O_5 based LIBs in the future. As-designed self-standing electrodes display distinct merits: flexibility; large surface area; easy access of electrolyte and facile electron/ion transport. The electrodes also show potential applications as cathodes for foldable/flexible Li-battery devices.

5.2 Experimental section

Electrode Preparation. All chemicals used in this work are commercially available from Sigma-Aldrich (U.K.) and were used as-received without further purification. The $NiCo_2O_4@V_2O_5$ CSAs were synthesized on carbon cloth *via* a two-step hydrothermal reaction with annealing afterwards. At first, $Co(NO_3)_2•6H_2O$ (0.58 g), $Ni(NO_3)_2•6H_2O$ (0.29 g) and methenamine (0.56 g) were dissolved into a solution of methanol (35 mL) to form a clear pink solution in an autoclave. The carbon cloth substrates were cleaned by sonication in acetone, deionized (DI) water and ethanol successively for 30 min, and transferred to the above autoclave in an electrical oven at 160 ˚C for 6 h. After the reaction, the NiCo hydroxides on carbon cloth was annealed at 300 ^oC for 2 h under air in the tube furnace. During the initial step, four pieces of carbon cloth were prepared. Secondly, different amounts of vanadium oxytriisopropoxide (0.1 ml, 0.2 ml, 0.4

ml and 0.6 ml) were mixed with isopropanol (50 mL) in four separate 60 mL teflon-lined autoclaves under magnetic stirring for 30 min. Afterwards, the magnetons were taken out and one piece of $NiCo_2O_4$ nanosheet arrays coated carbon cloth were put inside of each liner, which was sealed and heated in an electrical oven at 200 ^oC for 12 h. Then, the as-synthesized electrode materials on carbon cloth were washed with DI water and ethanol to remove any loosely attached powders and remove any residual ionic species and dried in a vacuum oven at 60 ^oC for 24 h. Finally, the as-synthesized samples on carbon cloths were annealed at 350 ^oC for 2 h under air in a tube furnace.

Characterization. Micro/nanostructures of the as-synthesized electrodes were characterized by SEM (S-4800; Hitachi) and TEM (JEOL, JEM-2100F equipped with an energy-dispersive X-ray spectrometer). X-ray diffraction patterns were recorded using a STOE StadiP diffractometer with Mo-Kα radiation (λ = 0.71 Å). The mass of the active materials was weighed using the accurate balance (readability of 0.001 mg). *In-situ* TEM observation of the lithiation/delithiation process was conducted by a scanning tunneling microscopy-TEM holder from Nanofactory Instruments AB (Gothenburg, Sweden) within the JEOL 2100F TEM under the accelerating voltage of 200 kV.

Electrochemical measurements. The $NiCo_2O_4$@V_2O_5 CSAs/carbon cloth nanocomposites were served as working electrodes directly without extra conductive agents or binder materials. The loading densities were calculated as 1.790-1.816, 2.594-2.618, 3.040-3.072, 3.640-3.812 mg/cm^2 for the four types of electrodes, the mass density of $NiCo_2O_4$ nanosheet arrays was 0.994-1.024 mg/cm^2 on the carbon cloth. The V_2O_5/carbon cloth were loaded with ~ 1.76 mg/cm^2 of V_2O_5. The mass of the carbon cloth in each coin cell is ~ 18 mg. As for the compared electrodes, the working electrode was prepared by mixing the V_2O_5 nano-flowers, conductive substance (carbon black) and binder (sodium alginate) with a weight ratio of 50:40:10. Coin-type cells (CR2032) were fabricated using

lithium metal as the counter electrode, Celgard 2400 (Charlotte, NC, USA) as the separator and 200 μL of 50 $LiPF_6$ (1 M) in ethylene carbonate-dimethyl carbonate (1:1 vol%) as the electrolyte. Cyclic voltammetry (CV) measurements were conducted at 0.1 mV s^{-1} in the range of 2.0 ~ 4.0 V (*vs.* Li/Li^+) on a CHI 600D (Shanghai, China) potentiostat. Electrochemical impedance spectroscopy was carried out with a ZAHNERelektrik IM 6 (Kronach) potentiostat at a frequency range of 100 kHz to 0.01Hz. All electrochemical measurements were tested more than twice to ensure the replication of the results.

Theoretical calculation of layered effect for lithiation in V_2O_5. DFT+U calculations were carried out by a projector-augment wave (PAW) pseudopotential, implanted in the Vienna *Ab initio* Simulation Package (VASP).[20] As the van der Waals interaction dominant the intra-layer of α-V_2O_5, serial functions have been assumed for comparison, including PBEsol-vdW-DF, PBE-vdW-DF2, and optPBE-vdW.[21-28] The plane-wave basis was set with energy cut-off of 520 eV, which has been proven large enough to ensure the methods correctly reproduced the V_2O_5 strudcutre.[29] The Brillouin zone was sampled by Gamma centred at $2 \times 2 \times 2$ k-mesh for the bulk and $2 \times 2 \times 1$ for the layered slides. All the structures are fully relaxed, and the relaxation criteria set to the force on each atom and energy difference of each ionic step are less than 0.01 $eVÅ^{-1}$ and 10^{-5} eV, respectively. Spin polarization was counted through all the simulations. Due to the limitation of DFT calculations in presenting the delocalised *d* and *f* electrons excessively, [30] the effective Cou42lomb and exchange parameters +U was set to 4 eV, as suggested from previous work. [31]

The $2a \times 2b$ supercell of 1- to 5-layer of α-V_2O_5 have adopted for the analysis of the layer effect on Li^+ ions intra-plane and inter-plane diffusion process. Dipole correction has adopted through all the calculations. For the few-layer V_2O_5, each model has 15 Å vacuum region. Energy barriers of the Li were evaluated by the climbing image nudged elastic band (Ci-NEB) method. [32]

5.3 Results and discussion

The schematic illustration of fabricating carbon cloth supported $NiCo_2O_4$@V_2O_5 CSAs is presented in Figure 5.1 and described in detail in the experimental parts. The flexible carbon cloth with high electron conductivity and potential applications for wearable LIB devices, were selected as the current collector to support integrated electrodes. At first, $NiCo_2O_4$ nano-network was synthesized on the current collectors *via* a facile hydrothermal process followed by annealing to improve the crystallinity, bonding and further electrical conductivity. These porous networks could deliver adhesive supports and further form heterojunctions with V_2O_5 shells. Importantly, $NiCo_2O_4$ nanostructure exhibits 5 ~ 6 orders of magnitude higher electron conductivity than that of V_2O_5[33-36]. The nano-architectured design also benefits from the open channels of 3D $NiCo_2O_4$ frameworks, which provide easy access for the electrolyte thus enabling sufficient ion mobility. Then, V_2O_5 nanosheets were coated on both sides of the $NiCo_2O_4$ arrays by a hydrothermal process that formed well-connected core-shell networks. The firm structure and the strong binding between the structure and the carbon-support partially alleviates the possible stress of volumetric change during the lithiation/delithiation process. To obtain the best performed electrodes, different concentrations of precursor solution (0.1~0.4 mL) were adjusted to identify the appropriate thickness ratio of the core-shell network.

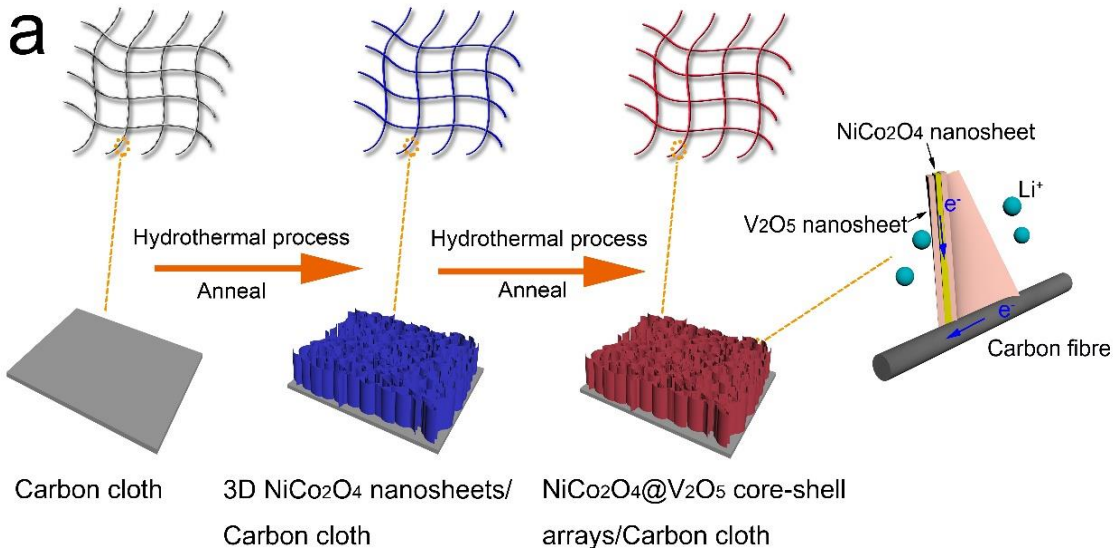

Figure 5. 1 schematic diagram showing the synthetic procedure for $NiCo_2O_4@V_2O_5$ core-shell arrays (CSAs) on carbon cloth.

The morphologies of the pure carbon cloth, carbon cloth supported $NiCo_2O_4$ and $NiCo_2O_4@V_2O_5$ CSAs were examined by SEM. As shown in Figure 5.2, the pure carbon fibers are interlaced and constituted fabric structure for promoting heterogeneous nucleation of Ni/Co precursors. During the first-step synthesis, $NiCo_2O_4$ nanosheets were grown on individual carbon fibers and formed a nano-network with a mesoporous structure as shown in Figure 5.3a. The zoom-in morphology was illustrated in Figure 5.3b, a thin layer of nanosheet could be noted and further increased the surface area of the electrodes. As for the second step, the growth of the V_2O_5 shell over the $NiCo_2O_4$ core, the amount of the precursor would influence the thickness of the V_2O_5 nanosheets. The microstructures of the nanosheets become crude showing small nanoparticles attached on the surfaces (Figures 5.4a, 5.5a), with the added vanadium precursor solution controlled at 0.1 mL. When the concentration of the precursor solution was increased to 0.2 mL, V_2O_5 nanosheets were observed to arrange on both sides of the $NiCo_2O_4$ sheets thus forming sandwich structures (Figures 5.4b, 5.5b). Further increases of the vanadium oxytriisopropoxide solution to 0.3 and 0.4 mL during sythesis, it noted that the thickness of the V_2O_5 nanosheets

increased dramatically (Figures 5.4c, 5.5c and Figures 5.4d, 5.5d). The nanosheets would then stack together and even block the porous architecture, which may retard the Li^+ ion diffusion and electron transfer during electrochemical energy storage process.

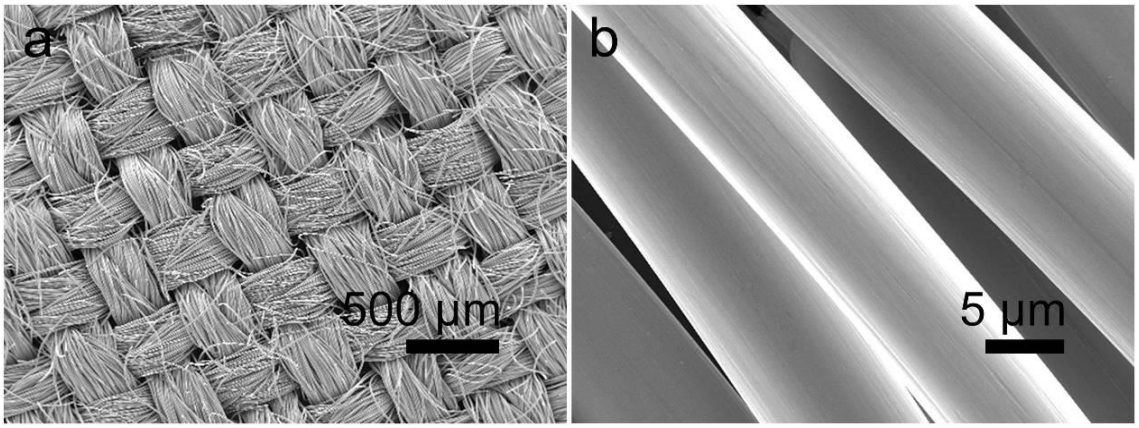

Figure 5. 2 Low and high magnification SEM of the carbon cloth.

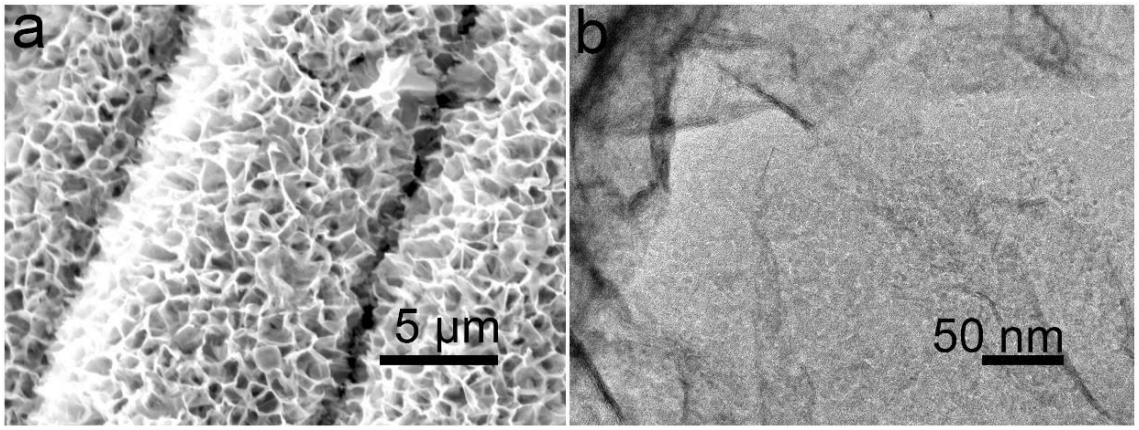

Figure 5. 3 (a) SEM image of the $NiCo_2O_4$ nanoarrays/carbon cloth; (b) TEM images of $NiCo_2O_4$ nanosheet.

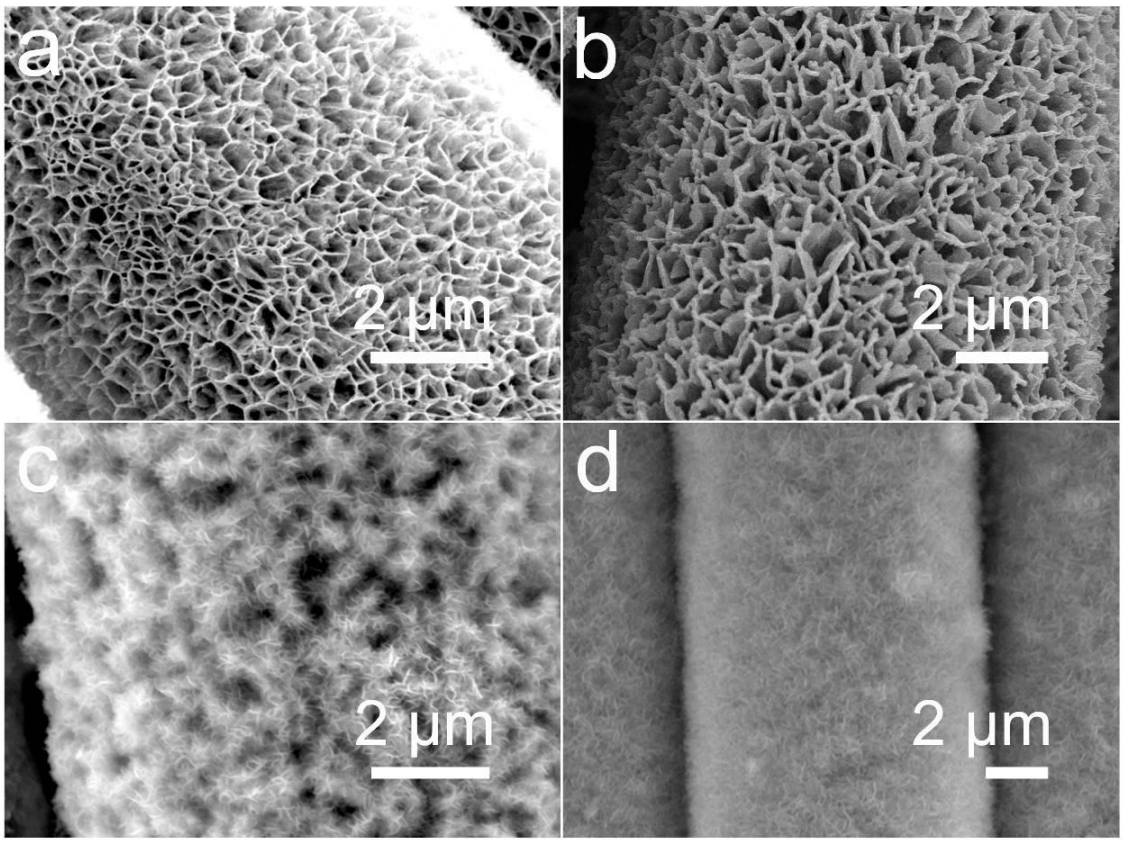

Figure 5. 4 (a-d) SEM images of four types of $NiCo_2O_4$@V_2O_5 CSAs on carbon cloth with different concentrations of reactant (b: 0.1 mL, c: 0.2 mL, d: 0.3 mL and e: 0.4 mL of vanadium oxytriisopropoxide, respectively) during second hydrothermal step.

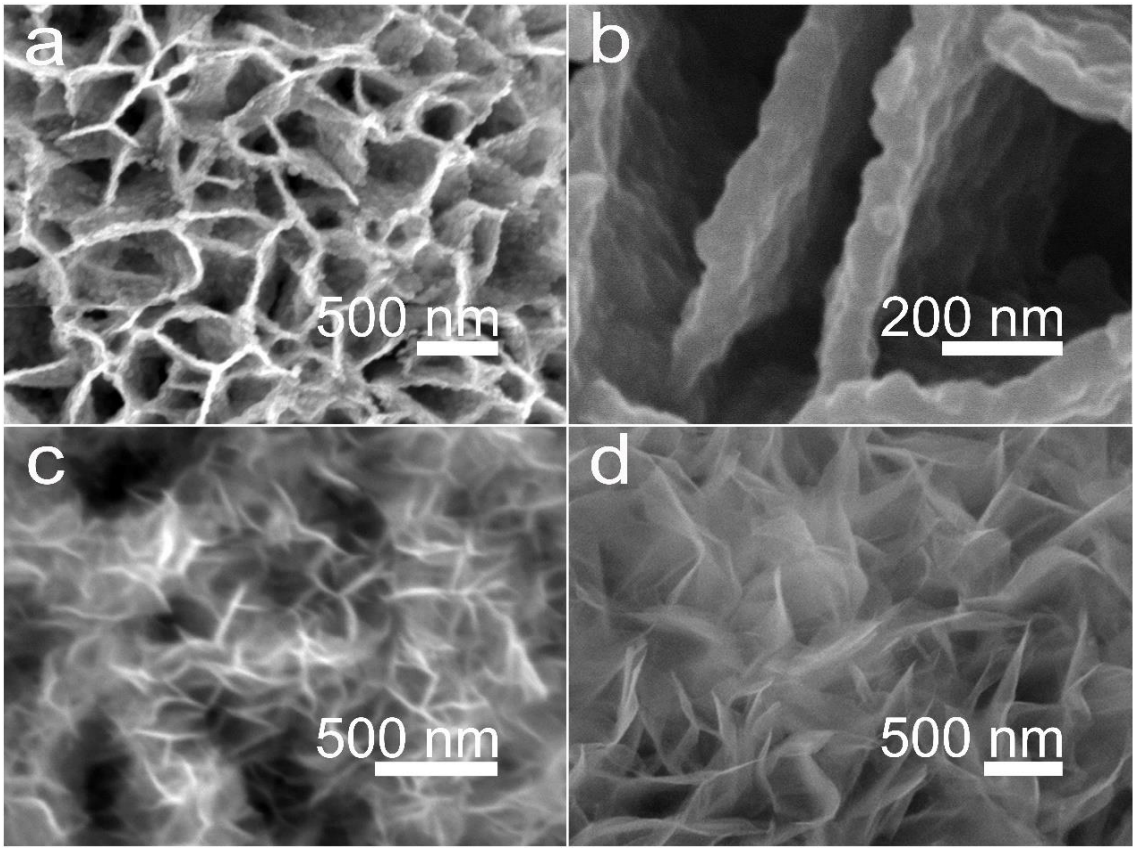

Figure 5. 5 (a-d) High magnification SEM images of four types of $NiCo_2O_4$@V_2O_5 CSAs on carbon cloth, showing the enlarged area in Figure 5.3.

The detailed topography of the sandwich-like structures was further characterized by transmission electron microscopy (TEM). The nanosheets show clearly the mesoporous structure with pore sizes of several hundred nanometers to micrometer scale, as detected from the low magnification TEM image (Figure 5.6a). The high magnification TEM observation in Figure 5.6b presents the morphology of nanosheet more broadly. As-obtained structures could afford large open surface areas for easy soak of the electrolyte, and fast transport for ions and electrons. In addition, the mesoporous structures can be noted on the individual nanosheet. High resolution TEM (HRTEM) image presenting the boundary between $NiCo_2O_4$ and V_2O_5 is shown in Figure 5.6c, where the lattice space of ~ 0.234 nm corresponds to the (222) plane of the $NiCo_2O_4$ spinel structure, while ~ 0.265 and ~ 0.438 nm could be assigned to the (310) and (001) lattice planes of the V_2O_5 orthorhombic structure, respectively. Due to the

relatively small lattice mismatch, the heterostructures constituted robust linkage across the interface, which ensures the structural integrity facilitates large amounts of Li^+ intercalation/deintercalation. The crystallographic phases of the $NiCo_2O_4$@V_2O_5 CSAs/carbon cloth were further characterized by X-ray diffraction (XRD), Figure 5.6d, where the two main diffraction peaks at 14.1º and 20.2º correspond to the (110) crystal planes of the orthorhombic phase of V_2O_5 and (400) crystal plane of the spinal phase $NiCo_2O_4$, respectively. A series of relatively weak and somewhat broad peaks could be indexed to V_2O_5 (JCPDS no. 41-1426) and $NiCo_2O_4$ (JCPDS no. 20-0781), respectively. In Figure 5.6e, X-ray mapping with a matching TEM images further elucidated the elemental distribution of the $NiCo_2O_4$@V_2O_5 CSAs, the result revealed that Ni, Co, V and O are distributed in the core with Ni, Co, O elements and the shell (V, O) regions uniformly.

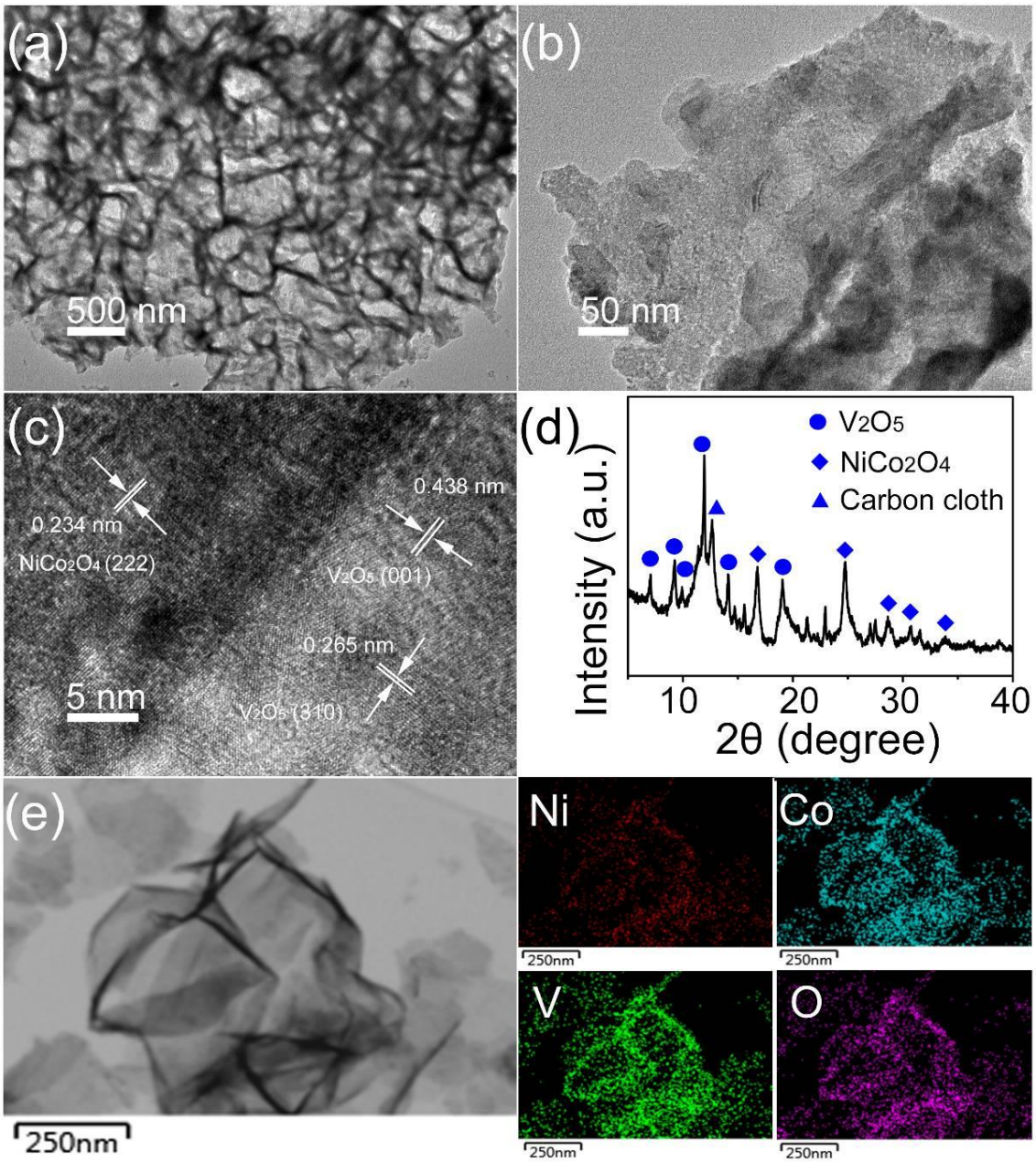

Figure 5. 6 (a) Low- and (b) high-magnification TEM images of $NiCo_2O_4$@V_2O_5 CSAs; (c) High resolution TEM images of $NiCo_2O_4$@V_2O_5 CSAs; (d) XRD pattern of $NiCo_2O_4$@V_2O_5 CSAs/carbon cloth; (e) the TEM image and its corresponding elemental maps.

The electrochemical properties of four types of $NiCo_2O_4$@V_2O_5 CSAs as the cathodes for LIBs were evaluated as shown in Figure 5.7. The specific capacity and the cycling performance was investigated at a current density of 0.5 C for 100 cycles, as shown in Figure 5.7a. As expected, compared with other electrodes, sandwich-structural CSAs, electrode b, shows the best performance

with the highest discharge capacity of ~ 276.4 mA h g^{-1}, calculated based on the total mass of $NiCo_2O_4$ framework and V_2O_5 material, (discharge capacity of ~ 238.9 mA h g^{-1}, ~ 197.3 mA h $g^{-1}$and ~ 166.8 mA h g^{-1} for electrode a, c and d, respectively). The results indicate that the thickness of the V_2O_5 nanosheet out-layers affects the specific capacity. The following electrochemical performance was carried out using the sandwich-structural $NiCo_2O_4$@V_2O_5 CSAs electrode.

The CV plots of the first and second cycles are shown in Figure 5.7b at a low scan rate of 0.1 mV s^{-1} within the potential window of 2.0 - 4.0 V *vs.* Li/Li^+. During the second stable cycle, the first cathodic peak at 3.34 V can be indexed to phase changes from α-$Li_xV_2O_5$ (x < 0.1) to ε-$Li_{0.5}V_2O_5$. Another two reduction peaks at 3.13 and 2.23 V can be ascribed to the formation of δ-LiV_2O_5 and ϒ-$Li_2V_2O_5$, respectively. In the Li de-intercalation process, three anodic peaks observed at 2.52, 3.28 and 3.48 V correspond to the reverse phase transformations, *i.e.* from ϒ-$Li_2V_2O_5$, δ-LiV_2O_5, ε-$Li_{0.5}V_2O_5$ to α-$Li_xV_2O_5$ (x<0.1), respectively.[3] There are no other available peaks from the CV curves, suggesting only the V_2O_5 phase transformations take place in the electrochemical reactions. This also indicates the stable network structure was introduced during the entire electrochemical process. The reaction processes could be expressed as below[3]:

$$V_2O_5 + 0.5\ Li^+ + 0.5e^- \leftrightarrow \varepsilon\text{-}Li_{0.5}V_2O_5 \quad (5.1)$$

$$\varepsilon\text{-}Li_{0.5}V_2O_5 + 0.5\ Li^+ + 0.5\ e^- \leftrightarrow \delta\text{-}LiV_2O_5 \quad (5.2)$$

$$\delta\text{-}LiV_2O_5 + Li^+ + e^- \leftrightarrow \gamma\text{-}Li_2V_2O_5 \quad (5.3)$$

Figure 5.7c shows the first, second and fifth cycles of the CD curves for the $NiCo_2O_4$@V_2O_5 CSAs at a current density of 0.1 C. After the first cycle to form the solid state electrolyte interface, the specific capacity remains stable and then decreases slowly. As shown in this figure, there is no evidence of flat voltage plateaus in the charge and discharge curves, which suggests relatively low crystallinity of the V_2O_5 structure. It is demonstrated that lower crystallinity can

lead to less stress on the electrodes during the Li ion insertion/extraction and better cyclic performance. In line with the above CV results, three distinct voltage stages could be observed at 3.40-3.32, 3.15-3.10 and 2.35-2.23 V on the discharge curves. These stages suggest the Li ion intercalation procedure. Likewise, three corresponding voltage stages at 2.42-2.55, 3.20-3.35 and 3.42-3.53 V are related to the Li ion de-intercalation processes. As stated above, both CV and CD results verify the multi-step Li intercalation process.

Rate capabilities of the $NiCo_2O_4$@V_2O_5 CSAs are further presented in Figure 3d. At a current density of 0.1 C, a stable discharge capacity of 292.0 mA h g^{-1} was achieved. With the increase of current densities, the discharge capacities decrease to 256.8, 198.4, 151.9 and 128.7 mA h g^{-1} at 1.0 C, 5.0 C, 10 C and 20 C, respectively. It is noted that the electrodes show excellent rate performance of ~ 45% retention with an increased current density of 200 times. The specific discharge capacity of 271.6 mAh g^{-1} can be maintained when the current density was recovered to 0.1C after 60 cycles of stepwise current density changes, corresponding to a capacity retention of ~ 93.0 % of its initial value. These improvements can be attributed to the complete Li intercalation/de-intercalation reaction of the V_2O_5 coating and rapid charge and Li^+ mobility within the entire heterostructure. The discharge capabilities of the $NiCo_2O_4$ nanosheet are shown in Figure 5.8, this skeleton structure has negligible capacity contribution of 14.6 and 6.9 mAh g^{-1} at current densities of 0.1 C and 1 C, respectively. It can be reflected that the $NiCo_2O_4$ core structure shows almost no electrochemical reactions with Li^+ within the voltage range of 2.0-4.0 V *vs*. Li^+/Li and this largely insignificant capacity is because of the limited ion absorption from the surface-controlled process.

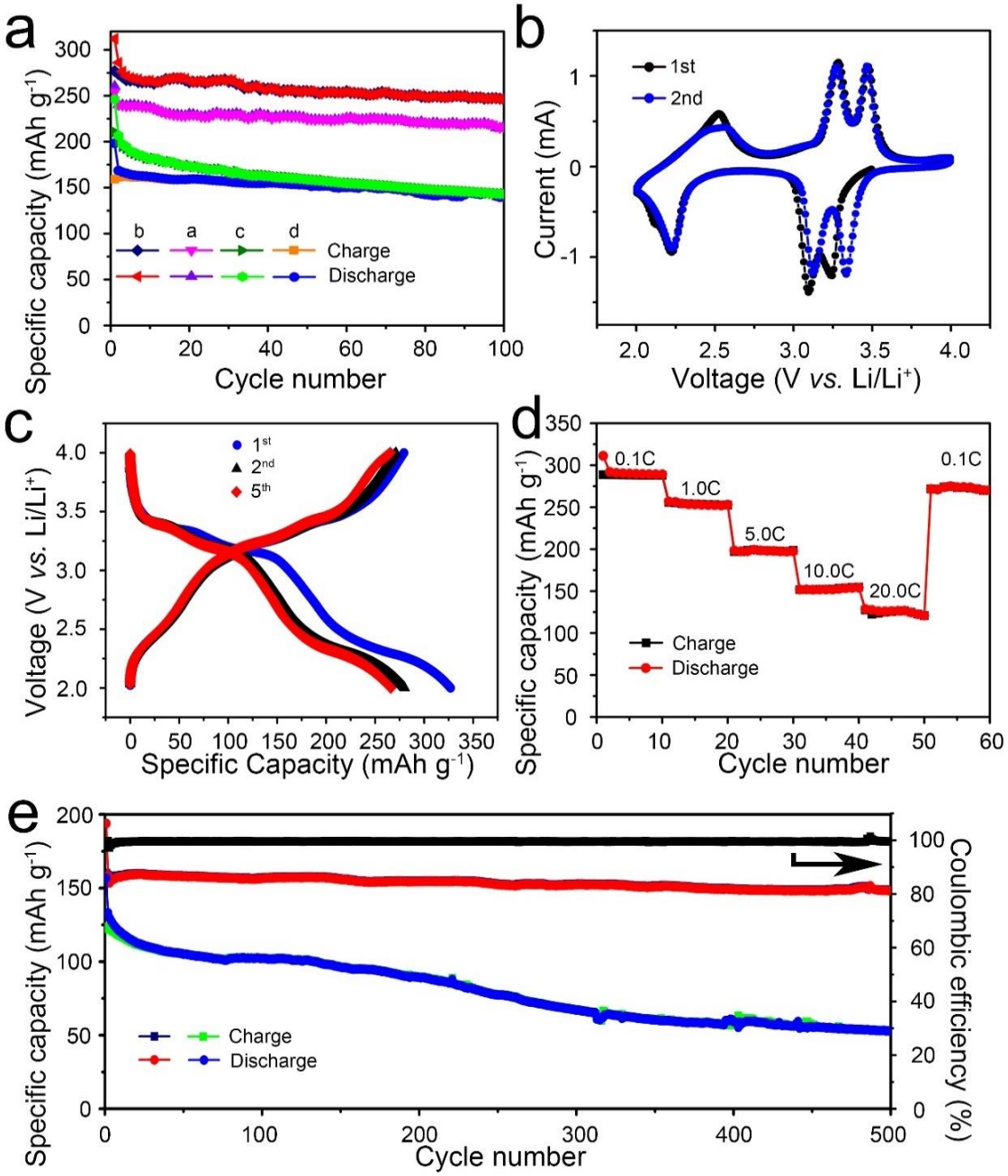

Figure 5. 7 (a) Cycling performances of four types of $NiCo_2O_4@V_2O_5$ at a current density of 0.5 C (a, b, c and d suggest different electrodes in Figure 5.5a, b, c and d); (b) Cyclic voltammetry (CV) measurements of $NiCo_2O_4@V_2O_5$ CSAs at a scan rate of 0.1 mV s^{-1}; (c) Charge-discharge curves (CD) of $NiCo_2O_4@V_2O_5$ CSAs at a current density of 0.1C. (d) Rate performances of $NiCo_2O_4@V_2O_5$ CSAs at different current densities; (e) Cycling performance and corresponding Coulombic efficiency of $NiCo_2O_4@V_2O_5$ CSAs and cycling performance of V_2O_5 nanoparticles measured at high current density of 10 C.

To tackle the persistent challenge of unsatisfied cyclic stability for these materials, the $NiCo_2O_4$@V_2O_5 CSAs electrode was evaluated under 500 cycles of a GCD test at a high current density of 10 C in Figure 5.7e. Notably, except for the first few cycles, the cycling stability was largely maintained with only 0.0126 % capacity loss per cycle within 500 cycles and a Coulombic efficiency > 99.5 %. For comparison, flower-like V_2O_5 nanoparticles (power samples) and V_2O_5/carbon clothes (Figure 5.9) were constructed into coin cells as cathodes in LIBs. After 500 cycles under the same conditions, the retention of capacities are 40.7% and 33.5% of their initial value, respectively, equivalent to decline of 0.12% and 0.13% capacity per cycle.

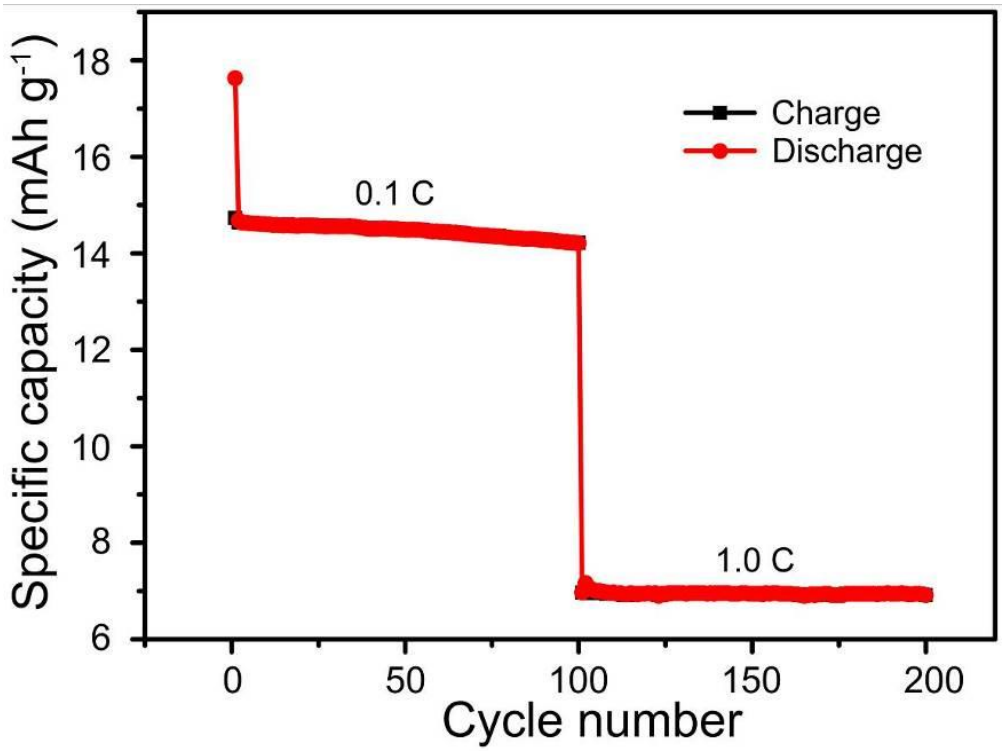

Figure 5. 8 Rate capability of carbon clothes supported $NiCo_2O_4$ nanosheet arrays.

Therefore, carbon cloth supported $NiCo_2O_4$@V_2O_5 CSAs electrodes improved the cycling stability by 10 times, in comparison with the V_2O_5 nanoparticles and V_2O_5/carbon cloth obtained from the same process. All these results demonstrate the excellent cyclic stability and reversibility with no side reactions in the

$NiCo_2O_4$@V_2O_5/carbon cloth electrodes. Compared with the previous work, the exceptional cycling performance of the $NiCo_2O_4$@V_2O_5 CSAs/carbon cloth electrodes is among the best reported nanostructures for cathodes in LIBs (Table 1). The long lifetimes were consistent with almost no obvious destruction of morphology after 500 cycles, though the sandwich network became thicker in Figure 5.10a, the porous structures of $NiCo_2O_4$@V_2O_5 CSAs structure remains complete. As for powdery V_2O_5 electrodes, the surface appeared to be rough and the nanoparticles further stacked together, shown in Figure 5.10b, which may prohibit the access of the electrolyte and the Li^+ diffusion during the electrochemical processes.

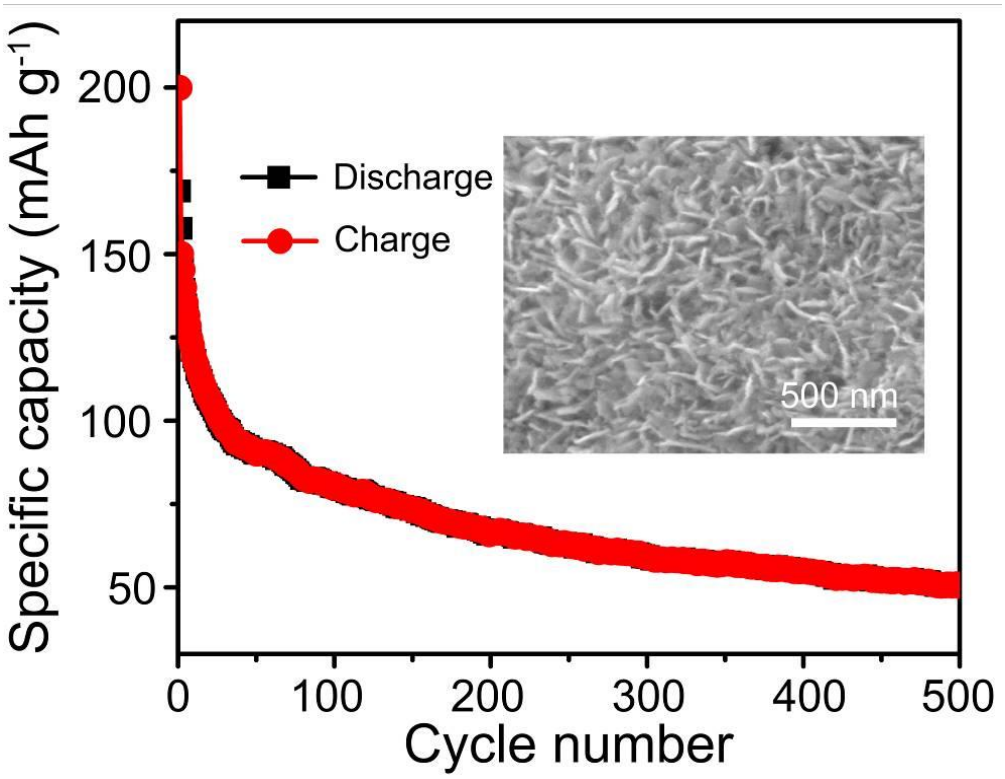

Figure 5. 9 Cycling stability of V_2O_5 nanoflowers on carbon cloth at high current density of 10 C, inset showing the SEM image of the V_2O_5 nanoflowers on carbon clothes.

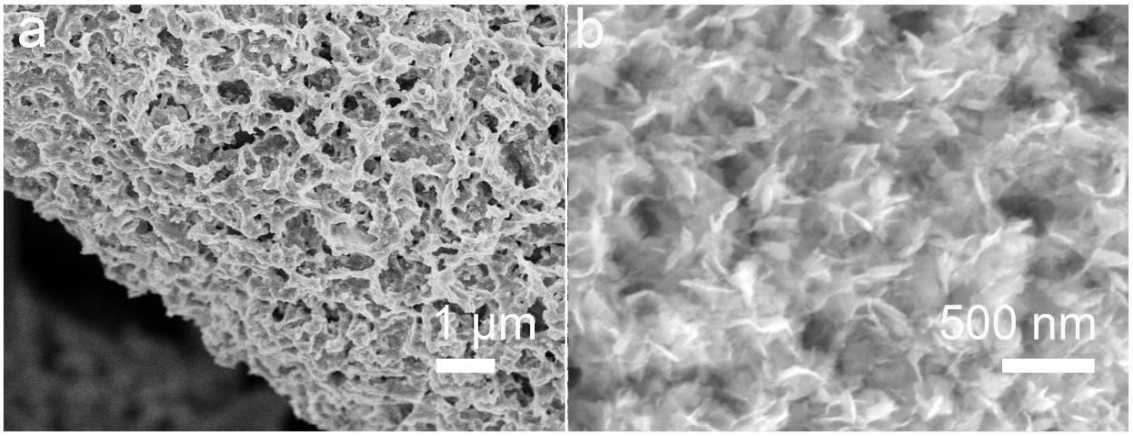

Figure 5. 10 SEM images of carbon cloth supported $NiCo_2O_4@V_2O_5$ CSAs and V_2O_5 nanoparticles after 500 cycles at the high current density of 10 C.

The outstanding stability and the morphologies further confirm the remarkable benefit from the rational design and the robustness of the open network. The overall energy storage performance for the optimized structures is better than a large series of reported cathode nanostructures for LIBs (Table 5.1).

Table 5. 1 Comparison of electrochemical performances of $NiCo_2O_4@V_2O_5$ SAs/carbon cloth as cathodes in LIBs with the representative cathodes in the literature.

Cathodes for LIBs	Specific capacity (Current density)	Rate performances (Increased current density)	Stability	Reference
$NiCo_2O_4@V_2O_5$ CSAs/carbon cloth	292 mAh g^{-1} (0.1 C)	45% retention (200 times)	0.0126% decrease per cycle (500 cyles at 10 C)	This work
V_2O_5 nanobelts	280 mAh g^{-1} (0.2 C)	32% retention (200 times)	0.28% decrease per cycle (50 cycles at 0.2 C)	[7]
V_2O_5 @carbon nanotubes	224 mAh g^{-1} (0.1 C)	40.2% retention (1000 times)	0.0415% decrease per cycle (200 cycle at 0.5 C)	[4]
Porous V_2O_5 microspheres	275 mAh g^{-1} (0.125 C)	33.5% retention (120 times)	0.38% decrease per cycle (20 cycles at 0.2 C)	[10]

V^{4+}-V_2O_5 nanoflake	293 mAh g^{-1} (100 mA g^{-1})	47.4 % retention (40 times)	0.05% decrease per cycle (100 cycles at 2000 mAh g^{-1})	[37]
V_2O_5 nanosheets	141 mAh g^{-1} (100 mA g^{-1})	88% retention (60 times)	0.09% decrease per cycle (100 cycles at 100 mAh g^{-1})	[33]
$LiNi_{0.4}Mn_{0.4}Co_{0.2}O_2$ spherical particles	228 mAh g^{-1} (0.05 C)	————	0.2% decrease per cycle (20 cycles)	[38]
V_2O_5 nanoparticles	285 mAh g^{-1} (0.5 C)	62.4% retention (40 times)	0.44% decrease per cycle (50 cycles)	[39]
V_2O_5/graphene	432 mAh g^{-1} (0.05 C)	45.8% retention (200 times)	0.13% decrease per cycle (200 cycles at 1 C)	[6]
$Li_4Mn_2O_5$ composition	355 mAh g^{-1} (0.05 C)	————	3.7% decrease per cycle (8 cycles)	[40]
Hydrogenated V_2O_5 nanosheets	252 mAh g^{-1} (0.1 A g^{-1})	54.8% retention (20 times)	0.42% decrease per cycle (200 cycles at 0.1 A g^{-1})	[5]

As discussed in previous contents, poor structural stability, inferior electron conductivity and sluggish Li diffusivity are the main obstacles for V_2O_5 materials as cathodes in LIBs. The first problem, unstable structures, mainly originated from the strains produced from the volumetric expansion of the electrochemical active material during the lithiation process. It could result in cracks, falling-off and electrical disconnection with the building blocks and the current collectors, thus shortening the lifespan of LIBs. *In-situ* TEM observation was carried out by a dual-probe biasing TEM holder in Figure 5.11a to monitor the mechanical properties and morphological evolution of $NiCo_2O_4$@V_2O_5 CSAs during Li intercalation and de-intercalation within layers of V_2O_5. The related experiments were collaborated with Prof. Rujia Zou in Donghua University. $NiCo_2O_4$@V_2O_5 CSAs were fixed on a Pt wire probe, the opposite side was an Au wire probe assembled with a small piece of Li/Li_2O. By manipulating a piezoelectric motor on the TEM holder, the $NiCo_2O_4$@V_2O_5 CSAs could contact with Li/Li_2O, then the Li^+ ion would go through the solid-state electrolyte towards $NiCo_2O_4$@V_2O_5 CSAs under driving

by a bias voltage of - 4.0 V. Figure 5.11b shows the pristine states of $NiCo_2O_4$@V_2O_5 CSAs before the lithiation. Afterwards, the $NiCo_2O_4$@V_2O_5 CSAs went through the lithiation process for 15 min, where the coated structure continues to expand, as shown in Figure 5.11c. After 30 min (Figure 5.11d), further volumetric expansion is negligible which verifies the completion of the intercalation reaction. The main period for volumetric expansion is in the initial 15 min. Compared with its initial state, *ca.* 1.22 times of volume change can be noted.

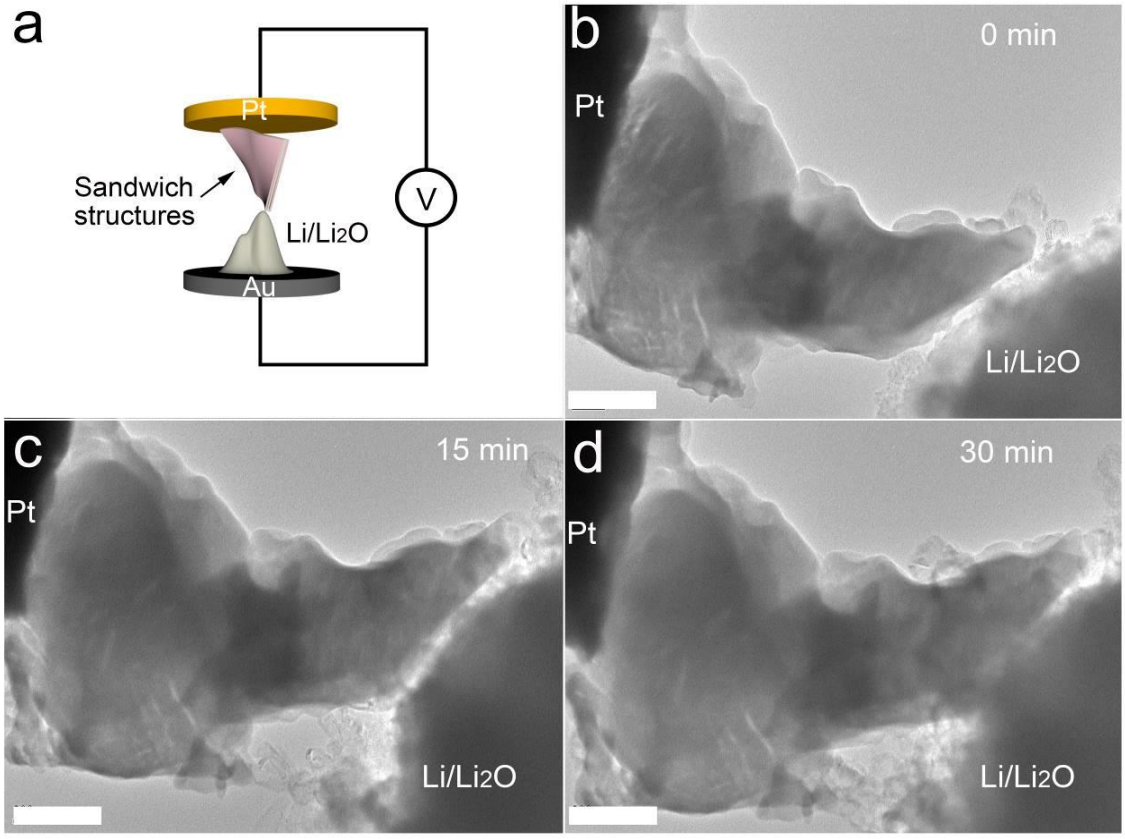

Figure 5. 11 (a) Schematic diagram suggesting the configuration of *in-situ* TEM observations during the lithiation process; (b-d) TEM images detecting the lithiation process of the $NiCo_2O_4$@V_2O_5 CSAs at 0, 15 and 30 min, respectively (Scale bar: 500 nm).

The delithiation process was also recorded in Figure 5.12 after 30 min. Compared with its initial state, an increased thickness of the coating is due to the distortion

of V_2O_5 during lithiation/delithiation. No obvious cracks could be observed or fractures in the $NiCo_2O_4$@V_2O_5 CSAs during the whole process of lithiation. As expected, there is tiny volumetric expansion noted for $NiCo_2O_4$@V_2O_5 CSAs and the $NiCo_2O_4$ core structure possesses sufficient ductility to adapt to the volumetric expansion, which could protect the entire structure during lithiation. The observation of the whole electrochemical process demonstrates clearly the structural stability and the excellent cycling performance of these sandwich structures. These results were in accordance with the SEM images before and after long-term cycling.

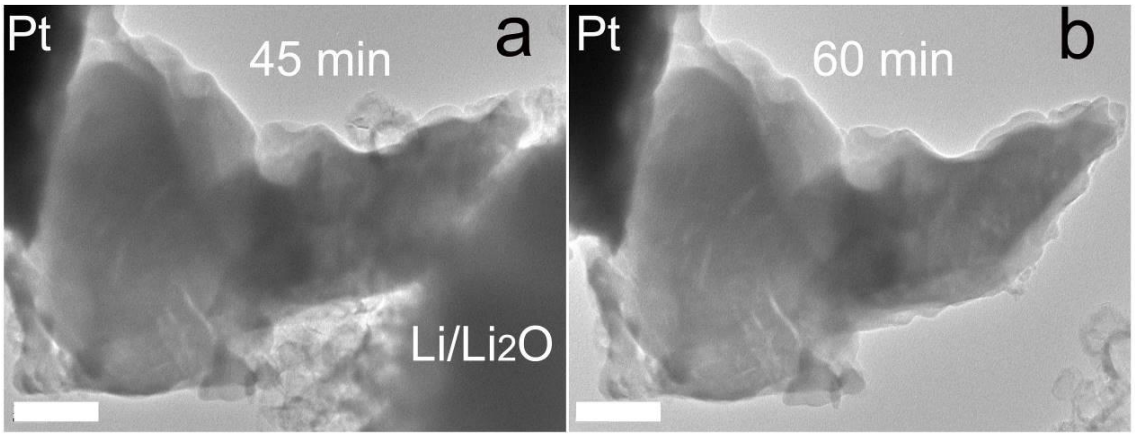

Figure 5. 12 TEM images monitoring the de-lithiation process of the $NiCo_2O_4$@V_2O_5 CSAs at time equal to 45 and 60 min, respectively (Scale bar: 500 nm).

To further elucidate and assuage the contradiction of sluggish Li diffusivity within the layered V_2O_5 structures, theoretical calculations were carried out to study the Li intercalation within layered α-V_2O_5 by Density Functional Theory (DFT). At first, the simulated lattice parameters and the V-O bond distances of the α-V_2O_5 structure from different functionals were compared with previous work, which are shown in Table 5.2.

Table 5. 2 Comparison of different functional and van der Waals correction of lattice parameters and V-O bond distances of bulk α-V_2O_5.

	a	b	c	V-O_1	V-O_2	V-O_3	V-O_4	V'-O_1
	This work							
PBEsol-vdW-DF	11.567	3.581	4.392	1.606	1.793	1.884	2.036	2.786
Error	0.47%	0.48%	0.55%	1.58%	0.73%	0.16%	0.69%	-0.25%
PBE- vdW-DF2	11.833	3.663	4.493	1.624	1.824	1.927	2.091	2.870
optPBE-vdW	11.648	3.606	4.422	1.609	1.802	1.897	2.048	2.814
	Comparison							
Theoretical work[41]	11.690	3.628	4.423	1.620	1.810	1.912	2.046	2.804
Error	1.55%	1.80%	1.26%	2.47%	1.69%	1.65%	1.19%	0.39%
Theoretical work[21]	11.496	3.630	4.804	1.602	1.805	1.915	2.018	3.204
Error	-0.14%	1.85%	9.98%	1.33%	1.40%	1.81%	-0.20%	14.7%
Experimental work[42]	11.512	3.564	4.368	1.581	1.780	1.881	2.022	2.793

In previous theoretical calculations, the *c* vector, suggesting the stacking direction, is excessively overestimated, even by 9.98 %,[21, 41] because the van der Waals contributions are not adequately considered from the standard DFT calculations. This is actually significant for layered structures.[43] The discrepancy of the reported predictions with the experimental values are relatively large. In addition, the PBEsol functional has verified to yield property predictions of densely packed materials and their surfaces.[32] The results match well with previous experimental data with the error of the lattice parameters under 0.55%. Therefore, the PBEsol-vdW-DF functional should be suitable for prediction of the geometries of α-V_2O_5, which is important for further calculation as its high thermal expansion coefficients.[44] Thus, this functional was used in the calculation afterwards.

Figure 5.13 shows the calculated electronic density of states (DOS) of α-V_2O_5. The direct band gap at Gamma point is 2.55 eV, whereas the indirect band gap

is 1.98 eV, which is in consistency with previous calculations[41] and experimental results.[45-47] The partial charge density of the valence band maximum (VBM) and the conduction band minimum (CBM) are shown in Figures 5.14a and 5.14b, where the VBM is primarily centred on vanadium atoms, consisting of $3d_{xy}$ orbitals and the CBM is concentrated on the oxygen atoms.

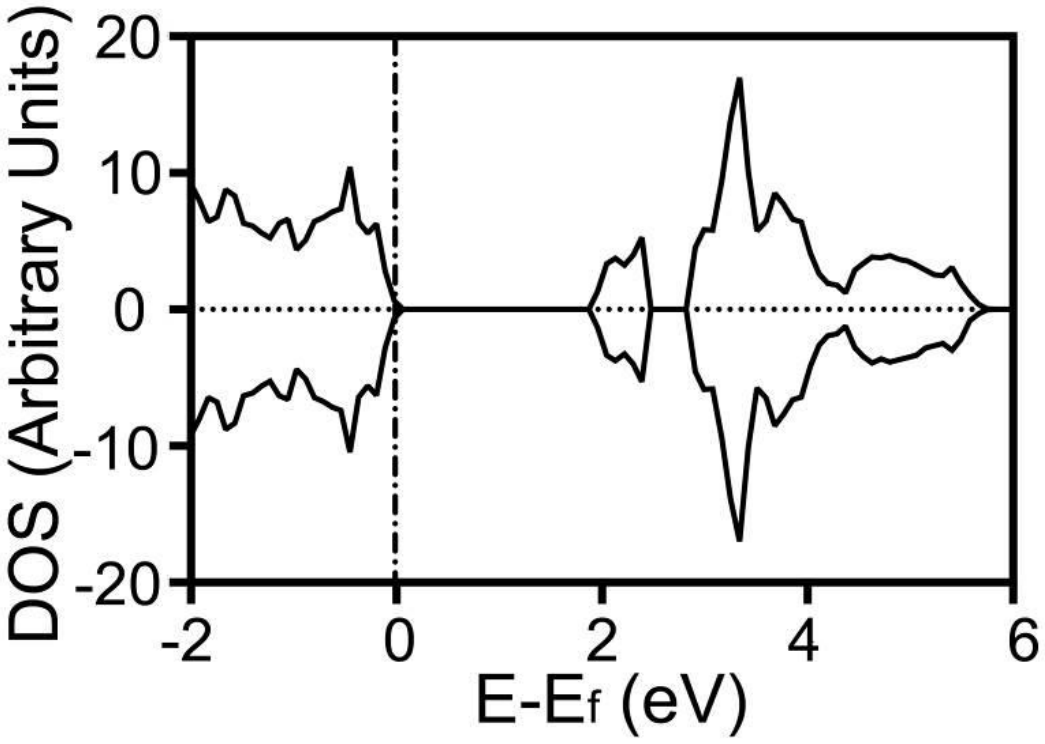

Figure 5. 13 Calculated electronic density of states (DOS) and band structure of α-V_2O_5.

The stable insertion sites of Li in α-V_2O_5 were investigated. Three possible sites were denoted as H_a and H_b for upper and the lower hollow sites and *T* for top site. The binding energy is calculated according to the following equation:

$$E_b = E_{total} - (E_{V_2O_5} + E_{Li}) \qquad (5.4)$$

where E_{total} is the energy of the entire system, $E_{V_2O_5}$ and E_{Li} are the energies of the pristine layered V_2O_5 and the chemical energy of a single Li, respectively.

The results shown from calculation suggested that the upper hollow site H_a is all over the most stable one, followed by the top site *T*. The lower site H_b is the least favourable for insertion. This result is in accordance with previous work.[41, 48] Meanwhile, the layer effect also plays an important role in the binding energy. The deeper the Li is inserted, the higher the binding energy E_b. This indicates that the Li atoms tend to bind with the top layers of the α-V_2O_5.

As for the Li-diffusion in the layered α-V_2O_5, two potential pathways have been considered and discussed, as illustrated in Figures 5.14c and 5.14d. Diffusion within the layers has been intensively studied from previous theoretical reports.[41, 48-50] However, the study around the other path where Li diffuses across the layered α-V_2O_5 has not been reported yet, neither has the layer effect on the Li diffusivity. For Li diffusion in the non-interaction lattice, the diffusion coefficient can be simply calculated by $\mathrm{D} = \Gamma \times d^2$, where Γ and d are the hopping frequency and hopping distance, respectively.[51] Further by adopting the Arrhenius theory and the transition state theory, the equation of diffusivity could be summarized by the following equation:[52]

$$D = d^2 v^* e^{-\frac{E_{act}}{k_B T}} \qquad (5.5)$$

where E_{act} is the activation energy, v^* is the attempt frequency, k_B and *T* are the Boltzmann constant and temperature respectively. As for the activation energy E_{act} of a Li atom to diffuse through the α-V_2O_5, it could be simplified as the energy barrier along the diffusion pathway. The attempt frequency v^* is generally in the range of phonon frequencies,[53] which is adopted from the experimental data in the literature[54], *i.e.* $v* = 3.1 \times 10^{13}$ Hz.

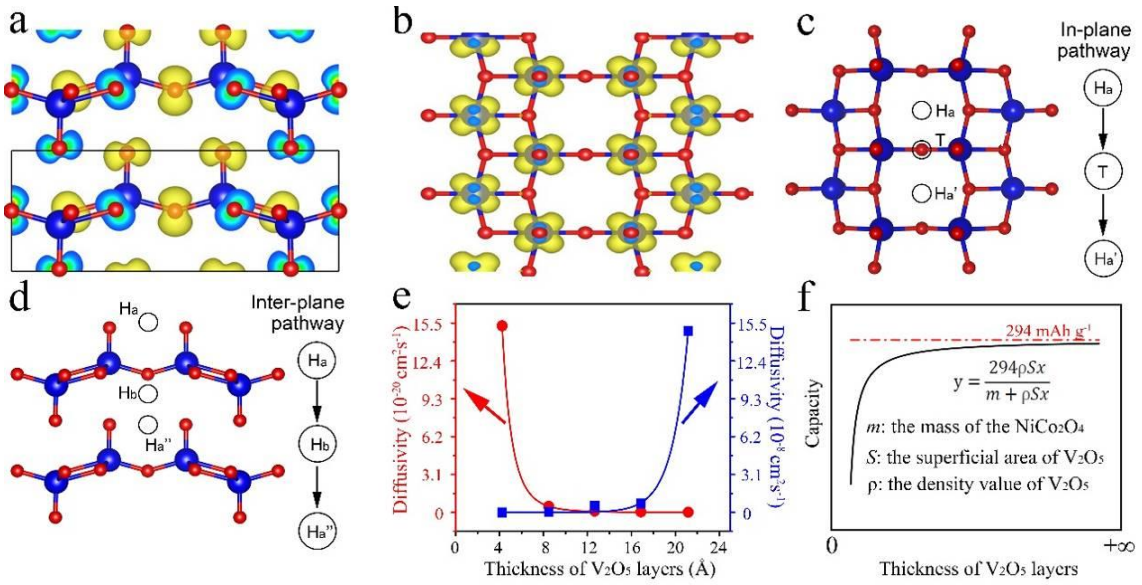

Figure 5. 14 (a, b) The side-view and top-view of α-V_2O_5 with the partial charge density of the valence band maximum (a) and conduction band minimum (b). The isosurface is set as 0.01 e/a_0^3. (blue balls: vanadium atoms, red balls: oxygen atoms) (c, d) Diagrams of the two possible pathways for Li within layered α-V_2O_5. (c) in-plane pathway from hollow position (H_a) to another hollow position (H'_a) through top position (T); (d) inter-plane pathway from the hollow position in the upper layer (H_a) to the lower layer (H_a''); (e) The diffusivity of Li through in-plane (blue line) and inter-plane (red line) pathways as a function of the thickness of α-V_2O_5; (f) theoretical relationship of specific capacity including the total mass of the structures as a function of the thickness of the layered α-V_2O_5 based on the case of two Li intercalation/de-intercalation.

The fitted average Li diffusivities along two different pathways for few layers α-V_2O_5 are shown in Figure 5.14e. Overall, the in-plane diffusivity is far higher than the inter-plane pathway by 12 orders of magnitude. The in-plane diffusivity varies exponentially with the thickness, ~ $e^{0.4835x}$, where x is the thickness of V_2O_5 layers. As for the individual diffusivity within diverse layers, the intercalation along the top layer delivers the highest diffusivity. This is due to the lower energy penalty needed to hop from one hollow position to another within the same layer on the surface of the α-V_2O_5 slab. An increase of the layer thickness, results in the binding energy and the energy barrier of Li decreasing, and an increased diffusion rate on the surface. As for the intercalation in the middle of the slides, the diffusivity drops dramatically. The situation is similar to that in bulk structures,

where the Li atoms bind to both the upper and the lower layers. Even though the overall diffusivity is dominated by the in-plane pathway, the inter-plane diffusion plays the key role in accommodating more Li atoms from the solution into the layered α-V_2O_5, and further contributing to the capacity. The simulation results show that the inter-plane diffusion is declined by ~ $x^{-3.3474}$. Two formulas were fitted according to the simulated results of 5 layers of α-V_2O_5 in Table 5.3.

Table 5. 3 Simulated values of the Li diffusivity within layered α-V_2O_5.

Atom layers of V_2O_5	Inter-plane activation energy (eV)	In-plane Activation Energy (eV)	Inter-plane pathway ($cm^2\ s^{-1}$)	In-plane pathway ($cm^2\ s^{-1}$)
1	1.006866	0.354687	1.53×10^{-19}	2.03×10^{-11}
2	1.103866	0.373143 0.25273	8.80×10^{-21}	5.26×10^{-10}
3	1.142663	0.437078 0.181142 0.368686	2.49×10^{-21}	5.53×10^{-9}
4	1.16495	0.52622 0.312728 0.166545 0.542227	1.15×10^{-21}	7.31×10^{-9}
5	1.18675	0.458004 0.13119 0.184827 0.087659 0.346326	5.34×10^{-22}	1.49×10^{-7}

*Maximum values of inter-plane activation energy were shown in the form

Values of all in-plane activation energy were shown in the form

Further analysis was conducted to uncover the conditions for electrode b to realize the highest capacity. The ideal relationship between the thickness of the V_2O_5 layers and the specific capacity is shown in Figure 5.14f. The mass of the conductive and supporting frameworks with negligible contributions to specific capacity, *i.e.* 3D networked $NiCo_2O_4$, was summed with active materials. With the

increase of thickness of the V_2O_5 materials and the mass of the frameworks constant, the mass loading would increase dramatically, and the sum of the specific capacity could be approximately equal to the theoretical values of the V_2O_5 without considering the Li diffusion limitations and electrical conductivity. In practice, from the high magnification SEM images of $NiCo_2O_4$@V_2O_5 CSAs and 3D $NiCo_2O_4$ nanosheets arrays (Figure 5.15), the thickness of the outer layers of V_2O_5 from 3D sandwich structures are ~ 32.6 nm, which is equivalent to ~ 77 atomic layers of V_2O_5. Therefore, the corresponding inter-plane diffusivity of Li for the innermost layer could be estimated as ~ 3.72×10^{-26} cm^2 S^{-1}.

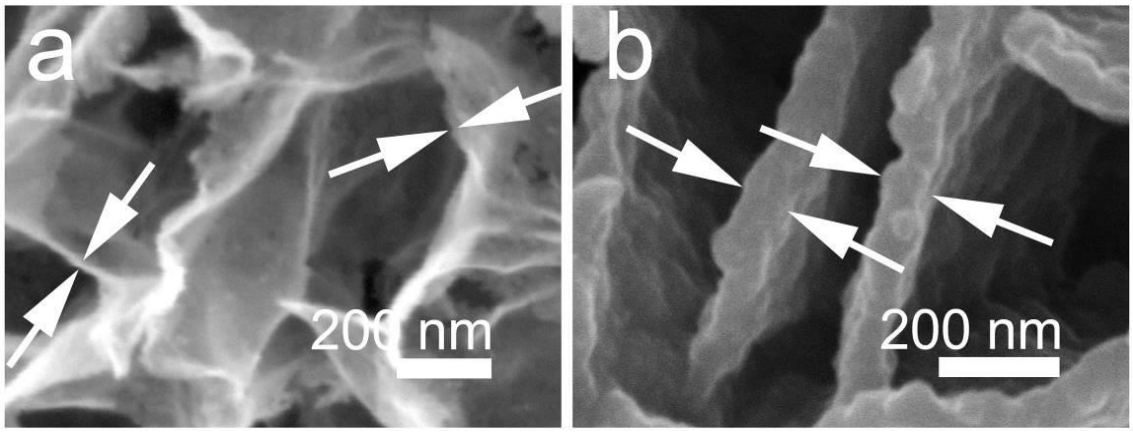

Figure 5. 15 High magnification SEM of (a) 3D $NiCo_2O_4$ nanosheets on carbon cloth; (b) $NiCo_2O_4$@V_2O_5 CSAs/carbon cloth.

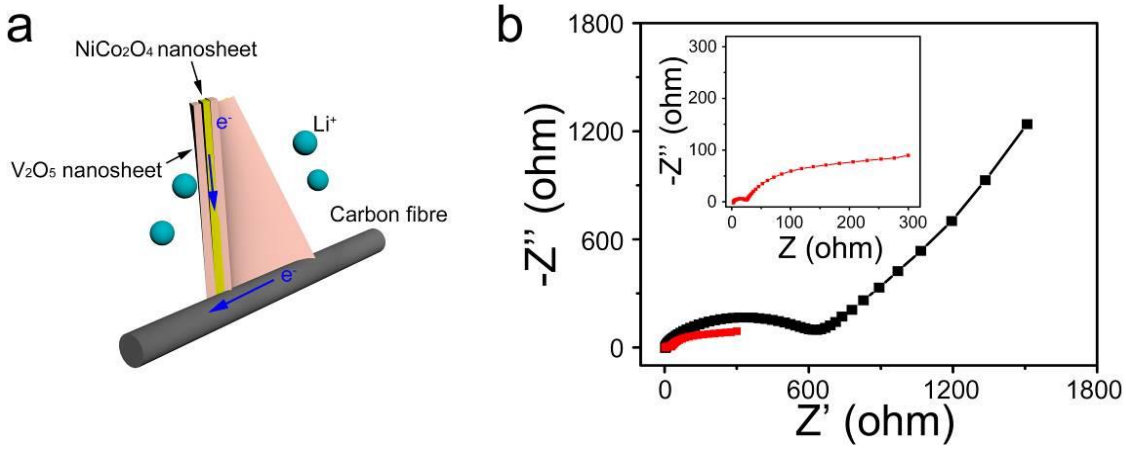

Figure 5. 16 (a) Schematic illustration of electrochemical reactions of $NiCo_2O_4$@V_2O_5 CSAs; (b) EIS spectra of $NiCo_2O_4$@V_2O_5 CSAs/carbon cloth (red line) and V_2O_5 nanoparticles (black line).

Table 5. 4 Parameters from the equivalent circuit model.

Electrodes Parameters	$NiCo_2O_4$@V_2O_5 SAs/carbon cloth	V_2O_5 nanoparticles
R_f (Ω)	21.3	104
R_{ct} (Ω)	223	454
R_s (Ω)	2.87	3.14

Obviously, the rapid decline of diffusion of Li within V_2O_5 layers is the main limitation for realizing the theoretical specific capacity. In these 3D sandwich structures, the above calculated inter-plane diffusivity value together with the enhanced electrical conductivity (Figure 5.16 and Table 5.4) can assure the realizing of theoretical specific capacity at a current density of 0.1 C.

5.4 Conclusion

In this chapter, a targeted design of carbon cloth supported sandwich-structural 3D $NiCo_2O_4$@V_2O_5 CSAs as the binder-free cathode for LIBs was developed. The design stragety was inspired by the work in Chapter 2 and 4 and has been balanced with the major issues in the electrode improvements. The electrode showed excellent specific capacity of ~ 292.0 mA h g^{-1} at a current density of 0.1 C, superior rate capability of ~ 45 % retention when the current density was increased 200 times based on the total mass of active materials and frameworks and one of the best reported cycling performances of 0.0126% capacity decrease per cycle over 500 cycles. Furthermore, the rational structure design was proved by both *in-situ* TEM and theoretical simulations. By further studying the few layer slides of both in-plane and inter-plane pathway through DFT caculations, it is suggested that the speed of diffusivity of Li is dominated by the in-plane direction, whereas inter-plane direction diffusion could host more Li intercalation. The balance of the Li diffusivity and the capacity contribution from the active materials

could be optimized. This chapter expanded the scope of the design concept of nanostructures for electrodes in batteries and shows that layered V_2O_5 nanostructures have an exciting future for cathode application in metal-ion batteries. In addition, further work and strategy need to be developed to increase the mass loading of active mateirals per unit area for binder-free electrodes, as the high areal capacity electrodes are more promising for practical applications.

5.5 References

[1] J. -M. Tarascon, M. Armand, *Nature* **2001**, *414*, 359.

[2] V. Etacheri, R. Marom, R. Elazari, G. Salitra, D. Aurbach, *Energy Environ. Sci.* **2011**, *4*, 3243.

[3] D. Chao, X. Xia, J. Liu, Z. Fan, C. F. Ng, J. Lin, H. Zhang, Z. X. Shen, H. J. Fan, *Adv. Mater.* **2014**, *26*, 5794.

[4] D. Kong, X. Li, Y. Zhang, X. Hai, B. Wang, X. Qiu, Q. Song, Q.-H. Yang, L. Zhi, *Energy Environ. Sci.* **2016**, *9*, 906.

[5] X. Peng, X. Zhang, L. Wang, L. Hu, S. H.-S. Cheng, C. Huang, B. Gao, F. Ma, K. Huo, P. K. Chu, *Adv. Funct. Mater.* **2016**, *26*, 784.

[6] Q. Liu, Z. F. Li, Y. Liu, H. Zhang, Y. Ren, C. J. Sun, W. Lu, Y. Zhou, L. Stanciu, E. A. Stach, J. Xie, *Nat. Commun.* **2015**, *6*, 6127.

[7] X. Rui, Y. Tang, O. I. Malyi, A. Gusak, Y. Zhang, Z. Niu, H. T. Tan, C. Persson, X. Chen, Z. Chen, Q. Yan, *Nano Energy* **2016**, *22*, 583.

[8] M. Chen, X. Xia, J. Yuan, J. Yin, Q. Chen, *J. Power Sources* **2015**, *288*, 145.

[9] X. Rui, Z. Lu, H. Yu, D. Yang, H. H. Hng, T. M. Lim, Q. Yan, *Nanoscale*, **2013**, *5*, 556.

[10] S. Wang, Z. Lu, D. Wang, C. Li, C. Chen, Y. Yin, *J. Mater. Chem.* **2011**, *21*, 6365.

[11] S. Liang, Y. Hu, Z. Nie, H. Huang, T. Chen, A. Pan, G. Cao, *Nano Energy* **2015**, *13*, 58.

[12] G. Yang, H. Song, M. Wu, C. Wang, *Electrochim. Acta* **2016**, *205*, 153.

[13] M. Ihsan, Q. Meng, L. Li, D. Li, H. Wang, K. H. Seng, Z. Chen, S. J. Kennedy, Z. Guo, H.-K. Liu, *Electrochim. Acta* **2015**, *173*, 172.

[14] R. Zou, Z. Zhang, M. F. Yuen, M. Sun, J. Hu, C.-S. Lee, W. Zhang, *NPG Asia Mater.* **2015**, *7*, e195.

[15] G. He, J. Li, W. Li, B. Li, N. Noor, K. Xu, J. Hu, I. P. Parkin, *J. Mater. Chem. A* **2015**, *3*, 14272.

[16] G. Kucinskis, G. Bajars, J. Kleperis, *J. Power Sources* **2013**, *240*, 66.

[17] L. Zhan, S. Wang, L.-X. Ding, Z. Li, H. Wang, *J. Mater. Chem. A* **2015**, *3*, 19711.

[18] B. Sun, K. Huang, X. Qi, X. Wei, J. Zhong, *Adv. Funct. Mater.* **2015**, *25*, 5633.

[19] B. Yan, X. Li, Z. Bai, Y. Zhao, L. Dong, X. Song, D. Li, C. Langford, X. Sun, *Nano Energy* **2016**, *24*, 32.

[20] G. Kresse, J. Furthmuller, *Phys. Rev. B* **1996**, *54*, 169-186.

[21] D. O. Scanlon, A. Walsh, B. J. Morgan, G. W. Watson, *J. Phys. Chem. C* **2008**, *112*, 9903.

[22] J. P. Perdew, J. A. Chevary, S. H. Vosko, K. A. Jackson, M. R. Pederson, D. J. Singh, C. Fiolhais, *Phys. Rev. B* **1992**, *46*, 6671-6687.

[23] K. Lee, É. D. Murray, L. Kong, B. I. Lundqvist, D. C. Langreth, *Phys. Rev. B* **2010**, *82*, 081101(R).

[24] T. Thonhauser, V. R. Cooper, S. Li, A. Puzder, P. Hyldgaard, D. C. Langreth, *Phys. Rev. B* **2007**, *76*, 125112.

[25] M. Dion, H. Rydberg, E. Schroder, D. C. Langreth, B. I. Lundqvist, *Phys. Rev. Lett.* **2004**, *92*, 246401.

[26] J. Klimes, D. R. Bowler, A. Michaelides, *J. Phys. Condens. Matter.* **2010**, *22*, 022201.

[27] J. Klimeš, D. R. Bowler, A. Michaelides, *Phys. Rev. B* **2011**, *83*, 195131.

[28] G. Roman-Perez, J. M. Soler, *Phys. Rev. Lett.* **2009**, *103*, 096102.

[29] J. S. Braithwaite, C. R. A. Catlow, J. D. Gale, J. H. Harding, *Chem. Mater.* **1999**, *11*, 1990.

[30] S. Fabris, S. de Gironcoli, S. Baroni, G. Vicario, G. Balducci, *Phys. Rev. B* **2005**, *72*, 041102(R).

[31] G. Henkelman, B. P. Uberuaga, H. Jónsson, *J. Phys. Chem.* **2000**, *113*, 9901.

[32] J. P. Perdew, A. Ruzsinszky, G. I. Csonka, O. A. Vydrov, G. E. Scuseria, L. A. Constantin, X. Zhou, K. Burke, *Phys. Rev. Lett.* **2008**, *100*, 136406.

[33] H. Song, C. Zhang, Y. Liu, C. Liu, X. Nan, G. Cao, *J. Power Sources* **2015**, *294*, 1.

[34] M. Castriota, E. Cazzanelli, A. Fasanella, D. Teeters, *Thin Solid Films* **2014**, *553*, 127.

[35] H. Yu, X. Rui, H. Tan, J. Chen, X. Huang, C. Xu, W. Liu, D. Y. Yu, H. H. Hng, H. E. Hoster, Q. Yan, *Nanoscale* **2013**, *5*, 4937.

[36] G. Q. Zhang, H. B. Wu, H. E. Hoster, M. B. Chan-Park, X. W. Lou, *Energy Environ. Sci.* **2012**, *5*, 9453.

[37] H. Song, C. Liu, C. Zhang, G. Cao, *Nano Energy* **2016**, *22*, 1.

[38] F. Lin, D. Nordlund, Y. Li, M. K. Quan, L. Cheng, T.-C. Weng, Y. Liu, H. L. Xin, M. M. Doeff, *Nature Energy* **2016**, *1*, 15004.

[39] T. Kim, J. Shin, T.-S. You, H. Lee, J. Kim, *Electrochim. Acta* **2015**, *164*, 227.

[40] M. Freire, N. V. Kosova, C. Jordy, D. Chateigner, O. I. Lebedev, A. Maignan, V. Pralong, *Nat. Mater.* **2016**, *15*, 173.

[41] J. Carrasco, *J. Phys. Chem. C* **2014**, *118*, 19599.

[42] R. Enjalbert, J. A. Galy, *Acta Crystallogr. C* **1986**, *C42*, 1467.

[43] X. Han, H. M. Stewart, S. A. Shevlin, C. R. Catlow, Z. X. Guo, *Nano Lett.* **2014**, *14*, 4607.

[44] J. J. Krochmal, *J. Am. Ceram. Soc.* **1965**, *48*, 328.

[45] N. V. Hieu, *J. Vac. Sci. Technol.* **1981**, *18*, 49.

[46] S. F. Cogan, N. M. Nguyen, S. J. Perrotti, R. D. Rauh, *J. Appl. Phys.* **1989**, *66*, 1333.

[47] A. Z. Moshfegh, A. Ignatiev, A. *Thin Solid Films* **1991**, *198*, 251.

[48] Z. Wang, Q. Su, H. Deng, *Phys. Chem. Chem. Phys.* **2013**, *15*, 8705.

[49] G. S. Gautam, P. Canepa, R. Malik, M. Liu, K. Persson, G. Ceder, *Chem.*

Commun. (Camb.) **2015**, *51*, 13619.

[50] W. Y. Ma, B. Zhou, J. F. Wang, X. D. Zhang, Z. Y. Jiang, *J. Phys. D: Appl. Phys.* **2013**, *46*, 105306.

[51] R. Kutner, *Phys. Lett. A* **1981**, *81A*, 239.

[52] K. A. Connors, *Wiley* **1990**.

[53] G. H. Vineyard, *J. Phys. Chem. Solids* **1957**, *3*, 121.

[54] P. Clauws, J. Vennik, *Phys. Stat. Sol. B* **1976**, *76*, 707.

Chapter 6

Summary and outlook

To further meet the criteria of energy demands, two typical strategies are widely investigated as aspect to electrodes in energy storage devices, including the exploration of novel materials and design of favourable configurations. This doctoral thesis has shown several novel materials/electrode configurations by means of two-pronged approaches to increase the electrochemical properties of the electrodes. The structural design and synthetic tactic could provide further guidance for developing high-performance electrodes and possibly the broader sphere of energy conversion applications, such as oxygen reduction/evolution, hydrogen evolution, *etc*.

In Chapter 1, the background of different types of energy storage devices were introduced, especially the supercapacitors and Li-ion batteries. The properties and application of transition metal derivatives, such as nickel, cobalt and tungsten, were introduced. The representative nanostructured materials for electrodes *via* different chemical synthesis, such as template-assisted method, exfoliation process and wet chemistry in various dimensions were discussed. The advantages and challenges of these energy storage materials were proposed.

In Chapter 2, nickel foam supported $NiWO_4$ and $CoWO_4$ electrodes were reported. The electrodes are among the top-tier of the similar materials and better than powder fabricated electrodes. The use of ternary transition metal materials and binder-free strategy could improve the electrical conductivity of the entire electrodes. Herein, the tungsten elements could not contribute to capacity through redox reaction. Further work around this system could discuss different species contribution in various electrolytes. In addition, the function and energy storage mechanism of nickel and cobalt species in alkaline electrolyte should be clarified. The future work around these materials could discover the relationships between structures and properties. One interesting topic is the phase-separated $NiWO_4$ or $CoWO_4$ materials (formed Co-WO_3 or Ni-WO_3) used in electrocatalytic areas. As these materials should be active catalysis, such as for hydrogen

evolution, deep research into boundary or surface chemistry should be meaningful and interesting.

In Chapter 3, sulfur and nitrogen co-doped nickel cobalt sulfides aerogels were developed and synthesized. This was a systematic research by controlling different atomistic ratios of nickel and cobalt in sulfides, mass ratios of metal sulfides and graphene aerogels to optimize energy storage and conversion properties of these materials. The utilizations of the materials as rechargeable alkaline electrodes and electrocatalysts for oxygen reduction reaction were explored. Importantly, nickel cobalt-based materials were demonstrated as the battery-type energy storage electrode materials through kinetic analysis from electrochemistry and *ex-situ* XRD measurements, which suggested that these electrode materials did not behave as pseudocapacitors as claimed in Chapter 2 and in many other literature reports. Nickel cobalt sulfides were promising materials as alkaline battery electrodes; however, the fluffy graphene aerogels may decrease the volumetric capacity for the hybrid electrodes. Further work could be carried out by designing high volumetric/areal capacity nickel cobalt sulfide electrode materials. In addition, kinetic analysis reflected diffusion-dominated and hybrid features (limited surface-controlled process) in this system, the facile methods or computer programs for separation of the contribution from surface-controlled and diffusion-controlled processes should be developed. The materials synthesized in this chapter are not highly active catalysts for ORR, which cannot be compatible to the commercial noble metal catalysts. The modification of the nickel cobalt derived high-performance catalysts, such as nitrides, for ORR and detailed mechanism discussion could be discussed in the future work.

Tungsten-based materials could be used as the electrodes in acid electrolytes by redox reactions between tungsten and protons. In Chapter 4, the free-standing electrodes of carbon cloth supported W_2N@C nanorods were obtained by

AACVD and by an annealing process. Compared to previous reports, the merits of W_2N materials as electrodes for pseudocapacitor electrodes compared to oxide counterparts were uncovered by electrical property testing *via in situ* TEM and DFT calculations. The asymmetric flexible devices were fabrication as demostrations for practical applications as the free-standing electrodes. However, as a potentially active materials for electrochemical water splitting, the limitation of the voltage window of the supercapacitor devices based on W_2N remains a problem. Even though the ionic liquid electrolyte was also used in this chapter, the specific capacitance was not high. Further work could be related to modification of the electrolyte to enlarge the potential window without sacrificing capacitance to improve the energy density of the devices.

In Chapter 5, a targeted design of sandwich structured $NiCo_2O_4$ and V_2O_5 on carbon cloth electrodes were designed. Inspired by chapter 2 to utilize relatively high electrical conductivity and stable features during cathode voltage range *vs.* Li^+/Li of $NiCo_2O_4$ materials, $NiCo_2O_4$ nanosheets were served as the robust framework. By consideration of the Li diffusivity, electrical conductivity and structural stability, the Li storage performance could be optimized. The loading amount of the active materials is restrictive, which could limit the areal capacity of the entire electrodes. In addition, the use of carbon cloth as the current collector in both Chapter 3 and 4 could be changed by other lightweight current collectors, for example using the thinner hollow carbon-tube interweaved frameworks.

For all binder-free or self-standing electrodes, other factors, such as the binding mechanism and loading amount of the active materials, should be considered in the future, which could provide the robust adherence between different components and facilitate electron transport. Binding behavior could be optimized by different reactants and loading amounts are suggested to control through various dimensional architecture.

Most of the above-listed insight/future work is happening in ongoing projects. The transition metal derivatives and their hybrids show great application prospects in energy storage areas, not only limited to supercapacitors, Li-ion batteries and hybrid devices in this thesis. Metal-ion (multivalent metals) or metal-air batteries are the next-generation devices for energy storage, the related developed materials reported in this thesis could hopefully serve in these devices. In summary, the future research will around synthesis of different transition metal materials for these applications, research from materials to devices and detailed mechanism analysis by both surface-chemistry and solid-chemistry approaches, including *in situ* measurements, such as TEM, AFM, XRD and XAS, together with more collaborations of computational studies at diverse scales.

Publication List

Publication related to the thesis:

(1) **G. He**, J. Li, W. Li, Noor N., K. Xu, J. Hu*, I. Parkin*, One pot synthesis of Nickel foam supported self-assembly of $NiWO_4$, $CoWO_4$ nanostructures that act as high performance electrochemical capacitor electrodes, ***J. Mater. Chem. A***, 2015, 3, 14272-14278. **(Highlighting materials research in the UK for energy and sustainability)**

(2) **G. He**, M. Qiao, W. Li, Y. Lu, T. Zhao, R. Zou, B. Li, J. Darr, J. Hu, M. Titirici and I. Parkin*, S, N-co-doped Graphene-Nickel Cobalt Sulfide Aerogel: Improved Energy Storage and Electrocatalytic Performance, ***Adv. Sci.,*** 2017, 1600214. **(Most access paper; ESI highly cited paper)**

(3) **G. He**, M. Ling, X. Han, D. Ibrahim Abou El Amaiem, Y. Shao, Y. Li, W. Li, S. Ji, B. Li, Y. Lu, R. Zou, F. Wang, D. J.L. Brett, Z. Guo, C. Blackman, I. P. Parkin*, Self-standing Electrodes with Core-shell Structures for High-performance Supercapacitors, ***Energy Storage Mater.,*** 2017, 9, 119-125.

(4) **G. He**, X. Han, R. Zou*, T. Zhao, Z. Weng, S. Ho-Kimura, Y. Lu, H. Wang, Z. X. Guo and I. P. Parkin*, A Targeted Functional Design for Highly Efficient and Stable Cathodes for Rechargeable Li-Ion Batteries, ***Adv. Funct. Mater.,*** 2017, 27, 1604903.

Other Pulications during PhD study:

(5) W. Li, B. Zhang, R. Lin, S. Ho-Kimura, **G. He**,* J. Hu* and I. P. Parkin*, A Dendritic Nickel Cobalt Sulfide Nanostructure for Alkaline Battery Electrodes, ***Adv. Funct. Mater.,*** 2018, 1705937. **(Back Cover Story)**

(6) R. Lin, Z. Li, D. Ibrahim Abou El Amaiem, B. Zhang, D. J.L. Brett, **G. He*** and I. P. Parkin*, A general method for boosting the supercapacitor performance of graphitic carbon nitrides/graphene hybrids, ***J. Mater. Chem. A.***, 2017, 5, 25545.

(7) B. Li, X. Wang, X. Wu, **G. He**,* R. Xu, X. Lu*, F. Wang, I. P. Parkin*, Phases and Morphological Control of MoO_{3-x} Nanostructures for Efficient

Cancer Theragnosis Therapy, ***Nanoscale***, 2017, 9, 11012–11016.

(8) Y. Lu, **G. He**,***** C. J. Carmalt and I. P. Parkin*****, Synthesis and characterization of omniphobic surfaces with thermal, mechanical and chemical stability, ***RSC Adv.***, 2016, 6, 106491-106499.

(9) Y. Zhao, W. Li, Z. Wang and **G. He**,* Electric field induced slanting growth of silicon nanowires with enhanced hydrophobic property, ***Mater. Lett.***, 2017, 198, 8-11.

(10) W. Li, R. Xu, M. Ling and **G. He,*** Ag-Ag_2S/Reduced Graphene Oxide Hybrids Used as Long-Wave UV Radiation Emitting Nanocomposites, ***Opt. Mater.,*** 2017, 72, 529-532.

(11) B. Li[1], F. Yuan[1], **G. He[1]**, X. Han, X. Wang, J. Qin, Z. X. Guo, X. Lu, Q. Wang, I. Parkin and C. Wu*, Ultrasmall $CuCo_2S_4$ Nanocrystals: All-in-One Theragnosis Nanoplatform with Magnetic Resonance/Near-Infrared Imaging for Efficiently Photothermal Therapy of Tumors, ***Adv. Funct. Mater.,*** 2017, 1606218. **(Co-first author)**

(12) D. Abouelamaiem, **G. He,** I. Parkin, T. Neville, A. Jorge, S. Ji, R. Wang, M. Titirici, P. Shearing, D. Brett*, Optimization of KOH/Cellulose Ratios for Biocarbon Hierarchically-Porous Supercapacitor Materials, ***Sustainable Energy & Fuels*****,** 2018, 2, 772–785. **(Front Cover Story)**

(13) D. Abouelamaiem, **G. He**, T.P. Neville, D. Patel, S. Ji, R. Wang, I.P. Parkin, A.B. Jorge, M.-M. Titirici, P.R. Shearing, D.J.L. Brett*, Correlating electrochemical impedance with hierarchical structure for porous carbon-based supercapacitors using a truncated transmission line model, ***Electrochimica Acta*****,** 2018, doi: 10.1016/j.electacta.2018.07.190.

(14) R. Zou, **G. He**, K. Xu, Q. Liu, Z. Zhang, J. Hu*, ZnO nanorods on reduced graphene sheets with excellent field emission, gas sensor and photocatalytic properties, ***J. Mater. Chem. A***, 2013, 1, 8445-8452.

(15) W. Li, **G. He**, J. Shao, Q. Liu, K. Xu, J. Hu* and I. Parkin*, Urchin-like MnO_2 capped ZnO nanorods as high-rate and high-stability pseudocapacitor electrodes, ***Electrochimica Acta***, 2015, 186, 1-6.

(16) R. Zou, Q. Liu, **G. He**, M. Yuen, K. Xu, I. Parkin, J. Hu*, C. Lee* and W. Zhang*, V_2O_5 Nanoparticles Encapsulated in 3D Networked Porous Carbon Coated Carbon Fibers: An Ultrastable Cathode for Li-Ion Batteries, ***Adv. Energy Mater.***, 2017, 2017, 7, 1601363.

(17) W. Zong, F. Lai*, **G. He**, J. Feng, R. Lian, Y. Miao, G. Wang, I. P. Parkin, and T. Liu*, Sulphur-Deficient Bismuth Sulfides/Nitrogen-Doped Carbon Nanofiber Nanofibre as Advanced Free-standing Electrode for Asymmetric Supercapacitors, ***Small***, 2018, 1801562.

(18) D. Abouelamaiem, L. Rasha, **G. He**, T. P. Neville, J. Millichamp, T. J. Mason, Ana Belen Jorge, Ivan P. Parkin, M. Titirici, R. Wang, S. Ji, P. R. Shearing, D. J. L. Brett, Integration of Supercapacitors into Printed Circuit Boards, ***J. Energy Storage***, 2018, 19, 28-34.

(19) M. Qiao, C. Tang, **G. He**, K. Qiu, R. Binions, I. Parkin, Q. Zhang, Z. Guo and M. M. Titirici*, Graphene/Nitrogen-Doped Porous Carbon Sandwiches for Metal-Free Oxygen Reduction Reaction: Conductivity versus Active Sites, ***J. Mater. Chem. A***, 2016, 4, 12658-12666.

(20) W. Li, J. Wang, **G. He**, L. Yu, N. Noor, Y. Sun, X. Zhou, J. Hu* and I. Parkin*, Enhanced Adsorption Capacity of Ultralong Hydrogen Titanate Nanobelts for Antibiotics, ***J. Mater. Chem. A***, 2017, 5, 4352–4358.

(21) X. Zhang, W. Zhu, **G. He**, I. P. Parkin*, Flexible and Mechanically Robust Superhydrophobic Silicone Surfaces with Stable Cassie-Baxter State, ***J. Mater. Chem. A***, 2016, 4, 14180-14186.

(22) T. Zhao, S. Gadipelli, **G. He**, M. J. Ward, D. Do, P. Zhang and Z. Guo*, Tunable Bifunctional Activity of $Mn_xCo_{3-x}O_4$ Nanocrystals Decorated at Carbon Nanotubes for Oxygen Electrocatalysis, ***ChemsusChem***, 2018, 11, 1295-1304. **(Front Cover Story)**

(23) G. Hu, W. Li*, **G. He**, J. Wang, Y. Zhao, Y. Zhang, B. Yao. Molten salt synthesis of $Zn_{1.8}Mn_{0.2}SiO_4$ luminescent materials in NaCl-$ZnCl_2$ eutectic salt, ***Ceram. Int.***, 2016, 42, 7852-7856.

(24) H. Wang, Q. Ren, D. J. L. Brett, **G. He**, R. Wang, J. Key, S. Ji*, Double-

shelled tremella-like NiO@Co_3O_4@MnO_2 as a high-performance cathode material for alkaline supercapacitors, ***J. Power Sources***, 2017, 343, 76-82.

(25) Q. Ren, Z. Peng, B. Li, **G. He**, W. Zhang, G. Guan, X. Huang, L. Liao, Y. Pan, X. Yang, R. Zou, J. Hu*, SnS nanosheets for efficient photothermal therapy, ***New J. Chem.***, 2016, 2016,40, 4464-4467.

(26) G. Hu, W. Lim J. Xu, **G. He**, Y. Ge, Y. Pan, J. Wang and B. Yao*, Substantially reduced crystallization temperature of SBA-15 mesoporous silica in $NaNO_3$ molten salt, ***Mater. Lett.***, 2016, 170, 179-182.

(27) F. Chen, Y. Lu, X. Liu*, J. Song, **G. He**, M. K. Tiwari, C. J. Carmalt, I. P. Parkin*, Table Salt as a Template to Prepare Reusable Porous PVDF-MWCNT Foam for Separation of Immiscible Oils/Organic Solvents and Corrosive Aqueous Solutions, ***Adv. Funct. Mater.***, 2017, 1702926. **(Front Cover Story)**

(28) Z. Weng, X. Zhang, Y. Wu, S. Huo, J. Jiang, W. Liu, **G. He**, Y. Liang*, H. Wang*, Self-Cleaning Catalyst Electrodes for Stabilized CO_2 Reduction to Hydrocarbons, ***Angew. Chemie. Int. Edit.,*** 2017, 2017, 56, 1-6.

(29) R. Zou, Z. Cui, Q. Liu, G. Guan, W. Zhang, K. Xu, **G. He**, J. Yang, J. Hu*, In situ Transmission Electron Microscopy Study of Individual Nanostructures during Lithiation and Delithiation Processes, ***J. Mater. Chem. A.,*** 2017, 5, 20072–20094.

Under reviews/In preparation:

(30) **G. He**, X. Han, B. Moss, Z. Weng, S. Gadipelli, F. Lai, A. G. Kafizas, D. J. L. Brett, Z. X. Guo, H. Wang, I. P. Parkin, Solid Solution Nitride/Carbon Nanotube Hybrids Enhance Electrocatalysis of Oxygen in Zinc-Air Batteries, ***Energy Storage Mater.,*** 2018, in revision.

(31) R. Zou, S. He, Z. Cui, X. Han, R. Lin, **G. He***, D. J.L. Brett, Z. X. Guo, J. Hu, I. P. Parkin*, A 'Self-Protection' Mechanism Promotes the Performance of Anodes in Li-ion Batteries, ***Energy Environ. Sci.***, 2018, under review.

(32) Q. Hu, W. Li,* B. Zhang, W. Sun, R. Lin, H. Jiang, and **G. He**,* Uniform

NiO nanoparticles used as anodes in Li-ion batteries, ***Mater. Lett.***, 2018, under review.

(33) Z. Li, Y. Yang, **G. He**, J. Guo, J. Li, Y. Lu, I. P. Parkin, S. Gadipelli and Z. Guo, ***Energy Environ. Sci.***, 2018, under review.

(34) S. Ho-Kimura, B. A. D. Williamson, S. Sathasivam, S. J. A. Moniz, **G. He**, D. O. Scanlon, J. Tang, and I. P. Parkin, 2018, under review.

(35) H. Tang, W. Li*, Z. Wang, **G. He***, W. Sun, Q. Hu, I. P. Parkin*, Carbon/Ultralong Titanium dioxide nanotubes composite for adsorption antibiotics, 2018, to be submitted.

(36) **G. He**, et al, Mechanism of biomass carbon as supercapacitor electrodes in different electrolytes, in preparation.

(* corresponding author)

Academic activities

- 11/2015-present Invited referee and adjudicative referee, Advanced Energy Materials (SCI); Journal of Materials Chemistry A (SCI); Chemical Communications (SCI); Physical Chemistry Chemical Physics (SCI); Dalton Transactions (SCI); Materials Science & Engineering C (SCI); International Journal of Hydrogen Energy (SCI); Journal of Energy Chemistry (SCI); Thin Solid Films (SCI); ACS applied Energy Materials (SCI)
- 07/2018 Oral presenter, Thinfilms2018, China
- 04/2018 Invited talk, JUICED Hub project meeting, Southampton, U.K.
- 12/2017 Invited talk, JUICED Electrochemistry Workshop, UCL, U.K.
- 11/2017 Invited talk, Henan University, China.
- 08/2017 Poster presenter, 13th European Congress on Catalysis, Italy
- 08/2017 Invited talk, External talk for Prof. Clare Grey's group meeting, University of Cambridge, U.K.
- 03/2017 Oral presenter, STFC Early Career Researchers Conference 2017, U.K. (Best Talk winner)
- 03/2017 Poster presenter, 5th International Conference on Multifunctional, Hybrid and Nanomaterials, Portugal
- 05/2016 Poster presenter, 5th International Conference on Advanced Capacitors, Japan
- 04/2016 Poster presenter, STFC Early Career Researchers Conference 2016, U.K.
- 05/2015 Invited speaker, Energy Materials Network London, Young Researchers Symposium, Queen Mary University of London, U.K.